The numerical investigation of a bank of delta plenum air-cooled heat exchangers

Dwain Iain Dunn

Thesis presented in partial fulfillment
for the Degree of Master of Science in the
Department of Mechanical Engineering
University of Cape Town

September 21, 2006

Declarations

I hereby:

1. Grant the University of Cape Town free license to reproduce the aforementioned dissertation in whole or in part for the purpose of research;

2. Declare that:

   (a) The aforementioned dissertation is my own unaided work. Except for normal guidance of my supervisor, I have received no assistance apart from that stated below;

   (b) Except as stated below, neither the substance or any part of the thesis has been submitted in the past, or is being submitted for a degree in this, or any other University;

I have used the Vancouver referencing system for citation and referencing. Each significant contribution and quotation in this report from works by other people have been attributed and have been referenced and cited.

Signed by candidate

Signature:..... Date:..19 October 2006

Dwain Iain Dunn

Acknowledgments

I would like to thank the following people for their help and support, without which this dissertation would not have been possible:

- The Lord, Our Father, for providing me with the opportunity, and ability to do this MSc.
- Dr. Chris Meyer for the encouragement, help with financial support, and faith in my abilities. I could not have done this without your guidance.
- My parents, without whom I would not be here. Thank you for all the sacrifices you have made to enable me to get this far. I am eternally indebted to you.
- CERECAM and the CFD research group for providing the necessary resources for this dissertation.
- J.P. Pelteret and D. Engelbrecht for there help with proof reading.
- My fellow postgraduates for the companionship and help.

Abstract

Forced draught air-cooled heat exchangers (ACHE's) are often used in arid regions as a means to cool down process fluids, and as air-cooled condensers as well. When a large amount of process heat must be rejected the ACHE's are arranged in large banks. The size of these banks often create adverse flow fields in the region of the peripheral fans. Experimental work has been performed on some of these phenomena, but due to the scale of interest, it would be impractical to investigate all possibilities. Therefore a numerical model was developed.

To reduce complexity, the fan was modeled as an actuator disc, which produces a good correlation to experimental data. The heat exchangers were modeled as a porous region which when using the appropriate constants reproduced the heat exchangers performance characteristics to a high degree of accuracy.

To validate the model, the effect of ground clearance and the presence of a walkway were investigated, and compared to experimental data. The correlation was good, but it was found that modeling of the heat exchanger and surrounding area over-predicted the fan volumetric effectiveness, compared to the investigations where just the fan is modeled. A two dimensional array was also investigated in order to inspect the flow field around the fans in the vicinity of an unconstrained corner. It was found that orientation of the plenum had an effect on the fan performance. When the plenum's are joined the fans that operate at a higher volume flow rate induce a cross flow in the plenum which decreases the volumetric effectiveness of the fans that operate at a lower volumetric effectiveness. When the plenums of all the ACHE's were connected, the fan closest to the perimeter of the ACHE bank behaved worse then if the steam tube on top of each plenum ran parallel to each other. The effect of wind was also investigated, and it was found that the presence of wind decreased the fan volumetric effectiveness curve.

Contents

List of Figures

List of Tables

Nomenclature

Symbols

A	Area (m^2)
b	Exponent used to calculate H_{HE}
a	Co-efficient used to calculate H_{HE}
C	Coefficient
c_{fb}	Fan blade chord length (m)
D	Drag (N)
d	Diameter (m)
k	Turbulent kinetic energy $(m^2.s^2)$
K	Dynamic pressure loss co-efficient
L	Lift (N) or Length (m)
M	Mach Number
N	Rotational speed (rpm)
P_R	Power (W)
p	Pressure (Pa)
Q	Torque (Nm)
Re	Reynolds Number
R_y	Characteristic flow parameter (m^{-1})

S	Source Term
T	Thrust (N)
t	Time (s)
v	Velocity (m/s)
V	Volume flow rate (m^3/s)
x	Distance (m)
z	Height (m)

Greek Symbols

α	Angle of attack $(^\circ)$
$\frac{1}{\alpha}$	Viscous resistance factor
β	Angle between the relative velocity vector, and the fan blade plane of rotation
δ_r	Blade element radial thickness
δ_{ij}	The Kronecker Delta
η	Efficiency $(\%)$
ϵ	Turbulent energy dissipation rate $(m^2.s^3)$
γ	Blade stagger angle $(^\circ)$
μ	Viscosity $(kg.m^{-1}.s^{-1})$
μ_t	Turbulent Viscosity $(kg.m^{-1}.s^{-1})$
ω	Specific dissipation rate (s^{-2})
ρ	Density $(kg.m^{-3})$
σ	Contraction ratio
$\bar{\bar{\tau}}$	Stress tensor
θ	Semi-apex angle of the delta plenum $(^\circ)$

Subscripts

ref	Calculated from point 2 to point 1
$34, 45$	Between the points numbered
c	Contraction
ci	Contraction at the inlet
d	Drag
dj	Downstream jetting
Fb	Fan blade
FC	Fan casing
Fr	Fan rotor
FS	Fan static
HE	Heat Exchanger
l	Lift
m	Mean
m	Momentum
o	Outlet
r	Radial
ref	Reference value
te	Trailing edge
θt	Total for a delta plenum

Acronyms

ACC	Air-cooled condensers
ACHE	Air-cooled Heat Exchanger

CFD Computational Fluid Dynamics

IO Input/output operations

RANS Reynolds Averaged Navier-Stokes equations

RNG Renormalization Group

RSM Reynolds Stress Model

UDF User Defined Function

Glossary

Array	A collection of ACHE row's
Bank	A collection of ACHE's arranged such that the fan axis are aligned vertically.
Cortex	The FLUENT® process responsible for user interface, and graphic related functions.
Exterior	Cells that belong to a different compute node, but are present to ensure continuity of data.
Fan blade tip clearance	The space between the fan blade tip and the fan casing.
Fan swept region	The region swept by the fan blades.
Fouling	Build up of dirt and dust on the heat exchanger fins.
Ground Clearance	The distance from the base of the fan platform to the ground.
Hexahedral Mesh	A mesh where the cells have six faces.
Host	The FLUENT® process responsible for IO operations, and interpreting commands sent by the cortex.

Interior	Cells that belong to the current compute node.
Navier-Stokes equations	The governing equations for fluid flow.
Node	The FLUENT® process that holds all the data, and does the computation.
Parallel computer	A system where more then 1 CPU is available to do the calculations.
Parallelization	The process of making a serial UDF one which can be used in a parallel environment.
Plenum	A chamber that is at a higher pressure then the surroundings.
Porous	A solid region which has pathways to allow fluid flow.
Row	A Nx1 set of ACHE's in a bank, running from the periphery on one side to the periphery on the opposite side.
Serial computer	A computer that has only 1 CPU available for calculations.
Solidity ratio	The ratio of fan blade area to area swept by the fan blades.
Tetrahedral Mesh	A mesh where the cells have four faces.
Volumetric effectiveness	Ratio of the actual volume flow rate through a fan to the ideal volume flow rate.

Walkway A horizontal platform that is attached to the perimeter of an ACHE bank, at the base of the fan platform.

Chapter 1

Introduction

1.1 Background

Forced draught Air-cooled Heat exchangers (ACHE's) are widely used in chemical, process, and petro-chemical industries to cool down hot process fluids. ACHE's have also been successfully implemented in power plants as air-cooled condensers, (ACC's) [5, 6]. In large installations where a large amount of heat needs to be rejected, multiple ACHE's are gathered into banks that consist of multiple rows of fans. The fan axes are aligned in the vertical direction, with the heat exchanger located down stream of the fan, for the forced draught case, and upstream of the fan for the induced draught case. Air is drawn in by the fan and forced over the heat exchanger taking some of the process heat along with it. The volume of air that passes over the heat exchanger thus directly affects the cooling capacity of the ACHE unit.

Since all the fans draw their air through the same region at the boundary of the ACHE bank, as shown in Figure 1.1, the number of ACHE units, as well as the clearance height above the ground will affect the volume of air that the fans have access to. This is due to the finite area open to the atmosphere along the perimeter of the bank. Since all the fans draw air in from the boundary, induced cross-flows are created at the inlets of the periphery fans [7, 8, 9]. This induced cross flow has a negative effect on the fans' performance characteristics and increases the fan inlet losses. The inlet losses are predominantly caused by oblique flow, shown in Figure 1.2, and flow separation, shown in Figure 1.3.

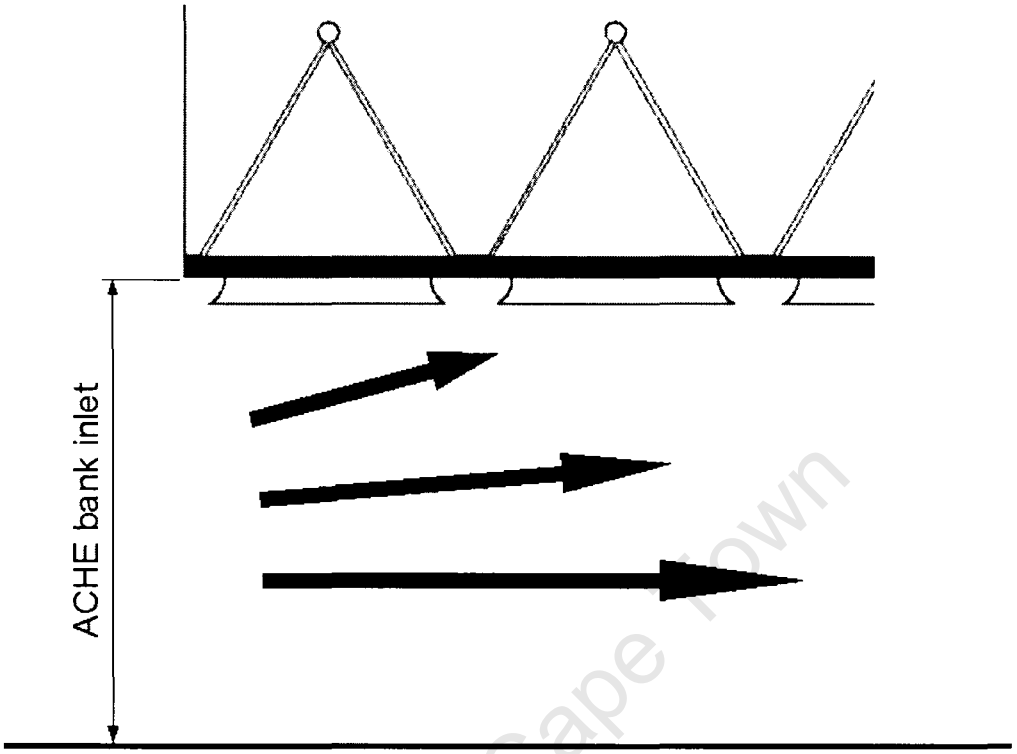

Figure 1.1: A schematic representation of an ACHE bank, showing the finite inlet area shared by all the fans in that row

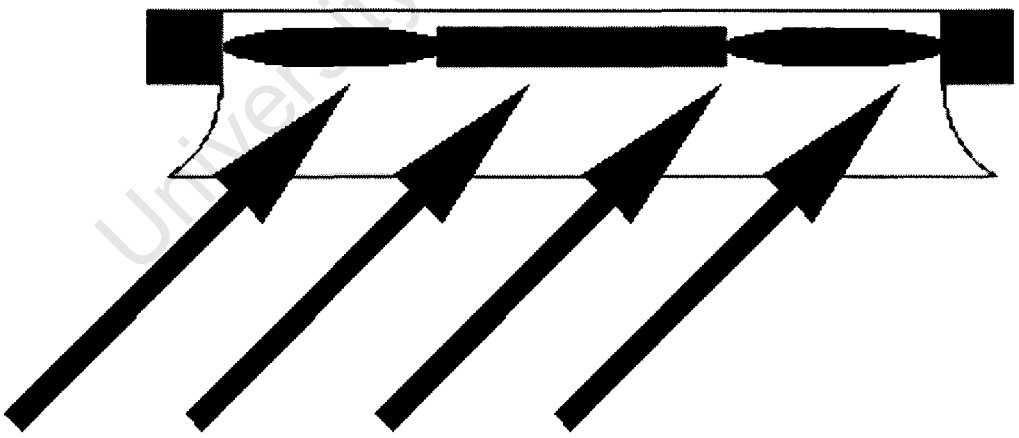

Figure 1.2: Oblique flow into the fan

1.2 Reasons for current investigation

Currently there are no practical means to experimentally investigate the flow field in the vicinity of a bank of ACHE's on the scale required. The Matimba power plant in

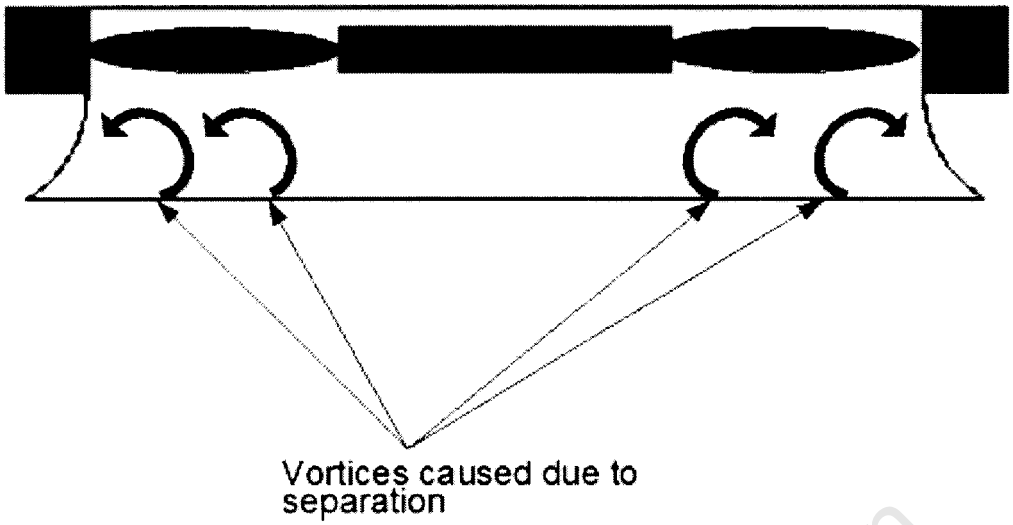

Figure 1.3: Flow separation at the inlet of the bell mouth

South Africa uses ACHE's that have fans of $d_{FC} = 9.145m$ in diameter [10]. Physical experiments on this scale would be both time consuming and expensive. The expense would further be compounded by the need to control the effects of wind.
It has been shown previously that computational fluid dynamics, CFD, is a powerful tool for analysing the flow field in the vicinity of an axial flow fan [10, 1] as well as for air-cooled heat exchangers [5, 11, 12]. For this reason CFD will be investigated as an alternative means of analysing the flow field in and around an ACHE bank.

1.3 Objectives

The purpose of this investigation was to develop a method whereby a large bank of ACHE's can be quickly and relatively accurately modeled. The objectives are thus :

- Parallelize the fan model used by Meyer [1], and validate it's use for parallel processing.
- Develop a method to simulate the performance characteristics of a heat exchanger.
- Validate the coupling of the fan model and the heat exchanger. This should be done by comparing the operating point of the delta plenum ACHE obtained empirically and numerically.
- Simulate an ACHE bank, and verify that the numerical results correlate with the experimental results.

1.4 Limitations

One of the largest limitations was the computational requirement of the simulations. In order to improve accuracy, the grid needs to be refined. This requires more RAM and will take substantially longer to simulate. For this reason the simulations will be kept as steady state simulations, with the minimum number of cells as required to maintain accuracy.

Due to the scale of the domain to be investigated, small scale effects will be ignored. These include, but are not limited to:

- Boundary layer effects and the effect they impose on the flow.
- Flow restrictions caused by fan motors and mountings, cables, fan platform supports etc.
- The effect of different surface roughnesses on the flow. All solid objects are treated as having completely smooth surfaces.
- The effect of fouling of the heat exchanger fins. The heat exchangers are treated as being uniform, and exhibit identical ideal characteristics at all points on its surface.

This investigation was concerned with the flow field in and around the ACHE only. Therefor the flow will be treated as being iso-thermal, and incompressible. The numerical model will however be developed such that thermal effects can be included at a later stage.

1.5 Outline of Dissertation

In order to ensure that the overall results obtained in this investigation are accurate, it was important that the results of the various components are accurate. To this end, the fan model was rewritten in parallel, and the validated results are described in Chapter 3. To determine which was the most appropriate turbulence model for the numerical model, simulations were carried out using the various turbulence models available in FLUENT® . These results are presented in Chapter 4. The fan was subsequently scaled up to the required size of $d_{FC} = 10m$ as described in Chapter 5, and validated using the fan scaling laws. With the fan model validated in a parallel environment, the heat

exchanger was investigated as discussed in Chapter 6. With the fan model, appropriate turbulence model and the heat exchanger model validated, an ACHE was modeled in the manner discussed in Chapter 7.

Once the ACHE has been validated, a bank of ACHE's will be simulated. Initially, an investigation was performed to determine whether the numerical model produces the same trends as experimental data. The effect of ground clearance was investigated in Chapter 8, the effect of the presence of a walkway was investigated in Chapter 9 and the effect of a 2 dimensional array of ACHE's was investigated in Chapter 10. Finally the effect of wind on a bank of ACHE's will be investigated in Chapter 11. The dissertation will end off with conclusions and recommendations for further research.

Chapter 2

Literature review

2.1 Numerical Method

The method to be employed was the control volume formulation as applied to the Navier-Stokes equations. For this investigation the software package, FLUENT® was used for the investigation.

2.1.1 Navier Stokes equations

The governing equations for fluid flow are known as the Navier-Stokes equations. These equations are a set of partial differential equations that include the conservation of momentum and other fluid properties. The fluid properties are defined by the respective equations of state. The Navier-Stokes equations are solved using the finite volume method [13]. As previously mentioned, all of the simulations performed are considered to be steady state. Due to the low velocities involved, $M \ll 1$, the air is assumed to be incompressible.

Conservation of Mass

The equation for conservation of mass, also referred to as the continuity equation [13] , is :

$$div(\rho\vec{v}) = 0 \tag{2.1}$$

Where ρ is density, and $\vec{v}$ is the velocity vector.

Conservation of Momentum

The equation for the conservation of momentum for an incompressible fluid can be described by [14]

$$\nabla \cdot (\rho \vec{v} \vec{v}) = -\nabla p + \nabla \cdot (\bar{\bar{\tau}}) + \rho \vec{g} + S_m \tag{2.2}$$

Where p is the static pressure, g is the gravitational force, S_m is the momentum source term, and $\bar{\bar{\tau}}$ is the stress tensor. The stress tensor is defined as :

$$\bar{\bar{\tau}} = \mu \left[(\nabla \vec{v} + (\nabla \vec{v})^T) \right] \tag{2.3}$$

2.2 Reynolds-Averaged Navier-Stokes Equations

In typical engineering flows, turbulent eddies can exist on a scale varying from the microscopic scale to the same size scale as the geometry to be modeled. They can also exist for a very long or very short periods of time. This makes it necessary to have a very fine mesh, using a very small time step, to resolve the flow accurately. Due to the computational expense required, this is currently unfeasible.

The turbulent instantaneous velocity can be expressed as the sum of the averaged velocity and a fluctuating velocity [13].

$$u_i = \overline{u}_i + u_i' \tag{2.4}$$

Where $\overline{u}_i$ is the average velocity and u_i' is the fluctuating velocity. The average velocity is defined as

$$\overline{u}_i = \frac{1}{t} \int_{t_1}^{t_2} u_i dt \tag{2.5}$$

Where $t_1 \ll t \ll t_2$. Scalar quantities, like pressure, p, and density, ρ, are defined in a similar manner as seen in Equation 2.4 and 2.5. By definition the time average of the fluctuating value is 0. Substituting the time averaged variables into the instantaneous continuity and momentum equations produces

$$\frac{\partial}{\partial x_i}(\rho u_i) = 0 \tag{2.6}$$

and

$$\frac{\partial}{\partial x_j}(\rho\overline{u_i u_j} + \rho\overline{u_i' u_j'}) = -\frac{\partial p}{\partial x_i} + \frac{\partial}{\partial x_j}[\mu(\frac{\partial \overline{u}_i}{\partial x_j} + \frac{\partial \overline{u}_j}{\partial x_i})] + \rho b_i \tag{2.7}$$

After time-averaging over many fluctuations, terms that have fluctuating components in them, or factors there of, become zero. The only term that is not zero are those that have the product of two fluctuating terms [15]. Thus in Equation (2.7) the only fluctuating term left is $\rho\overline{u_i' u_j'}$. Equation 2.7 can now be rearranged to produce

$$\frac{\partial}{\partial t}(\rho\overline{u}_i) + \frac{\partial}{\partial x_j}(\rho\overline{u_i u_j}) = -\frac{\partial p}{\partial x_i} + \frac{\partial}{\partial x_j}[\mu(\frac{\partial \overline{u}_i}{\partial x_j} + \frac{\partial \overline{u}_j}{\partial x_i})] + \rho b_i - \frac{\partial}{\partial x_j}(\rho\overline{u_i' u_j'}) \tag{2.8}$$

The new terms, $\overline{u_i' u_j'}$ in Equation 2.8 are referred to as the Reynolds stresses. With the inclusion of the Reynolds stresses more unknowns then equations exist. This is known as the turbulence closure problem, as for a set of equation to be solved there must be at least as many equations as unknowns. Therefore in order to close Equation (2.8), some assumptions need to be made in order to solve for the Reynolds stresses. One of the methods uses the *Boussinesq Hypothesis*, which relates the Reynolds stresses to the mean velocity gradients [16]:

$$\rho\overline{u_i' u_j'} = \mu_t\left(\frac{\partial u_i}{\partial x_j} + \frac{\partial u_j}{\partial x_i}\right) - \frac{2}{3}\left(\rho k + \mu_t\frac{\partial u_i}{\partial x_i}\right)\delta_{ij} \tag{2.9}$$

Where μ_t is the turbulent viscosity, and δ_{ij} is the Kronecker delta. $\delta_{ij} = 1$ if $i = j$ and $\delta_{ij} = 0$ otherwise.

This approach is used for the so-called *RANS* turbulence models in FLUENT® , i.e. the Spalart-Allmaras, $k-\epsilon$, and the $k-\omega$ turbulence models to name a few. The Reynolds Stress Model (*RSM*) solves for each of the variables in $\overline{u_i' u_j'}$. In three-dimensions this is 9 equations, which reduces to 6 due to the symmetry of the matrix, $\overline{u_i' u_j'}$. The transport equation is then solved for each of the 6 stresses. A seventh equation for the dissipation rate is also solved in order too close Equations 2.8 and 2.6 [14].

2.3 Turbulence Models

FLUENT® has a number of turbulence models available, each with it's own advantages and disadvantages. Not all of the turbulence models will be applicable to a given

problem, and thus the various models need to be investigated.

2.3.1 Standard $k - \epsilon$

The $k - \epsilon$ turbulence model was proposed by Launder and Spalding [17], and is considered the workhorse for practical engineering flows. It is both robust, economical and has reasonable accuracy for a wide range of turbulent flows. The standard $k - \epsilon$ turbulence model is one of the "simplest 'complete' turbulent closure models" [14]. Launder and Spalding [17] advocate that physical realism, computational economy and range of applicability are best served by a two equation turbulence model that is solved in conjunction to those governing the mean flow behavior. The two equations are for the turbulence kinetic energy (k) and the dissipation rate (ϵ). This two equation model allows the turbulent velocity and length scale to be independently determined, by solving two separate transport equations. The model is semi-empirical, with the derivation relying on phenomenological considerations, and empiricism [14].

2.3.2 Renormalization Group (RNG) $k - \epsilon$

The RNG $k - \epsilon$ model is derived from the instantaneous Navier-Stokes equations, using a rigorous statistical technique called "renormalization group theory". It is similar in form to the standard $k - \epsilon$ turbulence model, but has different constants, and additional terms and functions in the k and ϵ transport equations. These additions make the RNG $k - \epsilon$ model more accurate and reliable for a larger class of flows. The RNG refinements include [14]:

- An additional term in the ϵ equation, which significantly improves accuracy of rapidly strained flows.
- Swirl effects on turbulence have been included to improve the accuracy of swirling flows.
- The RNG theory provides an analytical formula for the turbulent Prandtl number.
- An analytically derived differential formula for the effective viscosity that accounts for low Reynolds number effects.

2.3.3 Realizable $k - \epsilon$

The realizable $k - \epsilon$ turbulence model is another variation to the standard $k - \epsilon$ turbulence model. The term "realizable" implies that this turbulence model satisfies certain mathematical constraints, with regard to the Reynolds stresses, that are consistent with the physics of turbulent flow. The standard and the *RNG* $k - \epsilon$ turbulence models are not realizable.

The realizable $k - \epsilon$ turbulence model differs from the standard $k - \epsilon$ turbulence model in two important ways :

- The realizable $k - \epsilon$ turbulence model uses a new formulation for the turbulent viscosity.
- A new transport equation for the dissipation rate, ϵ, has been derived from an exact equation for the transport of the mean square vorticity fluctuation.

One of the benefits of this turbulence model is it's ability to better predict the spreading rate of both planar and round jets. It also has superior performance for flows involving rotation, boundary layers under adverse pressure gradients, separation and recirculation [14].

2.3.4 Standard $k - \omega$

The FLUENT® standard $k - \omega$ is based on the $k - \omega$ model of Wilcox [16], which incorporates modifications for low Reynolds number effects, compressibility and shear flow spreading. The Wilcox model predicts free shear flow spreading rates that show close agreement with experimental results for far wakes, mixing layers, and plane, round, and radial jets. This makes it applicable to wall bounded and free shear flows.

2.3.5 *SST* $k - \omega$

The shear stress transport (SST) version of the $k - \omega$ turbulence model was developed by Menter [18] to blend the robust and accurate formulation of the $k - \omega$ model in the near-wall region with the free stream independence of the $k - \epsilon$ model in the far-field regions. The SST $k - \omega$ model is similar to the standard $k - \omega$ model, but includes the following refinements:

- The model constants are different.

- The $k-\omega$ and the transformed $k-\epsilon$ equations are both multiplied by a blending function and added together. The blending function is such that for near-wall regions it becomes the $k-\omega$ model and the $k-\epsilon$ model for far away regions.
- It incorporates a damped cross-diffusion derivative term in the ω equation.
- The turbulent viscosity is modified to account for the transport of the turbulent shear stress.

This makes the SST $k-\omega$ model more accurate and reliable for a wider class of flows.

2.4 Axial Flow Fan Model

In order to allow the geometry to be simulated as a steady state problem the fan will not be physically modeled. Instead it will be replaced by an actuator disc. The actuator disc forces will be calculated using blade element theory. The actuator disc applies a momentum source term to the fluid, thus accelerating it through the disc [19], the affect of this acceleration can be seen in Figure (2.1). The fan model will be incorporated into FLUENT® by means a User Defined Function (UDF).

Von Mises [20] states that the force exerted on the fluid stream at any location within the actuator disc is dependent on the fluid velocity vector relative to the fan blade v_R, as well as the lift and drag characteristics of the fan blade cross-sectional area. Figure (2.2) shows the relationship between the relative velocity vector, v_R, the resulting lift, δ_L, and drag ,δ_D, at a radial co-ordinate, r.

The lift and drag force on a blade element is calculated using the following equations:

$$\delta_l = \frac{1}{2} C_l \rho \left|v_R\right|^2 \cdot c_{Fb} \cdot \delta r \tag{2.10}$$

$$\delta_d = \frac{1}{2} C_d \rho \left|v_R\right|^2 \cdot c_{Fb} \cdot \delta r \tag{2.11}$$

Where C_l and C_d are the coefficients of lift and drag respectively, c_{Fb} is the fan blade chord length and δr is the blade element radial thickness.

The coefficients of lift and drag are dependent on the fan blade profile. The fan blade chord length and the blade element radial thickness are all geometry based. Thus the only unknown in Equation (2.10) and (2.11)is the relative velocity vector. The velocity

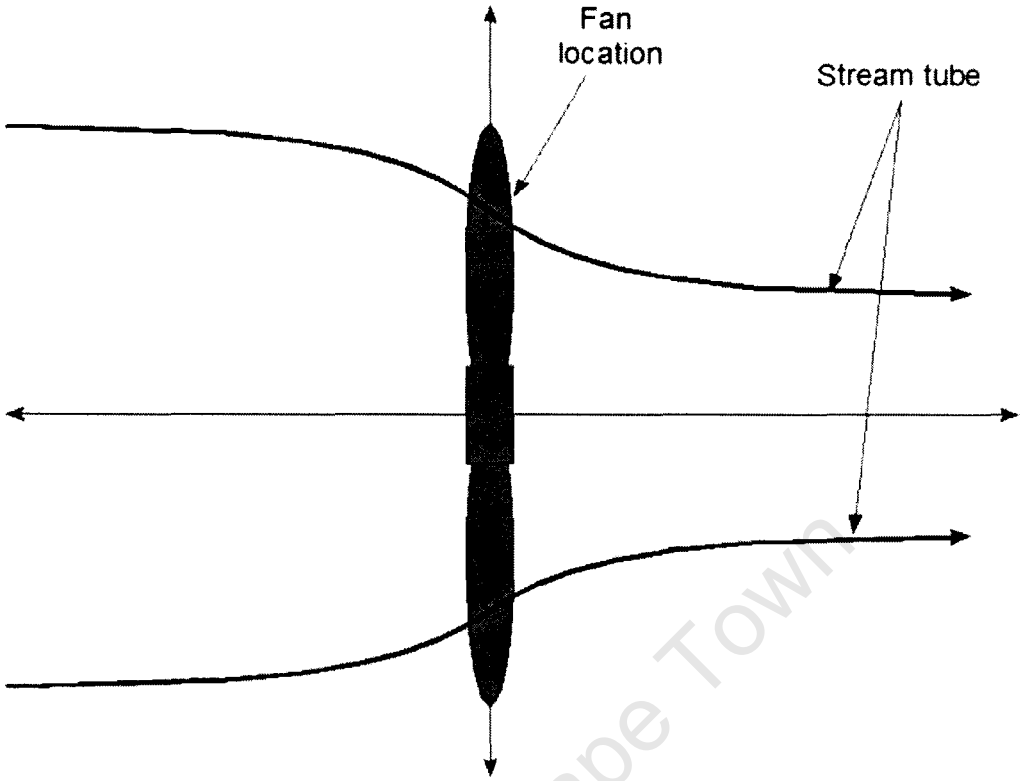

Figure 2.1: Stream tube showing fluid acceleration through the actuator disc

field experienced by the two-dimensional blade element differs from the uniform velocity field for which the coefficients of lift and drag are valid. The major difference is the tangential velocity component of the velocity field on the two-dimensional blade element downstream side [1]. To compensate for this, the relative velocity vector is the average of the trailing edge velocity vector, downstream and the free stream velocity vector upstream of the two dimensional blade element. This method has been found to produce better results than just using the upstream vector to calculate the relative velocity vector.

The thrust, δT, and the torque, δQ in Figure (2.2) are calculated using:

$$\delta T = \delta L \cdot cos\beta - \delta D \cdot sin\beta \tag{2.12}$$

$$\delta Q = (\delta L \cdot sin\beta + \delta D \cdot cos\beta) \cdot r \tag{2.13}$$

Where β is the angle between the relative velocity vector v_R and the fan blade plane of rotation. These blade forces are expressed as momentum sources/sinks in the Navier-Stokes equations, and thus need to be expressed as force per unit volume. Thus, it

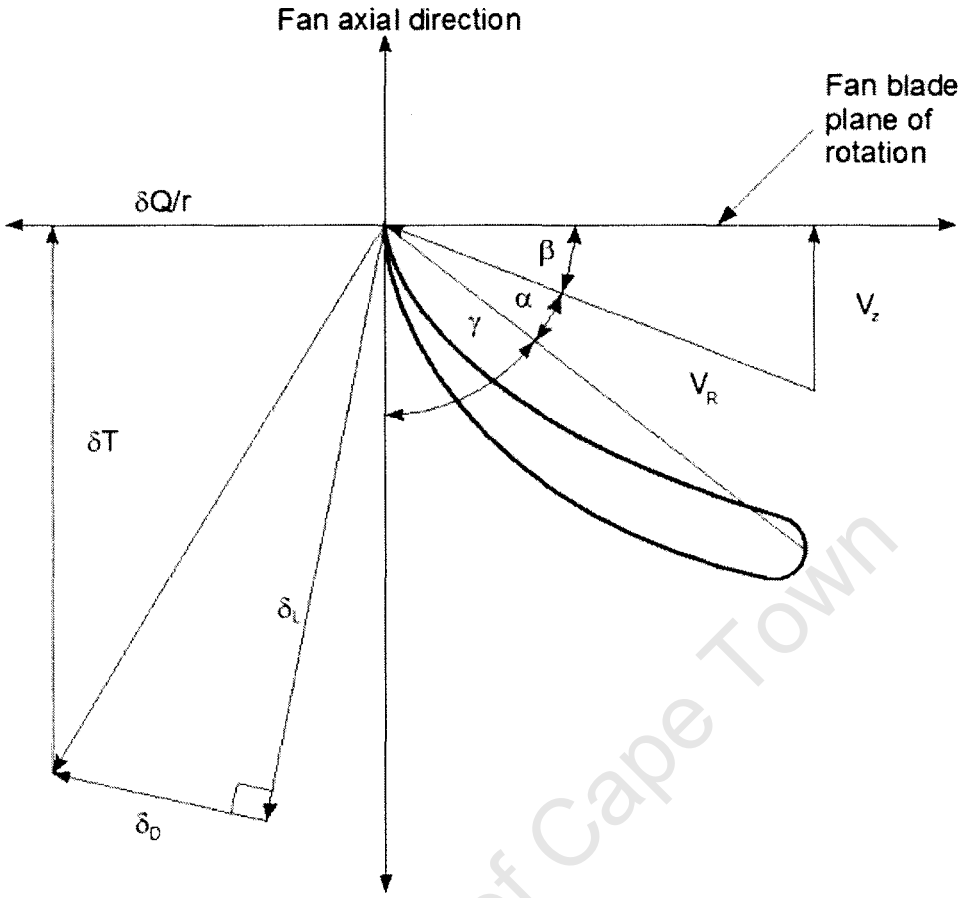

Figure 2.2: Blade element showing the geometric variables of importance

follows that :

$$\frac{\delta T}{\delta V} = \frac{n_{fb} \cdot \delta T}{2\pi r \cdot \delta r \cdot t_{Fr}} = \frac{\sigma \cdot \delta T}{c_{Fb} \cdot \delta r \cdot t_{Fr}} \tag{2.14}$$

$$\frac{\delta Q}{\delta V} = \frac{n_{fb} \cdot \delta Q}{2\pi r \cdot \delta r \cdot t_{Fr}} = \frac{\sigma \cdot \delta Q}{c_{Fb} \cdot \delta r \cdot t_{Fr}} \tag{2.15}$$

Where n_{fb} is the number of fan blades, t_{Fr} is the fan rotor thickness, as used in the numerical model, and $\sigma = \frac{c_{fb} n_{fb}}{2\pi r}$ is the solidity ratio. The solidity ratio is the ratio of fan blade area to the fan swept or actuator disc area [19]. Substituting Equation (2.10)-(2.13) into Equations (2.14) and (2.15) produces:

$$\frac{\delta T}{\delta V} = \frac{1}{2}\rho \overline{v_R}^2 \frac{\sigma}{t_{Fr}} (C_l \cdot cos\beta - C_d \cdot sin\beta) \tag{2.16}$$

$$\frac{\delta Q}{\delta V} = \frac{1}{2}\rho \overline{v_R}^2 \cdot r \cdot \frac{\sigma}{t_{Fr}} (C_l \cdot sin\beta + C_d \cdot cos\beta) \tag{2.17}$$

The lift and drag coefficients need to be calculated in order to solve Equations (2.16) and (2.17). Within a specified range of Mach numbers the lift and drag characteristics are a function of Reynolds number, Re, and angle of attack, α, alone. The angle between the blade chord and the fan's plane of rotation, the stagger angle, γ, is known at a given radial station, referring to Figure 2.2, it can be seen that the angle of attack is :

$$\alpha = \frac{\pi}{2} - (\gamma + \beta) \tag{2.18}$$

The lift and drag characteristics are taken from the NASA-LS profile, in accordance to the experimental results obtained by McGhee *et al.* McGhee *et al.* [21] experimentally investigated the NASA-LS profile, and plotted the dimensionless lift and drag coefficients, C_l and C_d against the angle of attack, α, for a range of Reynolds numbers. For angles of attack outside the range tested by McGhee *et al.* [21], the lift and drag characteristics of a flat plate are used. According to Hoerner and Borst [22] and Hoerner [23] the dimensionless lift and drag coefficient of a flat plate are respectively given as

$$C_l = C_{d_{max}} \cdot sin\alpha \cdot cos\alpha \tag{2.19}$$

$$C_d = C_{d_{max}} \cdot sin^2\alpha \tag{2.20}$$

Where $C_{d_{max}} = 1.98$.

A fourth order polynomial and trigonometric functions were used to ensure a smooth transition between the lift and drag characteristics of a flat plate and the NASA-LS profile. Linear interpolation is used to calculate the C_l and C_d values for other Reynolds numbers.

2.5 Heat exchanger model

A heat exchanger is a complex array of finned tubes, as can be seen in Figure 2.3. Air is forced through the heat exchanger and over the fins. The fins transfer the heat they acquired from the process fluid inside the heat exchanger tubes to the air passing over them. The geometry is thus complex, and it would be computationally expensive to model the heat exchangers explicitly. Therefore the heat exchangers will be modeled as a porous medium. The performance characteristics of the heat exchanger can then be replicated by specifying a viscous and inertial resistance to the porous region [14].

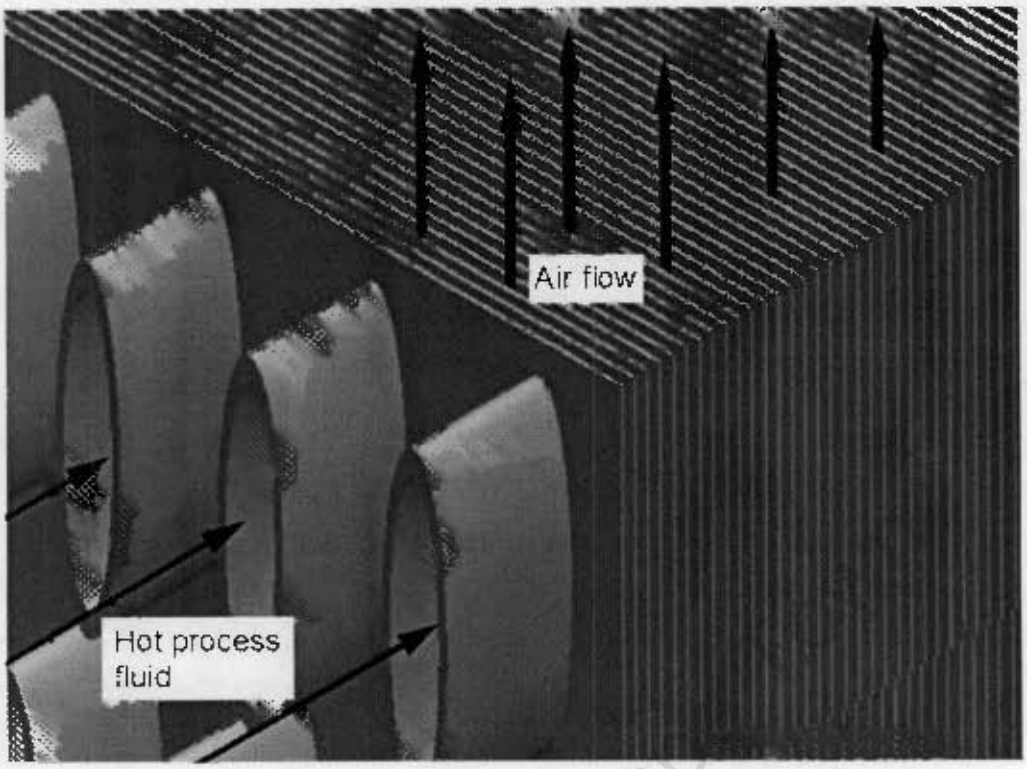

Figure 2.3: An isometric view of the heat exchanger, showing the cooling fins

2.6 Wind Velocity Profile

The velocity of wind is dependent on the height of measurement above the ground, due to viscous effects. In order to reproduce the effect of wind on the ACHE's, it is necessary to specify the wind profile it will experience. Due to the presence of obstacles upstream of the geometry as well as viscous effects the wind profile is not uniform. Some profile is required in order to account for this. The wind profile can be approximated by the $\frac{1}{7}^{th}$ Power Law [24, 25, 26]:

$$v(z) = v_{ref}\left(\frac{z}{z_{ref}}\right)^{n} \tag{2.21}$$

Where v is the mean velocity at the height z, v_{ref} is the free stream reference velocity, and z_{ref} is the reference height. The reference values, v_{ref} is the required velocity at height z_{ref}. The effect of the obstacles, or surface roughness can be included by changing the power n in Equation (2.21) [24]. Values between $n = \frac{1}{10}$ and $n = \frac{1}{3}$ were found in literature, varying for different conditions. Tulapurkara *et al.* [26] did experimental work involving a prismatic body and used $n = \frac{1}{7}$. Coetzee and du Toit [12] performed numerical work involving edge effects on a bank of ACHE's and used a value of $n = \frac{1}{5}$.

Since this investigation is a generic case, the default value of $n = \frac{1}{7}$ will be used.

2.7 Considerations for large scale flows

Some compromises are required due to the scale of the simulation. Due to the limitations of current computer architecture, the computational resources are limited. Although the fan model will be modified to run on a parallel computer cluster, the number of computers to be clustered is still finite. As the number of computers linked together increases the overall efficiency per machine decreases due to the communication requirements between the nodes. Thus the number of nodes required is kept to a minimum to ensure efficient use of resources. To do this the computational domain must be kept as small as possible, and as simple as possible.

By increasing the cell size, using a lower order discretization scheme, a single precision solver and ignoring boundary layers this can be achieved. This unfortunately comes at the cost of accuracy. Due to the larger cell size, sub-scale turbulent effects have to be modeled, instead of being resolved. This means that sub-grid phenomena, vortices etc., are not likely to develop. In this investigation only large scale effects (wind effects for instance) are of interest. Small scale effects are assumed to dampen out sufficiently to be assumed negligible.

The Large Eddy Simulation (LES) turbulence model resolves to a smaller scale then the RANS turbulence models, but is more time consuming, as it is inherently a transient turbulence model. Due to this increased expense the LES turbulence model will not be considered.

2.8 Conclusion

The numerical model must include a fan model, a means of simulating the heat exchanger bundles, and a means to simulate wind conditions. The fan model developed by Meyer [1] will be used to simulate the effects of the fan. The fan is modeled as an actuator disc, and the disc forces are calculated using blade element theory [1]. A porous region will be used to simulate the heat exchanger bundles [1, 27]. The wind profile will be simulated using the $\frac{1}{7}^{th}$ Power Law.

Chapter 3

Fan model verification

Before implementation of the fan model, it was essential to validate it. The code has already been validated in serial computing [1, 5, 11, 27]. Two fans were simulated to validate that the UDF worked in a parallel environment.

3.1 Fan description

The fan model is based on the B-fan designed and tested by Bruneau [3]. The B-fan is a eight bladed axial flow fan, that uses the NASA-LS blade cross sectional profile previously mentioned. The B-fan is a medium chord axial flow fan, with the blade chord and the twist increasing from the fan tip, to a maximum at the blade root, close to the hub [1]. The fan is molded fiber glass, with a smooth surface finish. The geometric characteristics are listed in Table (3.1). The variables used in Table (3.1) are shown in Figure (3.1)

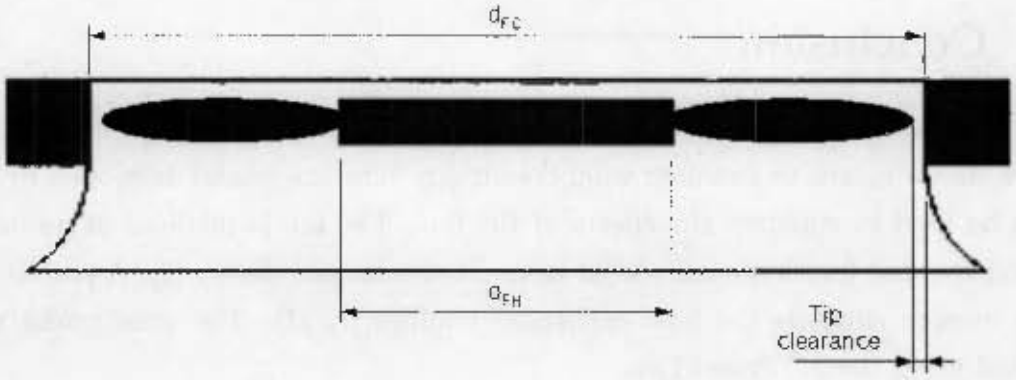

Figure 3.1: Schematic of a fan showing the variables of interest

Fan casing diameter	$d_{FC} = 1.542m$
Hub diameter	$d_{FH} = 0.4d_{FC}$
Tip clearance	$4mm$
Rotational speed	$N = 750rpm$

Table 3.1: Characteristics of the B-Fan tested by Bruneau [3] and Stinnes [4]

3.2 Geometry and Mesh Description

3.2.1 Geometry Dimensions

The performance characteristics of the B-fan were experimentally investigated by Stinnes and Von Backström [8]. The B-fan was tested using the standard configuration as described by the British Standard, BS 848 for a Type A installation, as seen in Figure (3.2a), as well as a modified configuration, shown schematically in Figure (3.2b). It was concluded that the fan performance characteristics were essentially unaffected by the difference between these two configurations.
Meyer [1] experimentally determined the performance characteristics for configurations depicted by Figure (3.2a) and Figure (3.2c). The fan performance characteristics were essentially the same. It was concluded that the fan characteristics for Figure (3.2d) should be an adequate measure for validation of the fan model.

The geometry to be modeled as shown by Figure (3.2d), is made up of 3 regions namely: the cylindrical region upstream of the fan, the fan swept region and the annular region downstream of the fan. The dimensions of the ducted fan can be seen in Figure (3.3). The 55mm region is the fan swept region. The fan swept region is region that will contain the actuator disc. Three identical discs that are $5mm$ thick are created, each of these discs is $20mm$ apart. The three $5mm$ discs are the inlet disc, the actuator disc and the outlet disc. The inlet and outlet discs are used to calculate the relative velocity vector, v_R, while the actuator disc is where the actuator disc forces are applied.

3.2.2 Mesh Description and Boundary Conditions

For the validation, two ducted fans with an annular region downstream of the fan were created using the geometry as seen in Figure (3.3). The geometry is set up such that the two fans control volumes are not connected. Using separate fans ensures that the

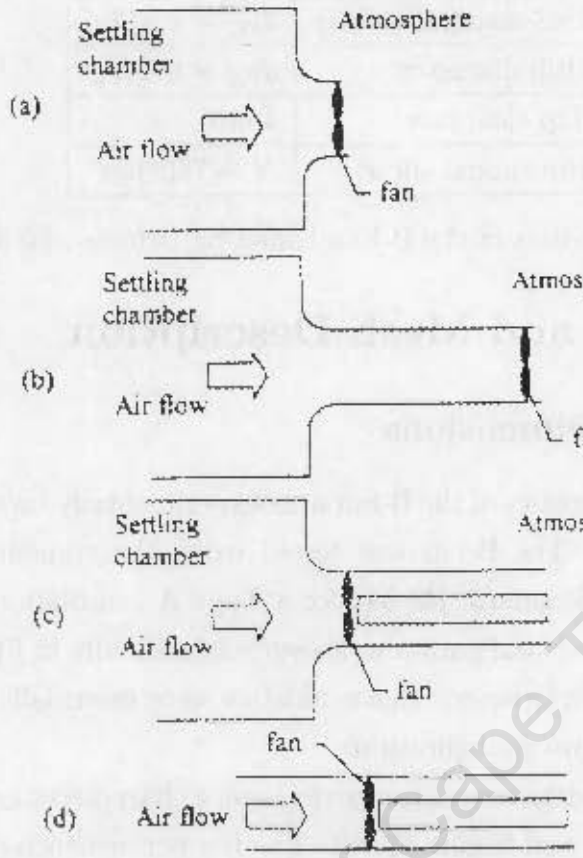

Figure 3.2: Different configurations of the fan test facility [1]

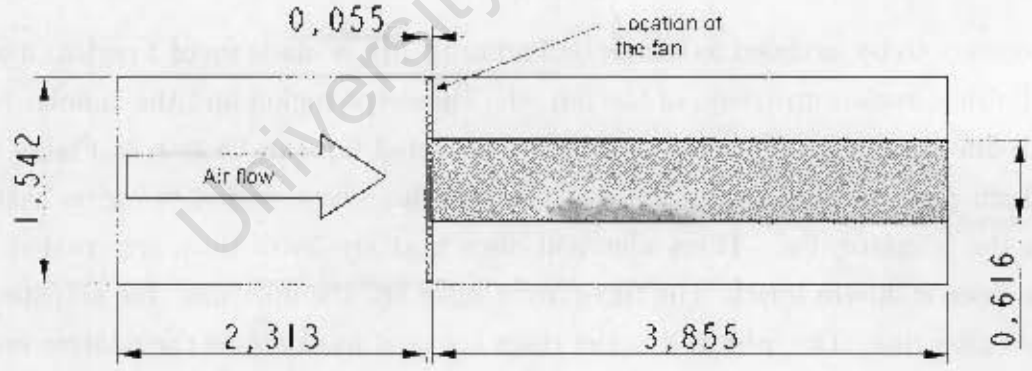

Figure 3.3: Dimensions of the validation geometry, in meters

flow field of one fan does not interfere with the other. The separation was done by placing separate ducted fan regions next to each other. These regions were connected with a seperating region of cells. To ensure separation of the ducted regions, the interface between this region of cells and the cylindrical section of the ducts was specified as a wall. This makes the duct's ontside surface homogeneous and keeps the ducted regions

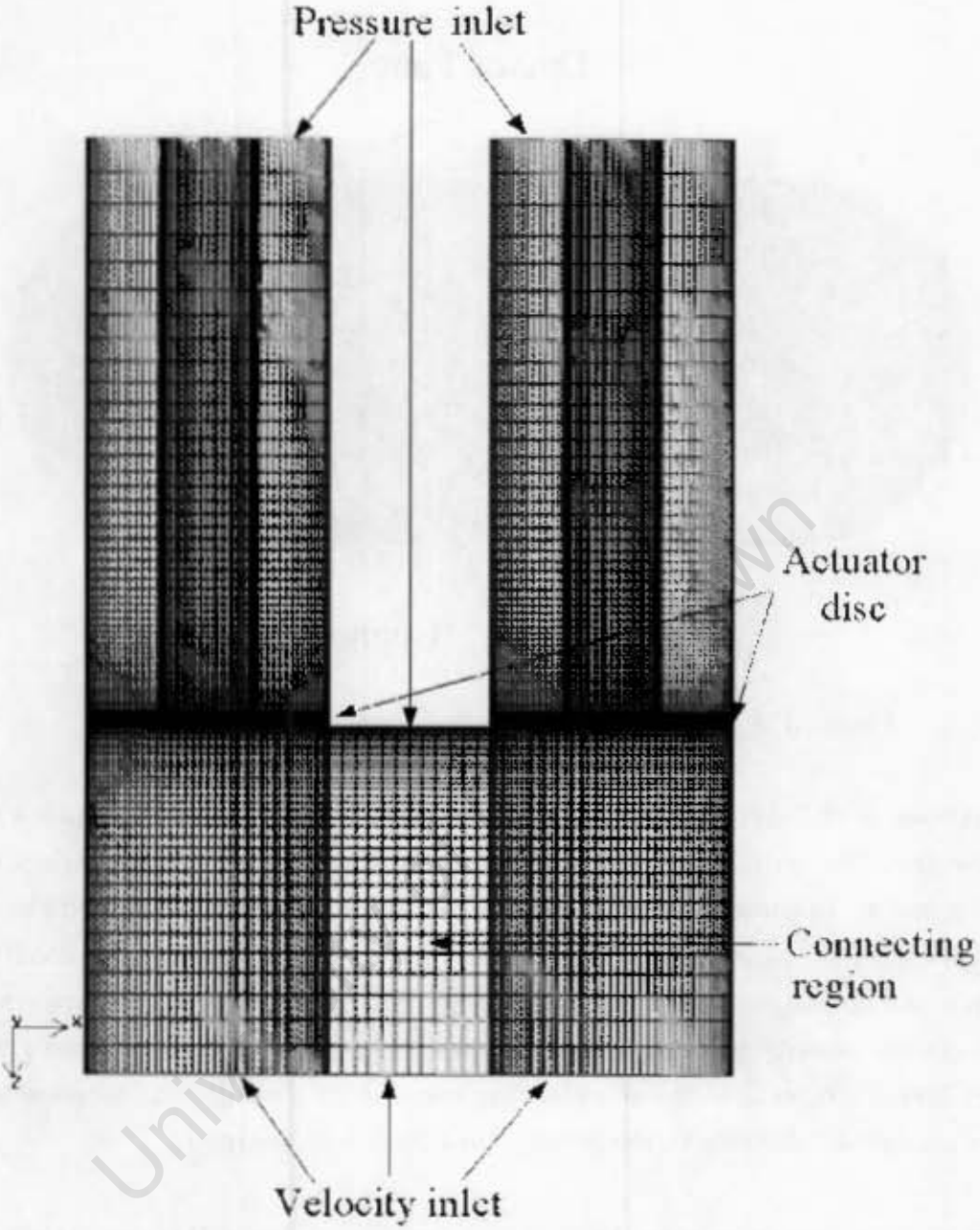

Figure 3.4: Plane view of the ducted fans, showing the boundary types

separate. The two ducted regions were created using the same dimensions. The amount of separation between the two ducts was irrelevant as long as they did not intersect; there will be no flow from one duct to the other.

As previously mentioned, the fan model averages the velocity upstream and downstream of the actuator disc. To do this two additional discs are created, one upstream and one

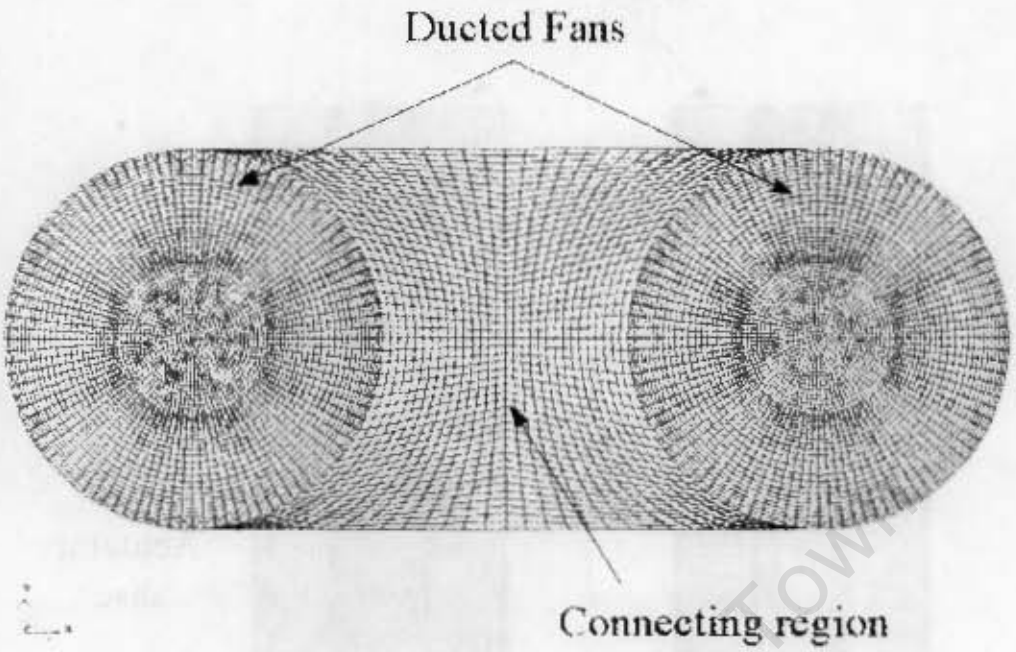

Figure 3.5: Front view of the ducted fans, showing disc mesh

down stream of the actuator disc. These two discs have identical dimensions to the actuator disc. The cells in the three disc's must be linked; linking is dependent on the cells' alignment. To ensure correct alignment, the three discs must be meshed identically such that each cell in the actuator disc has the same radial co-ordinate as a cell in the upstream and downstream discs, as seen in Figure (3.5). The linked cells are now used to average the velocity in the region of the fan. It was found by Hotchkiss [28] that between 2500 - 3000 cells in the actuator disc gave accurate results. An increase to 7000 made a negligible difference to the results, thus 2500 cells are used.

The fan swept region experiences large velocity gradients, due to the momentum source applied within the actuator disc. Thus the grid is finer near the actuator disc, as seen in Figure (3.4). The quality of the mesh in the connecting region of cells is irrelevant, as the flow here does not affect the fan performance characteristics.

The upstream boundary of the ducted region is set to a velocity inlet, which allows different flow rates to be simulated by changing the velocity. The down stream boundary is set to a pressure inlet, as shown in Figure (3.4). This was done because, in FLUENT® , a pressure inlet allows you to specify total pressure, whereas a pressure outlet only allows you to specify a static pressure. The duct perimeter was set as a wall. The three discs

were made to be distinguishable continuum volumes, so that they can be referenced by FLUENT® , and the actuator disc later.

FLUENT® 's double precision solver was used for the validation. The geometry was discretized using the first-order upwind differencing scheme. The standard $k-\epsilon$ turbulence model was used to account for turbulent effects, as it was used for the previous validations of the fan model.

To test the parallel aspect of the code, the fans will reside on separate nodes. This is done by partitioning the grid through the connecting band of cells, which ensures that the actuator discs are not split.

3.3 Fan Performance Calculations

The fan performance characteristics are defined by the fan static pressure rise Δp_{FS}, fan power consumption P_R and the fan static efficiency η_{FS} plotted as a function of the volume flow rate V. The fan performance characteristics were obtained in accordance to the British Standards Organisation's BS848 for a Type A installation. A Type A installation is one in which there is a free inlet and a free outlet, as shown in Figure (3.2). The numerical simulations were done for volume flow rates ranging from $V = 12m^3/s$ to $V = 19m^3/s$. The flow rate is specified by setting the velocity at the inlet boundary. Equation (3.1) is used to calculate the velocity to be specified in FLUENT®.

$$v = V/A \tag{3.1}$$

Where V is the volume flow rate, A is the area of the inlet, and v is the velocity perpendicular to the face, over which the area is calculated. The fan static pressure is calculate using Equation (3.2).

$$\Delta p_{FS} = p_2 - \left(p_1 + \frac{1}{2}\rho v^2\right) \tag{3.2}$$

Where p_1 is the inlet pressure, and p_2 is the outlet pressure, and ρ is the air density, and v is the velocity. The pressures are calculated as the area weighted average, over the boundary of interest.

The fan power is calculated using Equation (3.3):

$$P_R = \frac{2\pi}{60} QN \tag{3.3}$$

Where Q is the torque, which is calculated by the fan model, N is the rotational speed, specified in rpm. The value $N = 750rpm$ is used, as used by Bruneau [3] and Stinnes and Von Backström [8]. The fan static efficiency is calculated using Equation (3.4).

$$\eta_{FS} = \frac{\Delta p_{FS} V}{P_R} \tag{3.4}$$

3.4 Results of the parallelized fan model

The changes made to the fan model only involve the communication of data from one node to another. For this reason it is assumed that if the fan model works for one blade root stagger angle, it will work for the others that is has previously been validated for. The fan model has been validated for $\gamma_{root} = 58°$ to $\gamma_{root} = 62°$ For this investigation the blade root stagger angle $\gamma_{root} = 59°$ is used.

3.4.1 Comparison of the two fans

The first check was whether the two fans operate the same. They were created identically, and had the same boundary conditions. If the fan performance characteristics of the two fans differ greatly, then the parallelization of the UDF will have failed. From Table (3.2) it is clear that the two fans produce the same fan performance characteristics, and hence the parallelization of the fan model was successful.

3.4.2 Comparison with experimental results

The comparison of the numerical and experimental results was made using the results of one of the fans tested. The results of the numerical simulations show a good correlation to the experimental results. This can be seen graphically in Figures (3.6) to (3.8). The fan static pressure shows a good correlation; the worst correlation was for flow rate lower then that of the the peak fan static efficiency. The fan static power was under-predicted, which is similar to the findings by Meyer [1]. This was attributed to frictional losses not accounted for by the model, which include: physical rotational instabilities that increase

	Fan 1	Fan 2	Fan 1	Fan 2	Fan 1	Fan 2
V	Δp_{FS}	Δp_{FS}	P_R	P_R	η_{FS}	η_{FS}
(m^3/s)	(Pa)	(Pa)	(W)	(W)	$(\%)$	$(\%)$
12	286.296	286.283	5649.413	5648.740	60.8	60.8
14	258.420	258.417	5818.242	5817.612	62.2	62.2
15	239.186	239.183	5832.490	5831.868	61.5	61.5
16	216.033	216.034	5784.966	5784.347	59.8	59.8
18	157.431	157.439	5444.087	5443.540	52.1	52.1
19	126.582	126.583	5199.406	5198.914	46.3	46.3

Table 3.2: Comparison between the fan static pressure rise of the validation fans

the mechanical losses, as well as the tip effects caused by the fan blade tip clearance. The power does however produce the same trend. The over-predicted value for fan static efficiency is due to the under-prediction of the power, the trend is however the same.

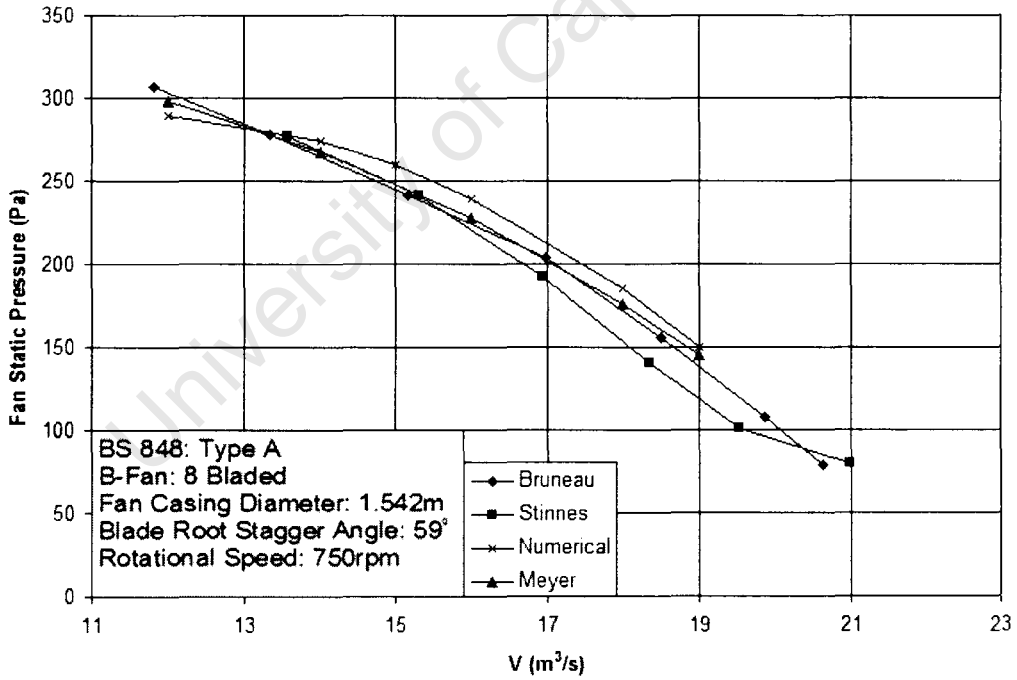

Figure 3.6: Comparison of fan static pressure rise vs. flow rate

It can be concluded that the fan model accurately simulates the flow field in the vicinity of an axial flow fan on a hexahedral mesh.

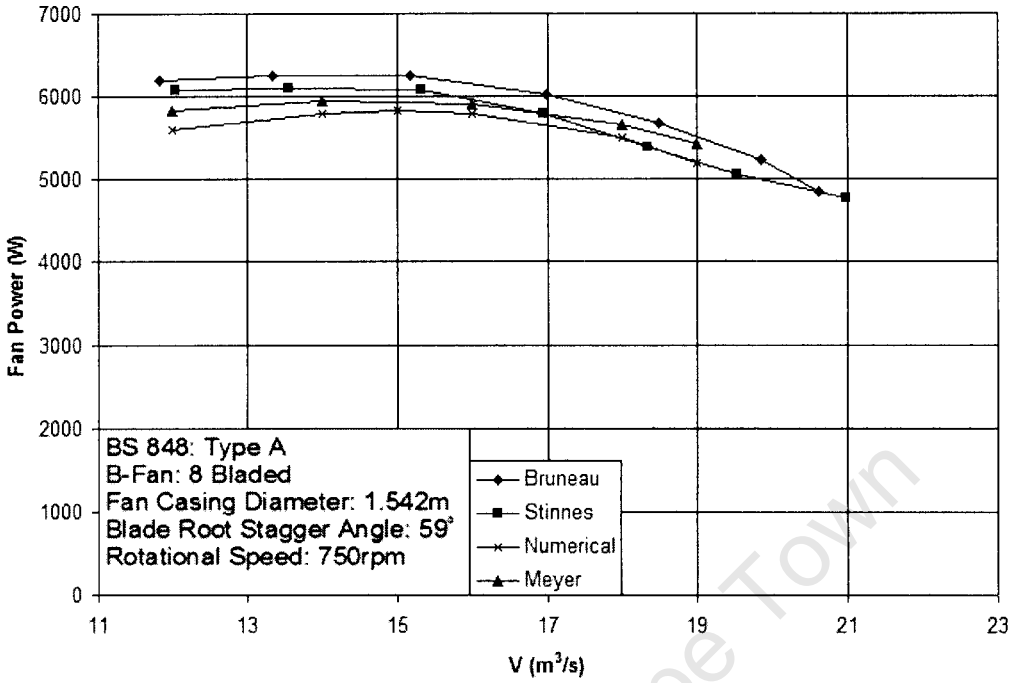

Figure 3.7: Comparison of fan power vs. flow rate

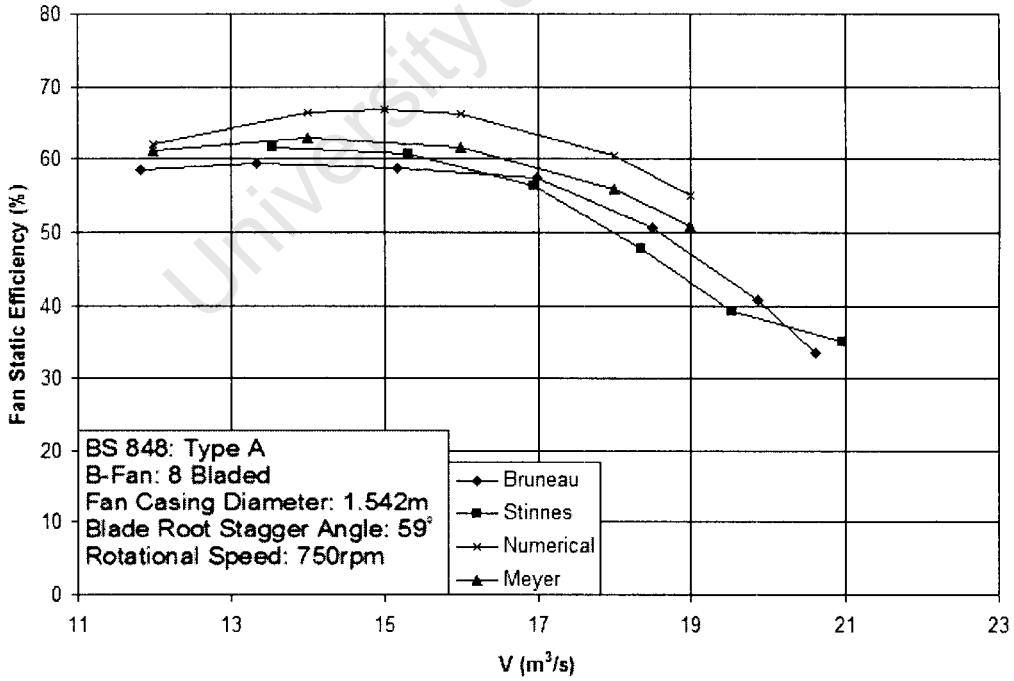

Figure 3.8: Comparison of fan static efficiency rise vs. flow rate

Chapter 4

Investigation of turbulence models

During the literature survey on wind profiles, it was obvious that the $k-\epsilon$ turbulence model is not appropriate for bluff body flow [29, 30, 31, 32]. This is due to the fact that the $k-\epsilon$ turbulence model over-predicts the production of turbulent kinetic energy, k. Since a wind profile will be used in the numerical analysis a more suitable turbulence model is required. An investigation of the effect of different turbulence models on the fan performance characteristics is required in order to ensure that the fan model reproduces the appropriate results using other turbulence models. Only the turbulence models available in FLUENT® will be evaluated, using the default constants in each case.

4.1 Geometry and Mesh Description

The level of convergence will be the criteria on which the turbulence models was eliminated, i.e. the turbulence models that do not allow the solution to fully converge will be discarded. This will eliminate turbulence models that require a higher mesh density in order to produce reasonable results. Since the geometry used for the fan model validation converged satisfactorily it will be used to investigate the appropriateness of the turbulence models.

The effect of the type of mesh on the results will also be investigated as the final mesh is unlikely to be a full structured mesh. A structured mesh consists of a regular arrangement of cells, where as an unstructured mesh does not. The plenum of the ACHE to be simulated is a delta plenum which forms a triangular prism. This makes a tetrahedral

mesh the obvious choice, as a hexahedral mesh will have skewed elements in the corners of the plenum. Using tetrahedral cells in the surrounding areas will also help reduce the cell count, as tetrahedral cells lend themselves well to cell size growth. Hexahedral cells get skewed if growth is required and if the volume they are created in is prismatic in nature. The overall cell count can be kept down, by having a sparsely meshed atmosphere surrounding the ACHE bank. Initially the turbulence models will be tested on the hexahedral mesh used in Chapter 3, then the tetrahedral mesh will be tested.

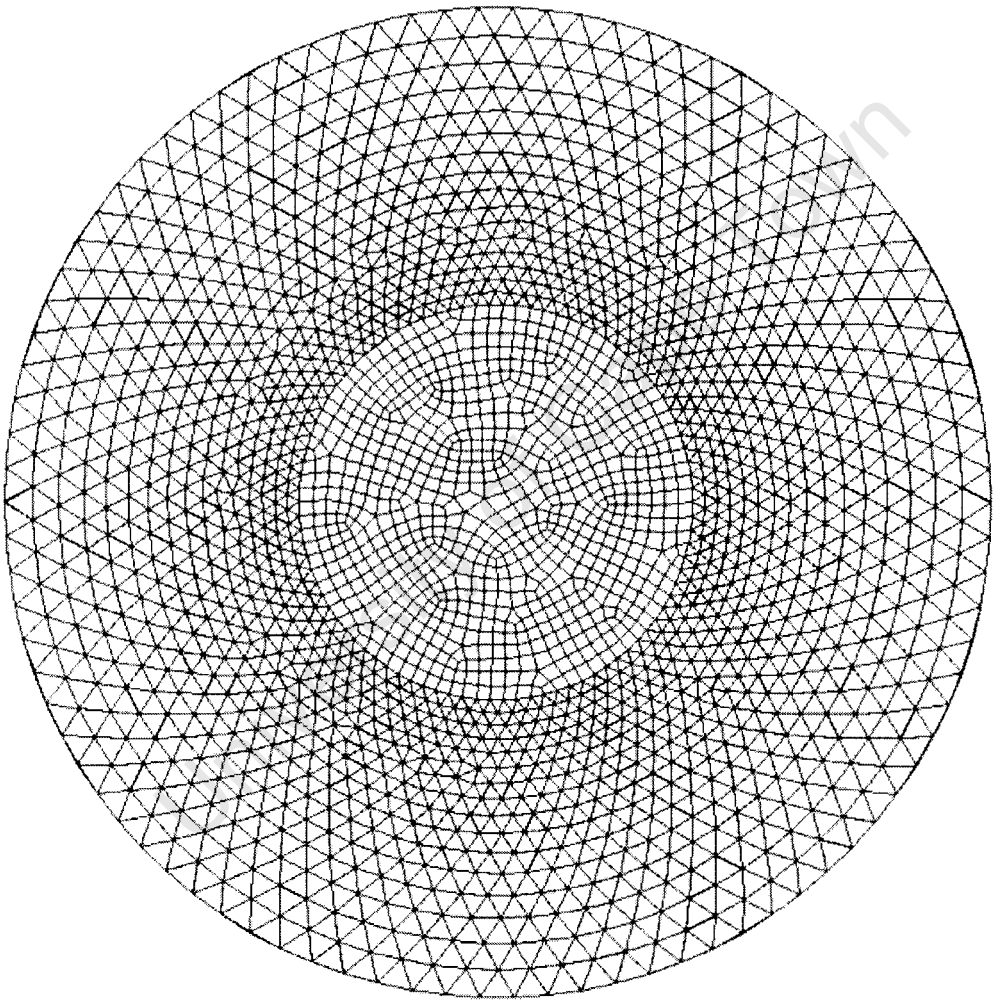

Figure 4.1: View of the tetrahedral mesh of the actuator disc

The fan swept region will be meshed using triangular prisms, such that the cells in the actuator disc and upstream and downstream discs are identical. The actuator disc contained approximately 2900 cells. The mesh can be seen in Figure (4.1). The turbulence models used on the tetrahedral mesh will be those that performed the best on the

hexahedral mesh.

4.2 Turbulence models

The turbulence models available in FLUENT® are as follows:

Turbulence Model	Version
$k-\epsilon$	Standard
	RNG
	Realizable
$k-\omega$	Standard
	SST
RSM	
Spallart-Allmaras	

Table 4.1: Turbulence models to be investigated

Some of the models have additional options to take care of a variety of flows, where this is the case the difference amongst the options will be compared.

4.3 Method

The simulations were performed in the same manner as they were for the validation, i.e., the flow rate will be varied and plotted against the fan static pressure, fan power and fan static efficiency. The results of Bruneau [3] were used for comparison.

The next turbulence model to be investigated will then be selected and the range of flow rates are tested again. For all cases standard wall functions were used, since the boundary layer will not be resolved in the large scale simulation.

4.4 Results and Discussion

Some of the turbulence models tested did not converge for some of, or all of the flow rates. This eliminates them as prospective options since the flow rate a wide range of

flow rates were required to be tested. The turbulence models that did not converge are as follows:

- The *RNG* $k - \epsilon$.
- The RSM turbulence model, along with various combinations of the options.
- The Spalart-Allmaras turbulence model.
- The SST $k - \omega$ turbulence model, along with various combinations of the options

Furthermore, some of the turbulence models reached the default turbulent viscosity ratio limit imposed by FLUENT® . These turbulence models are also deemed unsuitable, since the final solution will be affected by turbulent viscosity ratio limitation. If the turbulent viscosity ratio is limited the viscosity of the fluid has exceeded a realistic value. The only turbulence model to do this was the Standard $k - \omega$ model, including all possible variations of the options. The limitation occurred at the higher flow rates.

This leaves only the Standard $k - \epsilon$ and the Realizable $k - \epsilon$ turbulence models. The fan characteristic curves can be seen in Figures (4.2) - (4.4). It can be seen that the Standard $k - \epsilon$ is the better of the two over the whole range, while the Realizable $k - \epsilon$ turbulence model is slightly better for the higher flow rates.

Even though the standard $k - \epsilon$ turbulence model is unable to deal with bluff body flow, it will be used for all the simulations, including those that make use of the wind profile. When wind is applied to the simulations it could possibly degrade the fans performance, thus putting it in the region that the Realizable $k - \epsilon$ performs the worst.

Figures (4.5) - (4.7) show the comparison between a hexahedral grid and a tetrahedral grid. The comparison between the different mesh types did not produce an appreciable difference in results. The largest difference occurs at the lower flow rates.

The results from the tetrahedral grid are thus accurate enough for the current investigation. The large difference at the lower flow rates will result in the perimeter fans performing worse than expected.

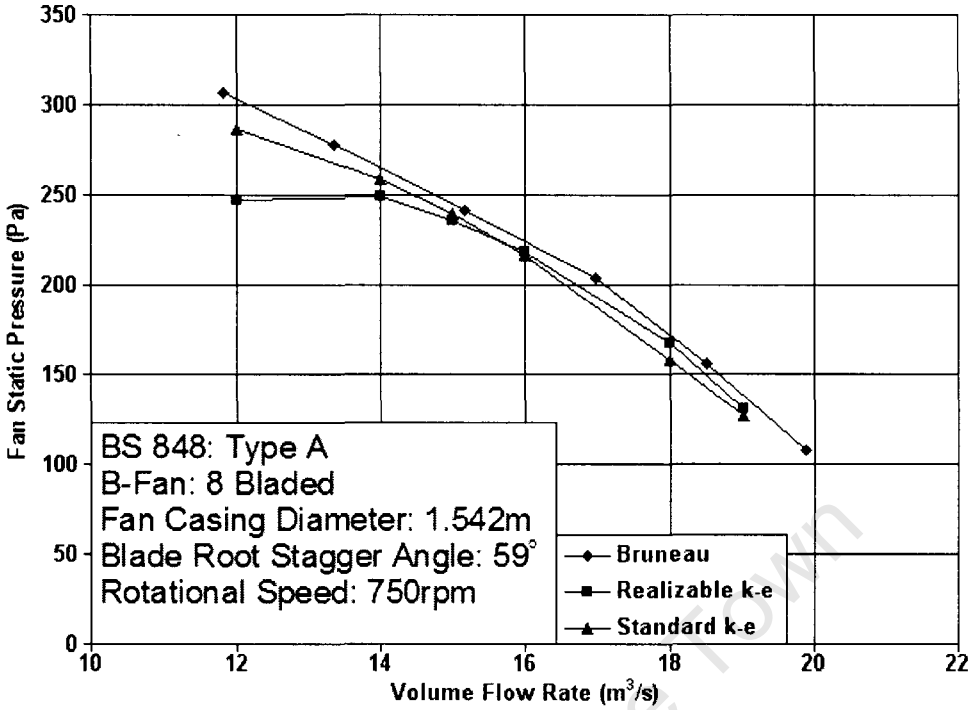

Figure 4.2: Comparison of the fan static pressure for different turbulence models

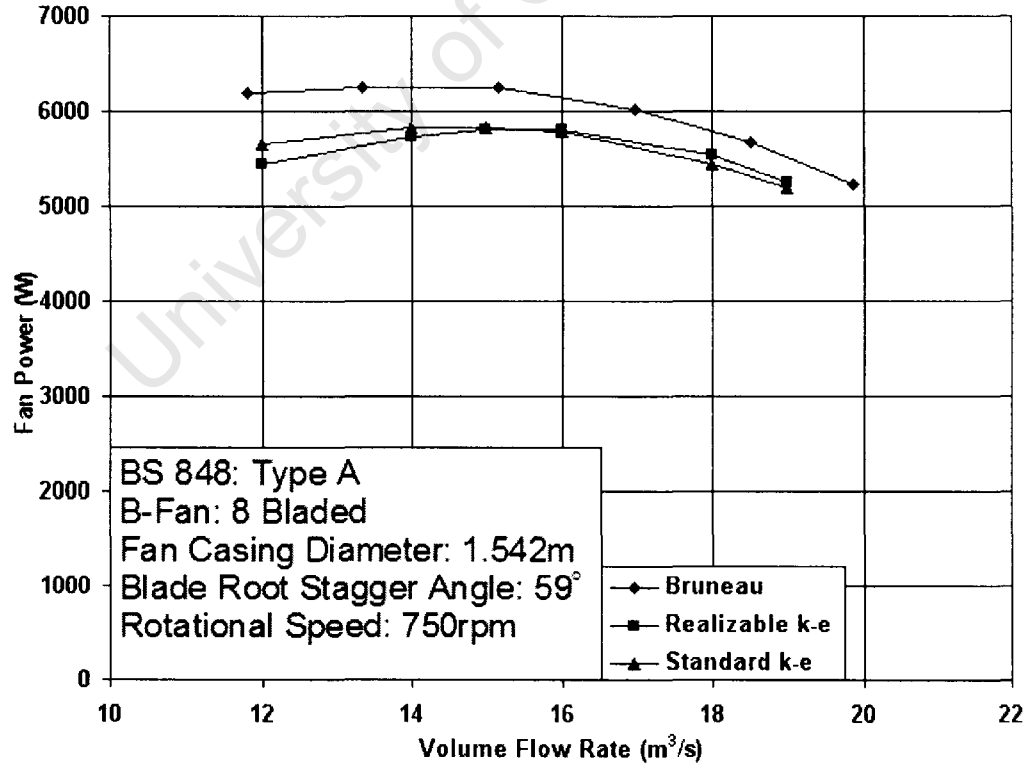

Figure 4.3: Comparison of the fan power for different turbulence models

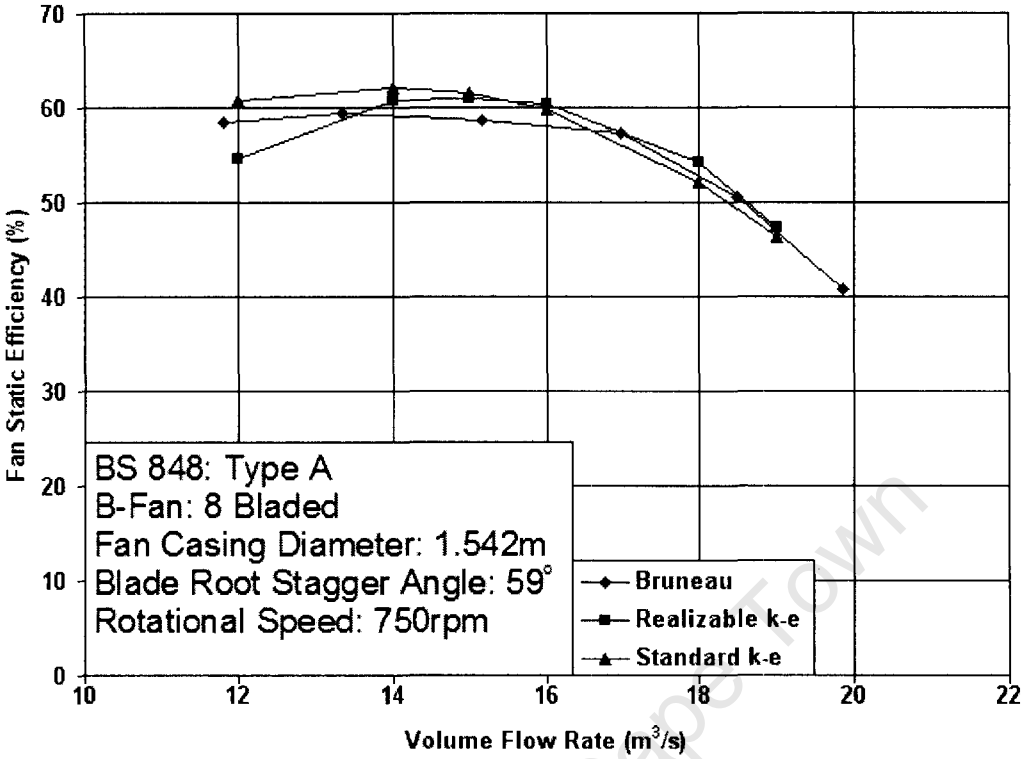

Figure 4.4: Comparison of the fan static efficiency for different turbulence models

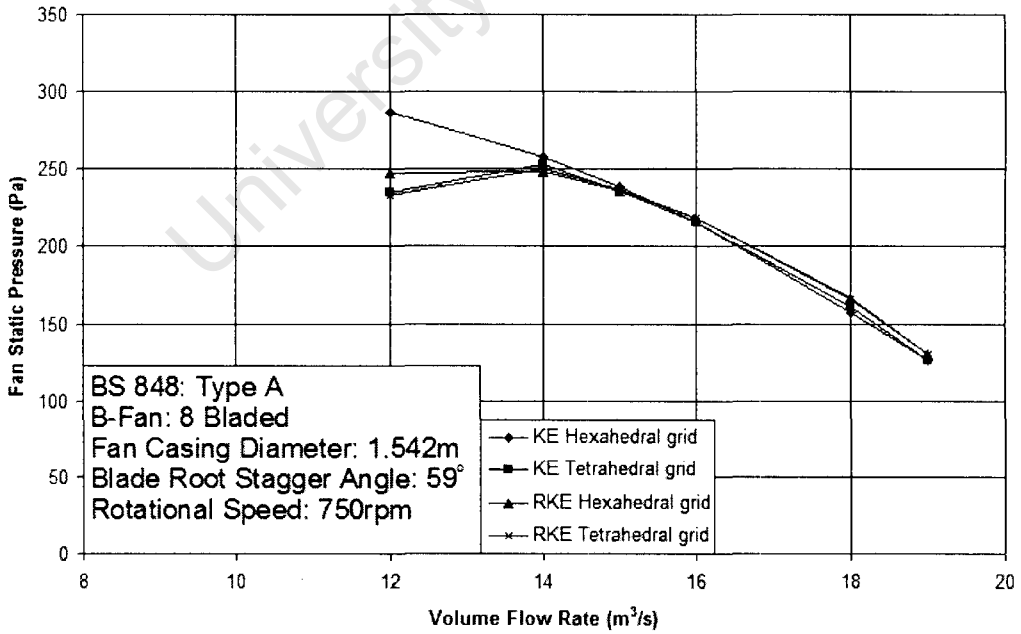

Figure 4.5: Comparison of tetrahedral and hexahedral mesh fan static pressure curves

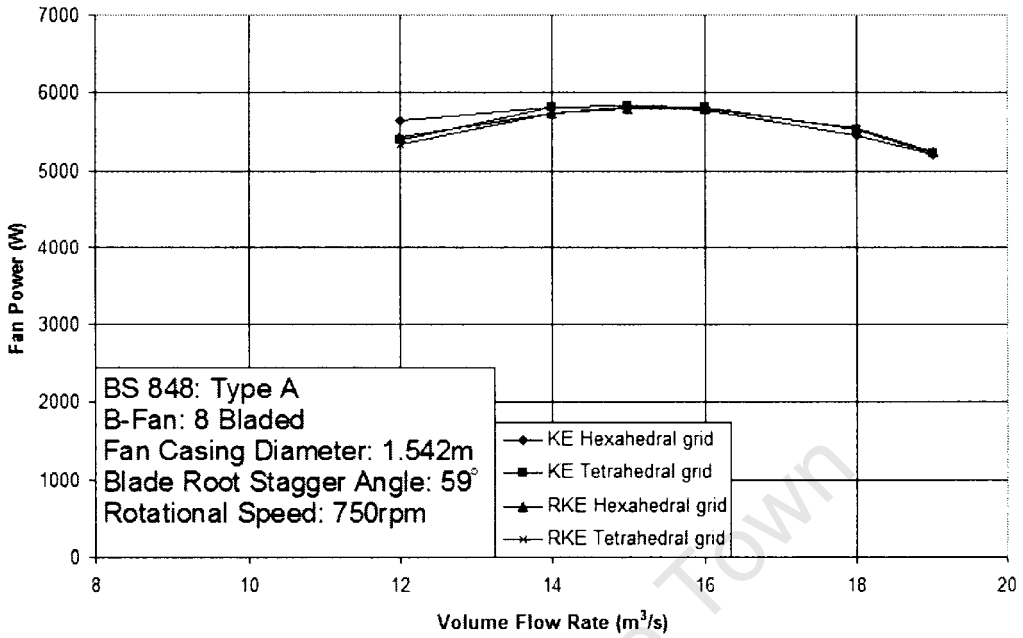

Figure 4.6: Comparison of tetrahedral and hexahedral mesh fan power curves

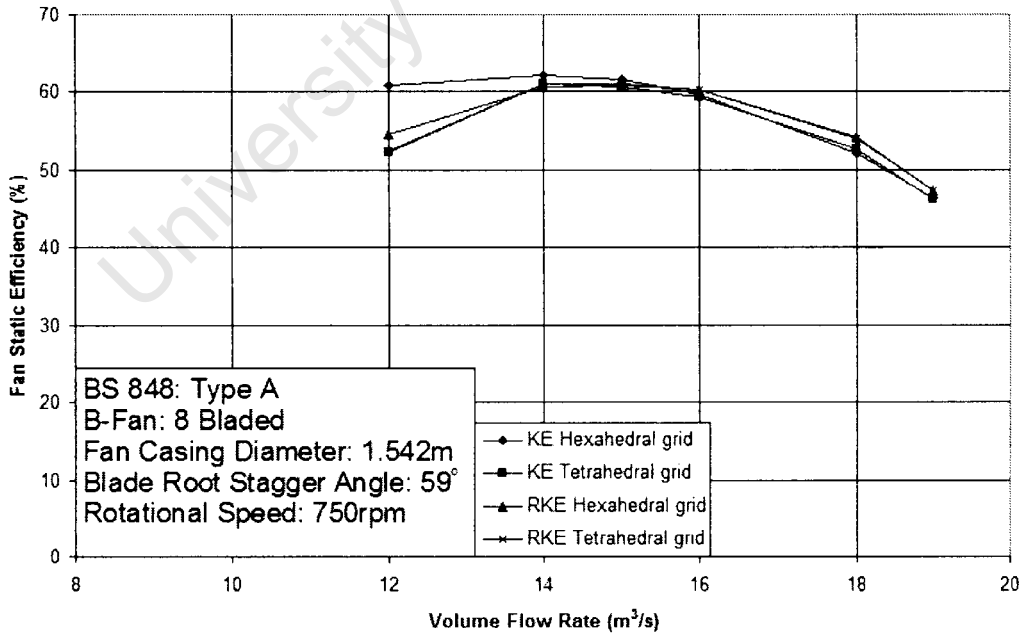

Figure 4.7: Comparison of tetrahedral and hexahedral mesh fan static efficiency curves

Chapter 5

Fan scaling investigation

The ACHE to be simulated has a fan diameter of $d_{FC} = 10m$. Therefore it is essential to validate the fan model for a fan of $d_{FC} = 10m$, in order to ensure that the fan model will work for a fan of this size, and produce meaningful results. Unfortunately there is no experimental data for a B-Fan of this size, therefore the fan scaling laws will be used as a comparison.

5.1 The fan laws

The fan laws are a set of equations that can be used to scale experimental result based on difference of the dimensions of the fans. The fan laws are based on the premise that fans of different sizes will have similarities in their respective velocity fields. The fan laws however do not make provision for fan blade Reynolds number and surface roughness differences [33]. The fan laws are as follows [6, 33]:

$$\frac{V'}{V} = \left(\frac{N'}{N}\right)\left(\frac{d'_{FC}}{d_{FC}}\right)^3 \tag{5.1}$$

$$\frac{\Delta p'_{FS}}{\Delta p_{FS}} = \left(\frac{N'}{N}\right)^2\left(\frac{d'_{FC}}{d_{FC}}\right)^2 \tag{5.2}$$

$$\frac{P'_R}{P_R} = \left(\frac{N'}{N}\right)^3\left(\frac{d'_{FC}}{d_{FC}}\right)^5 \tag{5.3}$$

$$\eta'_{FS} = \eta_{FS} \tag{5.4}$$

The primed values are those of the scaled fan.

5.2 Method

The scaled simulations are conducted in the same manner as those for the fan validation. The scaled values to be used were calculated first. According to Daly [34] excessive sound power levels are produced when the fan blade tip speed exceeds $60m/s$. For this reason the rotational speed of the large fan will be restricted to $N = 115rpm$. The flow rates used in Chapter 3 were scaled up to obtain the flow rates to be used for the scaled simulations. The flow rates range from $V = 500m^3/s$ to $V = 800m^3/s$. The large fan performance characteristics were then calculated. Similarly these are done the same way as described in Chapter 3. These measured values are then compared to the scaled values obtained by using the fan scaling laws. For the scaling validation only the best performing turbulence models are considered, namely the standard $k - \epsilon$ and the realizable $k - \epsilon$.

5.3 Results and Discussion

After initial simulations it was found that the solution failed to converge for the lowest flow rate to be tested ($V = 501.83m^3/s$). This was thought to be attributed to the re-circulation at the hub region of the actuator disk. Thus the actuator disk was re-meshed to contain three layers of cells, instead of one. This resulted in the solution converging. The correlation between the fan laws and the numerical results at lower flow rates is not as good as those at the higher flow rates. This is shown in Figures (5.1) - (5.3).

In an attempt to minimize the discrepancy, the actuator disk was re-meshed again to have six layers. The results were not appreciably different from the three layered actuator disk. Meyer and Kröger [33] performed a similar investigation using a fan with a diameter of $d_{FC} = 9m$. Instead of simulating the entire ducted region, only a thin axisymmetrical slice was modeled. The values obtained showed a better correlation than those of the current investigation. For this reason this geometry was investigated to see if the error is due to the large scale used. Due to the axisymmetric nature of the study, the flow could be constrained in a manner present in the full three-dimensional model. In an axisymmetrical model the flow leaving the periodic boundary is made to enter the other periodic boundary in the same manner that it left, this could dampen out the flow field.

The geometry used for the comparison with Meyer and Kröger [33] can be seen in Fig-

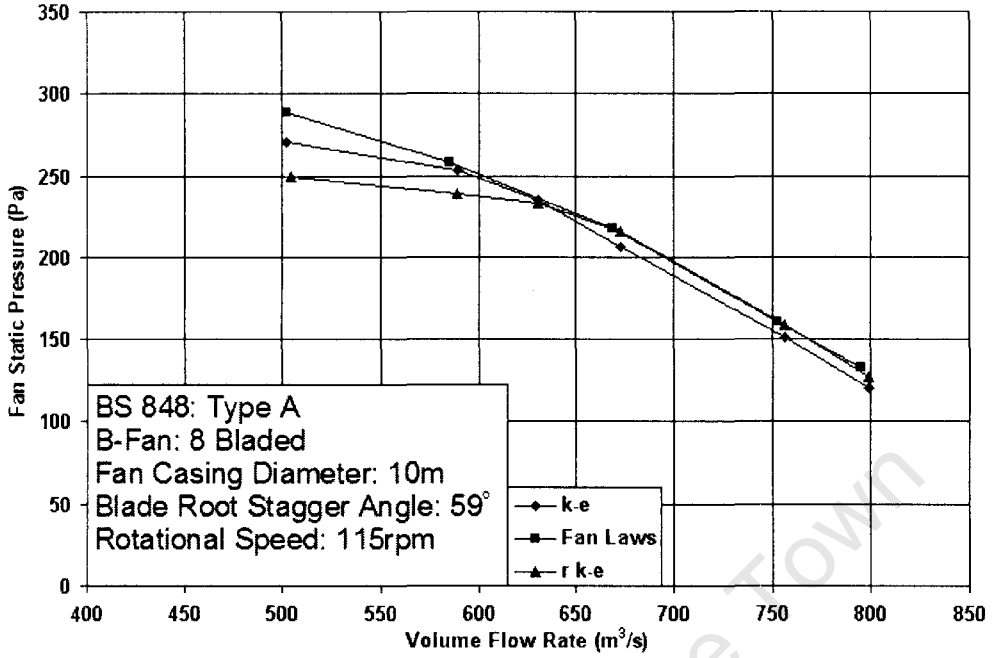

Figure 5.1: Comparison of the scaled fan static pressure curves

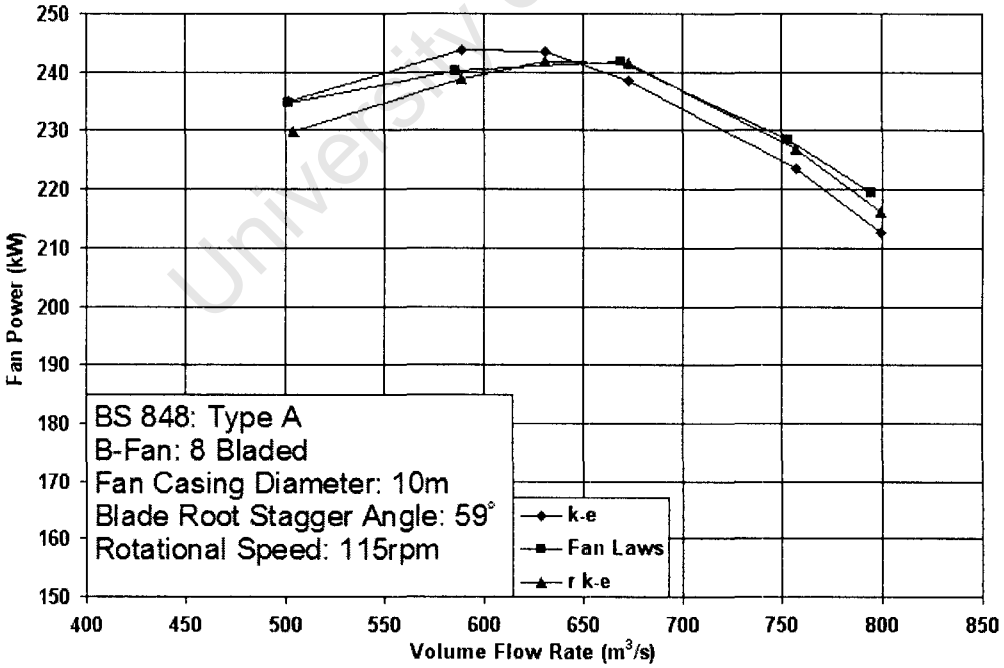

Figure 5.2: Comparison of the scaled fan power curves

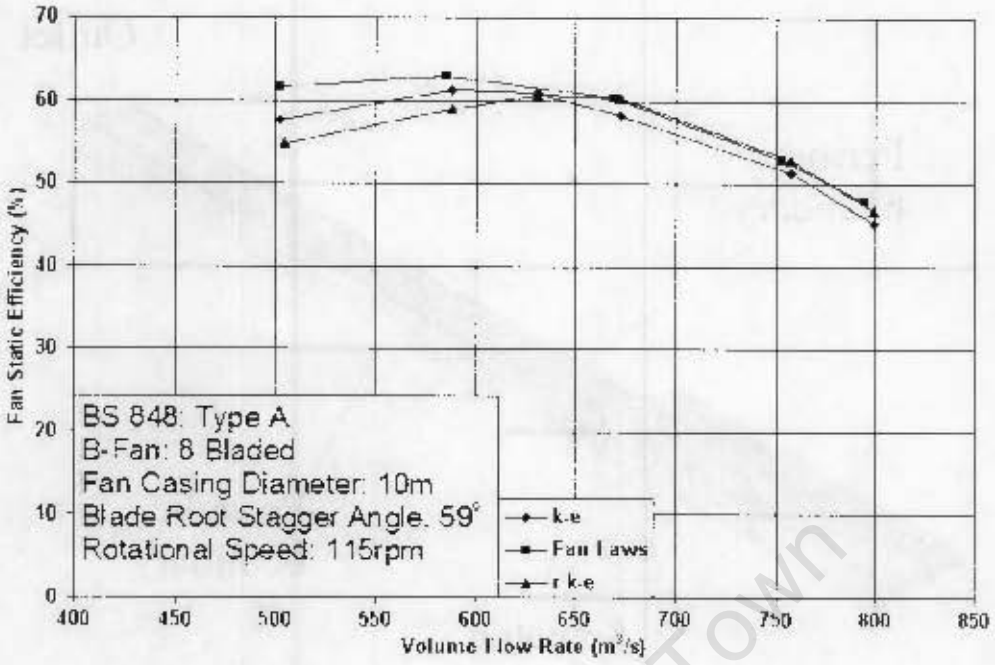

Figure 5.3: Comparison of the scaled fan static efficiency curves

ures (5.4). The boundary conditions and modeling constants were set up in the same manner as for the other validations. The root stagger angle was changed to $\gamma_{root} = 61^{\circ}$, and the fan diameter to $d_{FO} = 9m$ as used by Meyer and Kröger [33]. The results are shown in Figure (5.5) - (5.7).

In these simulations it is evident that the axisymmetric model performs better then the full model, but it still does not reproduce the results obtained by Meyer and Kröger [33]. The major difference between the two investigations is that Meyer and Kröger [33] used the CFD package Flo++ whereas these simulations are done in FLUENT® .

In order to investigate the effect of the boundary conditions on these results the outlet boundary types were changed. The types investigated were: pressure inlet, pressure outlet, mass flow inlet, outflow and outflow vent. These had a negligable effect to the fan performance curves. The parallelized fan model was also substituted for the original fan model, to ensure that the modifications did not affect the solution. The original fan model made no change to the solution obtained. The results of these investigations are omitted due to the similarity to the previously shown results. For this reason it was concluded that the difference in solution can be attributed to the difference in CFD package.

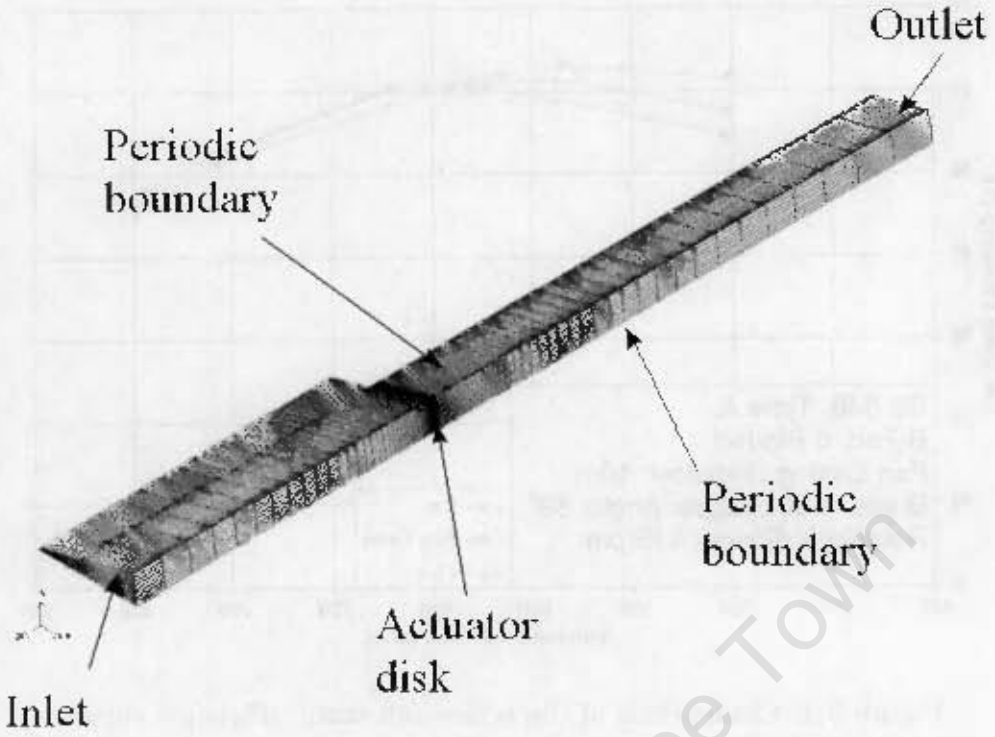

Figure 5.4: Geometry used for the axisymmetric model

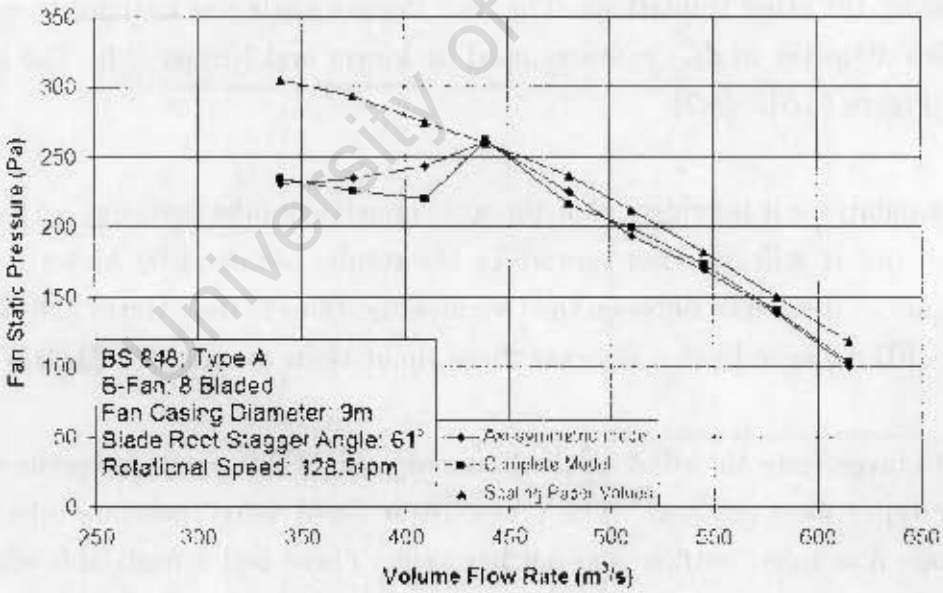

Figure 5.5: Comparison of fan static pressure for an axi-symmetric model and a full three-dimensional model

From the results obtained in this investigation it was evident that it might be problematic to implement the fan model at a large scale. It was observed that the fan

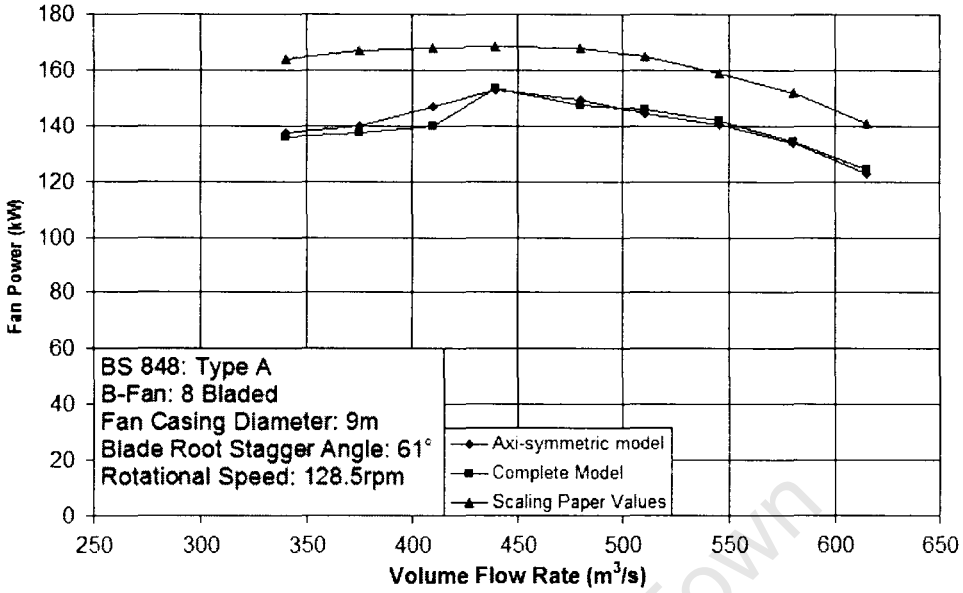

Figure 5.6: Comparison of fan power for an axi-symmetric model and a full three-dimensional model

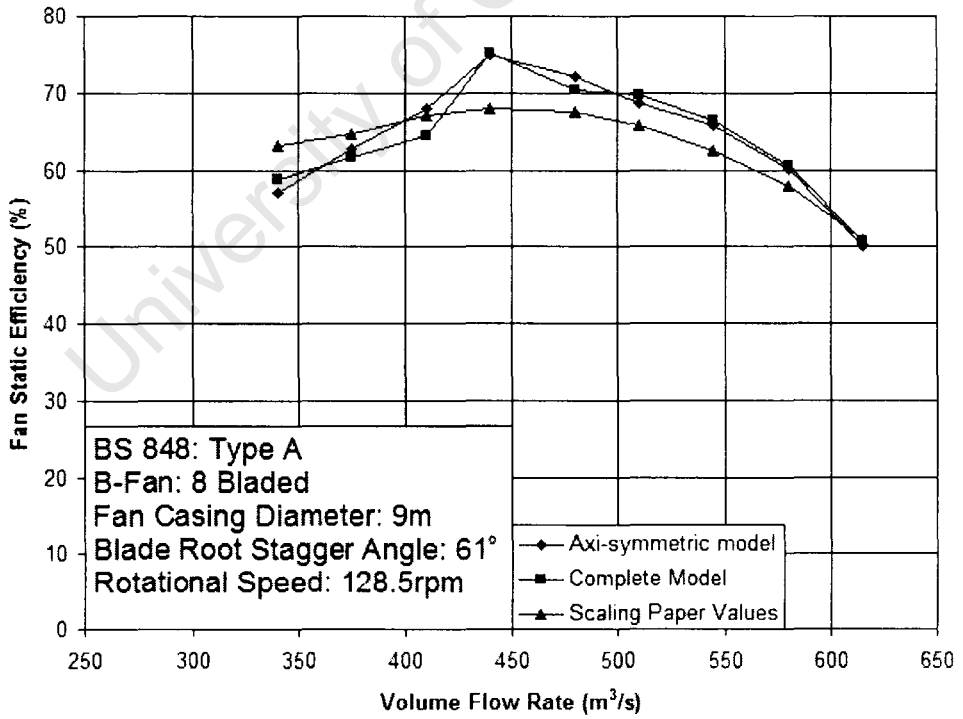

Figure 5.7: Comparison of fan static efficiency for an axi-symmetric model and a full three-dimensional model

performance characteristics deviate from the scaled numerical results at the lower flow rates. It is expected that the flow rate of some of the fans in the ACHE, which is yet to be tested will be lowered due to inlet losses. Hence at the large scale some of the simulations might not converge.

Chapter 6

Heat exchanger calibration

Every heat exchanger has a certain set of performance characteristics which gives an indication of how the flow over the heat exchanger is affected. For this investigation to produce meaningful results, the fluid passing through the porous region must behave in the same manner as a heat exchanger.

6.1 Heat exchanger description

The heat exchangers to be simulated are elliptical tube, rectangular plate fin heat exchangers [35]. The combination of the elliptical tube and the fins ensures that the air passing over the heat exchanger exits perpendicular to the plane of the heat exchanger. The heat exchangers was modeled as a rectangular volume that has the same dimensions of the heat exchanger bundle. This volume can therefore be coarsely meshed as the fins and the elliptical tube are omitted.

The heat exchanger performance curve gives an indication of the pressure drop across the heat exchanger for a given velocity. In order to reproduce the heat exchanger performance curve the rectangular volume was defined as a porous medium. FLUENT® makes it possible to specify the direction of the porosity. In so doing the flow can be restricted in the plane of the heat exchanger, and only allow flow perpendicular to it. FLUENT® also makes provision for a flow resistance to be applied in the porous medium, thereby applying a resistance to air flowing through the volume.

The flow resistance of the heat exchanger is dependent on the velocity of the flow through it. The resistance can be specified as either a viscous or an inertial resistance,

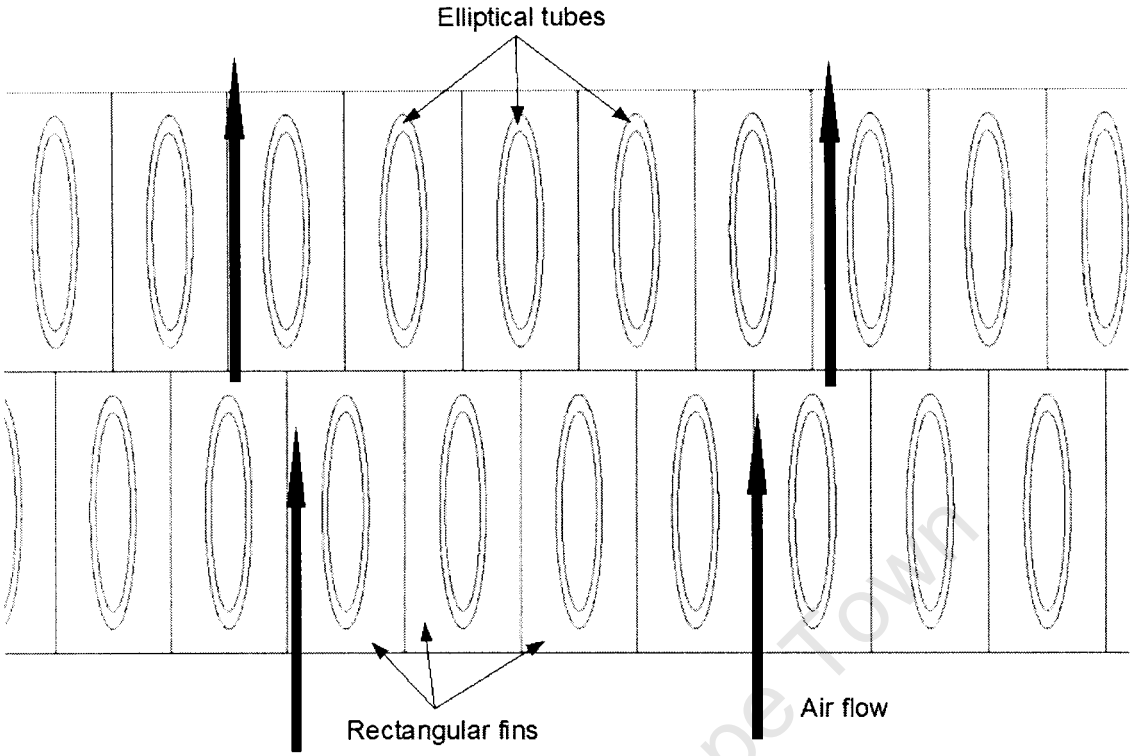

Figure 6.1: Cross sectional view of the heat exchanger, showing the tubes that contain the process fluid

or both. To ensure that the flow was perpendicular to the plane of the heat exchanger the resistance in the plane of the heat exchanger was specified as being much higher. FLUENT® recommends setting the inertial resistance be at least a 1000 times larger in the plane of resistance [14].

6.2 Empirical Analysis

Kröger [6] performed numerous experiments with heat exchanger and developed a set of empirical equations that define the pressure drop characteristics of a set of heat exchangers. These equations will be used to develop the characteristic curve of the heat exchanger to be used for the simulations.

6.2.1 Governing Equations

The pressure drop created across a heat exchanger is described as follows [6]:

$$\Delta p_t = K_{\theta t} \cdot \frac{1}{2} \rho v_{HE}^2 \tag{6.1}$$

Where Δp_t is the total pressure drop across the heat exchanger which must be supplied by the fan, $K_{\theta t}$ is the total loss co-efficient of a heat exchanger in a delta configuration, and v_{HE} is the air velocity through the heat exchanger. $K_{\theta t}$ is the sum of all the losses incurred due to the heat exchanger configuration.

The losses that are taken into account are :

- The pressure drop across the heat exchanger itself, K_{HE}
- The loss due to the fluid contraction at the inlet of the fins, K_{ci}
- The downstream jetting loss, K_{dj}
- The outlet losses K_o

Thus it follows that:

Total loss = (heat exchanger loss) + (inlet contraction loss, corrected for oblique flow) + (jetting loss) + (outlet loss)

Or

$$K_{\theta t} = K_{HE} + \left(\frac{1}{sin\theta_m} - 1\right)\left[\left(\frac{1}{sin\theta_m} - 1\right) + 2K_{ci}^{0.5}\right] + K_{dj} + K_o \tag{6.2}$$

The value of K_{HE} is calculated using the following relationship

$$K_{HE} = a(R_y)^b \tag{6.3}$$

Where a and b are heat exchanger constants, and R_y is the characteristic flow parameter, defined as

$$R_y = \frac{\rho v}{\mu} \tag{6.4}$$

θ_m is the mean flow incidence angle, formed by a semi-apex angle of θ, is determined using

$$\theta_m = 0.0019\theta^2 + 0.9133\theta - 3.1558 \tag{6.5}$$

The inlet contraction loss, K_{ci} is caused by the fluid separation at the entrance of the heat exchanger fins, and is calculated using the following equations:

$$K_{ci} = \frac{K_c}{\sigma_{21}^2} \tag{6.6}$$

$$K_c = \left(1 - \frac{1}{\sigma_c}\right) \tag{6.7}$$

$$\begin{aligned}\sigma_c = {} & 0.6144517 + 0.04566493\sigma_{21} - 0.336651(\sigma_{21})^2 + 0.4082743(\sigma_{21})^3 \\ & +2.672041\sigma_{21}^4 - 5.963169\sigma_{21}^5 + 3.558944\sigma_{21}^6\end{aligned} \tag{6.8}$$

Where K_c is the contraction loss, σ_c is the contraction ratio, σ_{21} is the ratio of the flow area between the fins at the leading edge to the corresponding area upstream of the fins. For this configuration the value of $\sigma_{21} = 0.875$ was used [6].

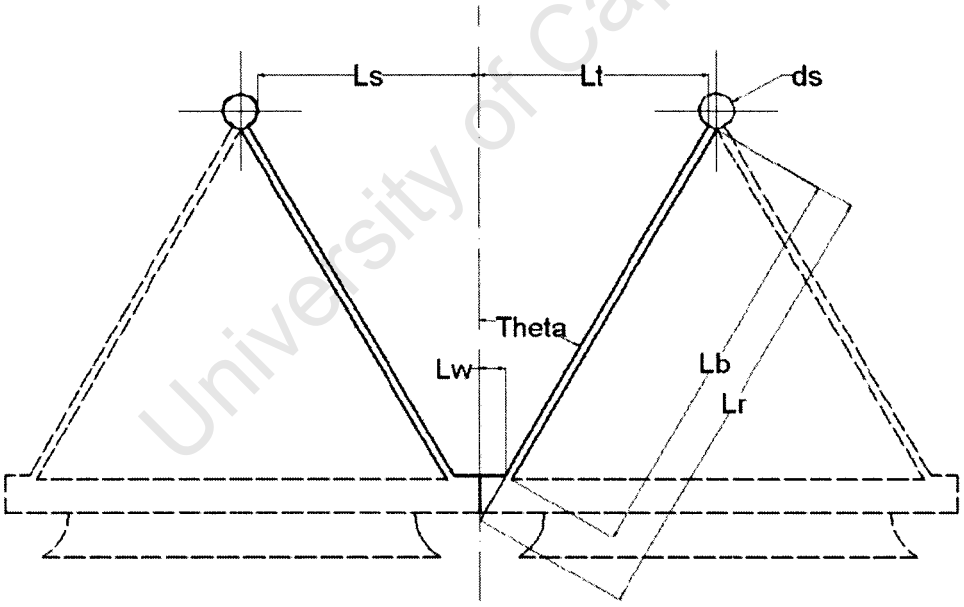

Figure 6.2: Schematic of the ACHE, showing the dimensions that affect the loss

The jetting loss is attributed to the reduction in the area which the flow must pass through. The air leaves the heat exchangers perpendicularly, and is then forced through the space between the steam ducts. The jetting loss can be calculated using the following

equation:

$$K_{dj} = \left[\left(2.93291\left(\frac{L_w}{L_b}\right)^2 - 2.89188\left(\frac{L_w}{L_b}\right)\right)\left(\frac{L_b}{L_s}\right)\left(\frac{L_t}{L_s}\right)\left(\frac{28}{\theta}\right)^{0.4} + \left(\frac{L_b}{L_r}\right)\left(e^{-3.3797x10^{-3}\theta^2+5.8601x10^{-2}\theta+2.36987}\left(\frac{L_s}{L_t}\right)\right)^{0.5}\right]^2 \quad (6.9)$$

The variables in Equation 6.9 are shown in Figure (6.2). Finally, the outlet losses can be determined with Equation (6.10).

$$K_o = \left[\left(2.93291\left(\frac{L_w}{L_b}\right)^2 - 2.89188\left(\frac{L_w}{L_b}\right)\right)\left(\frac{L_s}{L_t}\right)^3 + 1.9874 - 3.02783\left(\frac{d_s}{2L_t}\right) + 2.0187\left(\frac{d_s}{2L_t}\right)^2\right]\left(\frac{L_b}{L_s}\right) \quad (6.10)$$

It can be seen from the above equations the resistance of the heat exchanger is dependent on configuration and the flow field it experiences. The dimensions of the geometry were therefore held constant, and the flow dependent variables were altered. The values that can be readily altered are a and b used in the K_{HE} equation (Equation 6.3. These variables, a and b, change the resistance caused by flow through the heat exchanger. This is the largest of the resistances, and will therefore have the largest effect.

6.3 Operating point calculations

In order to determine the systems operating point it is necessary to solve Equation (6.1) by substituting the fan static pressure equation for the total pressure loss. The substitution is done because all of the energy lost by the heat exchanger must be supplied by the fan. The velocity of the air passing the fan must however be converted to the velocity of the air passing through the heat exchanger, since the resistance is applied to air flowing passed through the heat exchanger.

To do the substitution the fan static pressure equation is needed. This is derived by determining the fan static pressure change with respect to volume flow rate. This was done by plotting the fan static pressure versus the volume flow rate, and obtaining the equation of the resulting curve. Due to the possibility of the full scale model not being stable at low flow rates, the $d_{FC} = 1.542m$ B-fan, with a blade root stagger angle of $\gamma_{root} = 59°$ was used to calculate the operating point. The relationship can be expressed

as:

$$\Delta p_{FS} = -1.7697 v_{fan}^2 + 31.859 v_{fan} + 159.07 \tag{6.11}$$

Since the volume flow rate through the fan is the volume flow rate through the heat exchanger, to satisfy continuity. This can then be converted to the fan static pressure change with respect to the air velocity through the heat exchanger. Thus Equation (6.11) becomes:

$$\Delta p_{FS} = -82.966 v_{HE}^2 + 218.04 v_{HE} + 159.22 \tag{6.12}$$

Equation (6.12) can now be substituted in to Equation (6.1), which produces:

$$-82.966 v_{HE}^2 + 218.04 v_{HE} + 159.22 = K_{\theta t} \cdot \frac{1}{2} \rho v_{HE}^2 \tag{6.13}$$

The velocity used in Equation (6.13) coincides with the flow rate deemed to be sufficient for the current purposes. Since the investigation is isothermal, the main requirement is that the flow rate be higher then that of maximum fan static efficiency. The flow rate chosen was $V = 16.5 m^3/s$, which corresponds to $v_{HE} = 2.41076 m/s$. The values of a and b in Equation (6.3) are now adjusted to obtain the resistance that correlates to the chosen flow rate. In order to ensure realistic results the initial values specified were taken from literature [6, 35] and adjusted slightly until they satisfied Equation (6.13). The values $a = 4177.085$ and $b = -0.365$ were found to produce a sufficient resistance to satisfy Equation (6.13).

6.4 Resistance calculations

Once the heat exchanger performance characteristics were determined, they were converted to a set of values that FLUENT® can use to reproduce these characteristics. When a region had been specified as being a porous region, FLUENT® applied a source term to the momentum equation in this region [14]. The source term for a simple homogeneous porous region is described by Equation (6.14).

$$S_i = -\left(\frac{\mu}{\alpha} v_i + C_2 \frac{1}{2} \rho v_{mag} v_i\right) \tag{6.14}$$

Where $\frac{1}{\alpha}$ is the viscous resistance and C_2 is the inertial resistance. The momentum equation can be simplified to relate the source term to a pressure drop, or

$$\nabla p = S_i \tag{6.15}$$

Which can be rewritten as

$$\Delta p = -S_i \Delta n \tag{6.16}$$

Where Δn is the thickness of the porous region. For these calculations the actual thickness of the heat exchanger to be modeled is used. Refer to Figure (7.1) in Chapter 7 for these dimensions.

Figure 6.3: Heat exchanger performance curve

The the performance characteristics of the heat exchanger needs to be written in a form such that the resistance is specified as a pressure loss that is proportional to the velocity. This is done by calculating the pressure drop across the heat exchanger, using the constants previously calculated, for various flow rates. The curve produced can be seen in Figure (6.3). This is the curve that FLUENT® will be required to recreate. The equation of this curve was found to be:

$$\Delta p = 18.944 v^2 + 30.613 v \tag{6.17}$$

Comparing Equation (6.16) and Equation (6.17) it follows that:

$$C_2 = \frac{18.944}{\frac{1}{2}\rho \Delta n} \tag{6.18}$$

$$\frac{1}{\alpha} = \frac{30.613}{\mu \Delta n} \tag{6.19}$$

Substituting in the model constants of $\mu = 1.7894 \times 10^{-5}$, $\rho = 1.225 kg/m^3$ and $\Delta n = 0.037m$ produces the desired constants. The values used are as follows:

$$C_2 = 835.913 \tag{6.20}$$

$$\frac{1}{\alpha} = 46237750 \tag{6.21}$$

The values of C_2 and $\frac{1}{\alpha}$ must be specified to act perpendicular to the plane of the heat exchanger. To restrict the flow in the plane of the heat exchanger the value of C_2 in the plane of the heat exchanger was made to be 100000. This is more then 1000 times larger than the value of C_2 perpendicular to the plane of the heat exchanger.

6.5 Heat Exchanger validation

The values of C_2 and $\frac{1}{\alpha}$ needed to be tested to ensure they produce the correct trends. This was done by creating a test section with a heat exchanger in it, and compare the performance curves to those of the empirically derived heat exchangers. The test section can be seen in Figure (6.4). Inspecting Equation (6.16) the only dimension of interest is the thickness of the heat exchanger in the flow direction. This is the reason that the porous region is made $\Delta n = 0.037m$ thick, which is the thickness of the heat exchanger to be used in the ACHE. The length and breadth of the heat exchanger are equal in length and are arbitrarily chosen.

To reproduce the curve in Figure (6.3), it was necessary to vary the flow rate through the heat exchanger and plot the static pressure drop versus volume flow rate. The results of this can be seen in Figure (6.5).

The correlation of the numerical and the empirical data is very good. It was therefore concluded that the pressure drop across the heat exchangers is reproduced appropriately. Heat exchangers, however are usually characterized by plotting the heat exchanger loss co-efficient, K_{HE} versus the characteristic flow parameter, R_y [6, 35]. The graph shown in Figure (6.5) is converted to comply with this convention. The discrepancy shown in Figure (6.5) and (6.6) is due to having to adjust the curve in Figure (6.4) such that it intersects the axes at (0,0). The adjustment is legitimate as when there is no air flow there can be no resistance. Equation (6.14) also requires that the curve intersects at (0,0) to be solved.

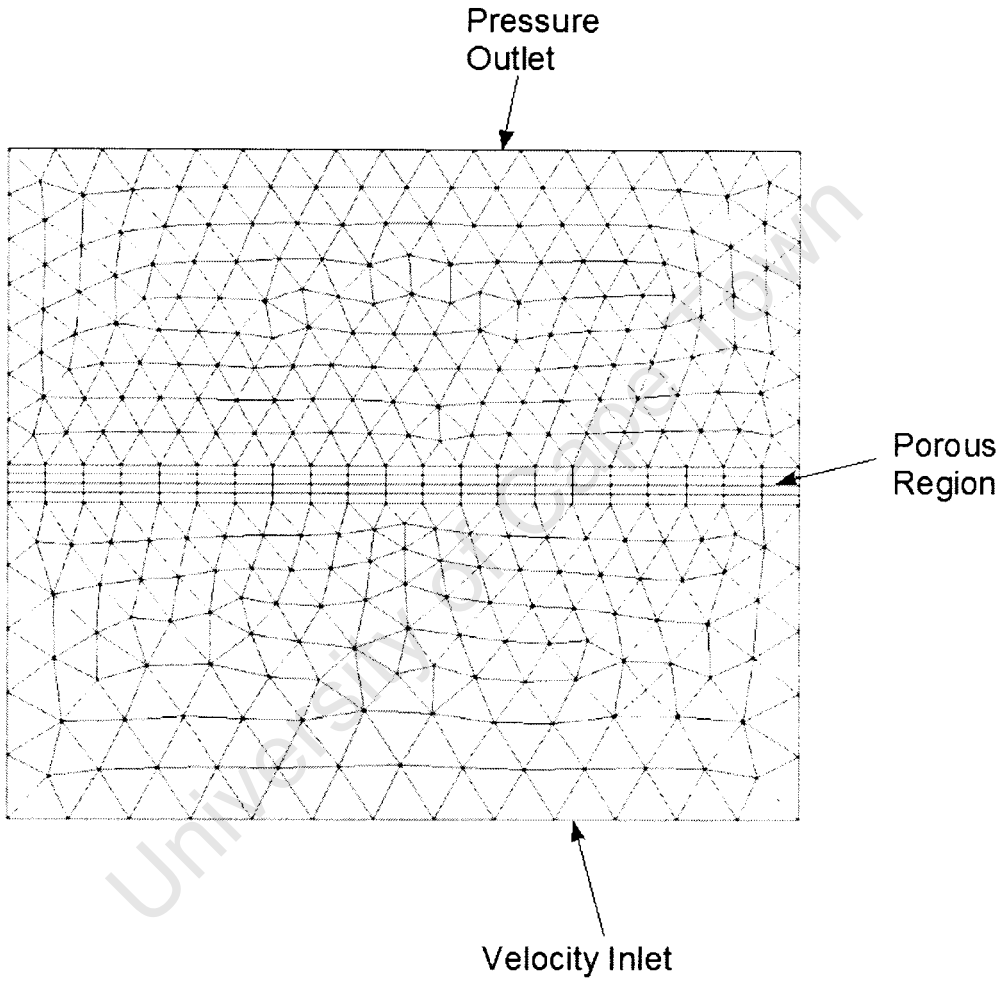

Figure 6.4: Side view of the geometry used to validate the heat exchanger

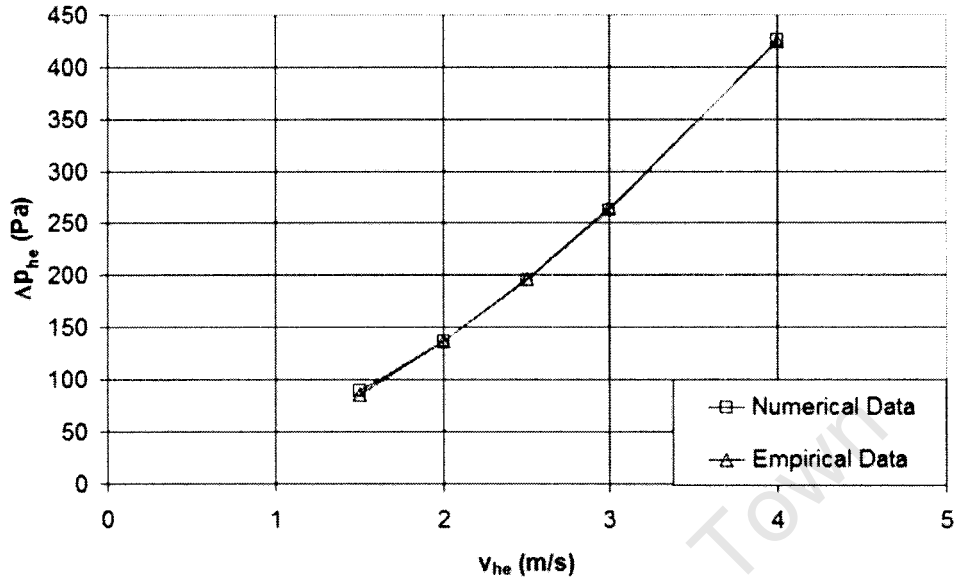

Figure 6.5: Comparison of the numerical and the empirical pressure loss

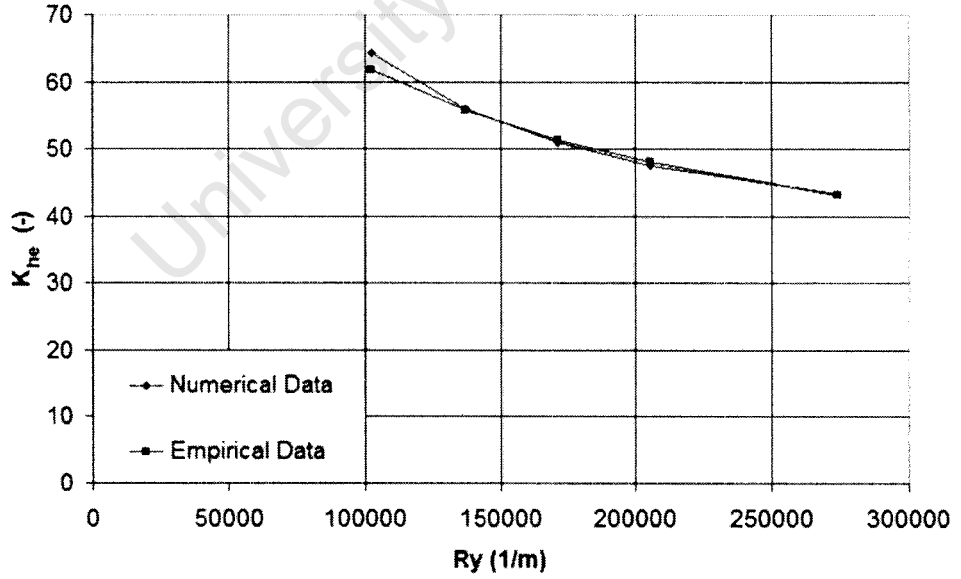

Figure 6.6: Comparison of the numerical and the empirical heat exchanger performance curves

Chapter 7

ACHE validation

The fan model and the heat exchangers have been developed and validated and have shown that they produce realistic results. The amalgamation of these components needs to be tested to ensure that they produce realistic results. This is done by constructing a delta plenum air-cooled heat exchanger and investigating it's performance under ideal inlet conditions. According to Duvenhage *et al.* [9], a bell-mouth inlet shroud produces the least inlet loss when compared to cylindrical and conical inlet shrouds. The ACHE will be considered to operate appropriately if the numerical volumetric flow rate through the fan matches the analytically calculated operating point volume flow rate.

7.1 Geometry and Boundary Conditions

The geometry of the ACHE to be modeled is a scaled down version of the geometry used by Dunn [27]. The unscaled geometry had a fan diameter of $10m$, and the heat exchangers were 12m x 12m x 0.24m. As mentioned before, with the constraint on the number of cells the large geometry would not converge. The geometry was scaled down such that the fan would have a fan diameter of $d_{fc} = 1.542m$, to correlate to the validated fans. The scaled down dimensions can be seen in Figure (7.1). The dimensions used are generic, and based on suggestions in literature [6].

Salta and Kröger [7] stated that the ideal volume flow rate through an ACHE occurs in the absence of inlet disturbances. The geometry created thus has a cylindrical "atmospheric" region which contains no obstructions. To simulate the atmospheric region, the boundaries were set as being pressure inlets, as can be seen in Figure (7.2). The geometry upstream of the fan is constructed according to the conditions used to

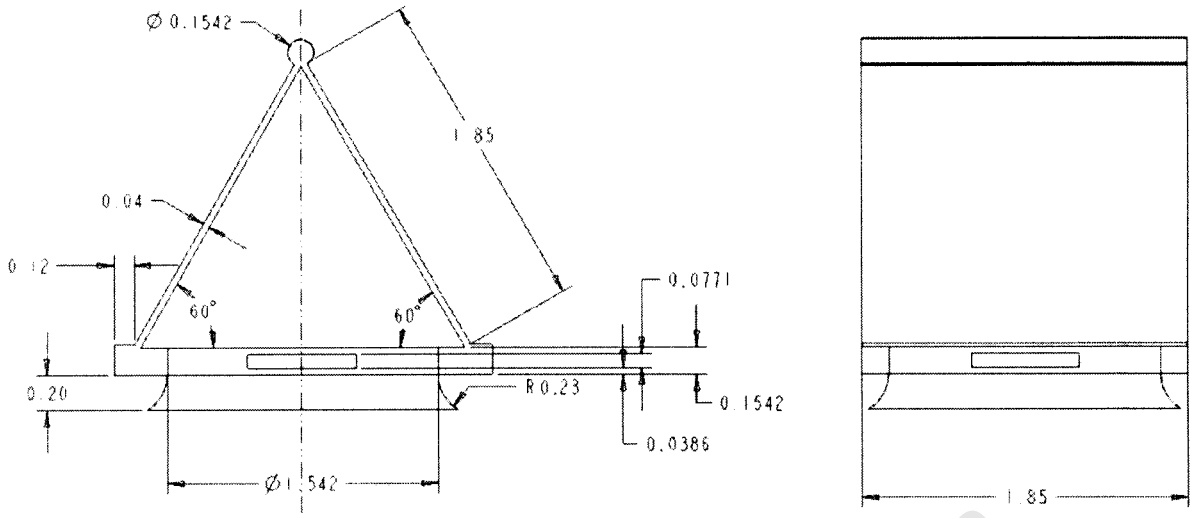

Figure 7.1: Dimensions of the ACHE to be modeled

calculate the operating point in Chapter 6. This means that the heat exchanger must be at 60° to the plane of fan rotation, the steam duct must be present, and the dimensions as those that are used to calculate the resistance curves. The geometry to be investigated can be seen in Figure (7.2).

During the operating point calculations in Chapter 6 the effect of adjacent heat exchangers was taken into account. Therefore the effect of adjacent ACHE's must be considered. This is achieved by specifying the walls on the perimeter of the ACHE, upstream of the fan, to be symmetry planes. Symmetry planes act similar to walls but reflect the influence of the flow, back on itself, without imposing wall functions [14]. The symmetry plains thus have the same effect as adjacent ACHE's would have, if they were modeled.

The heat exchangers are specified as being porous media, with the coefficients specified such that the flow can only exit the heat exchanger perpendicular to the plane of the heat exchanger. The coefficients calculated in Chapter 6 were used to specify the resistance characteristics. The plane of the heat exchanger had to be determined however, in order to specify the direction of flow. This was done by creating a surface that is flush with one of the surfaces of the heat exchanger, and then retrieving from FLUENT® the normal to that surface, as well as a vector in the plane of the heat exchanger.

For the fan model, three discs were created, as in Chapter 3 and 4. The characteristics used are as follows:

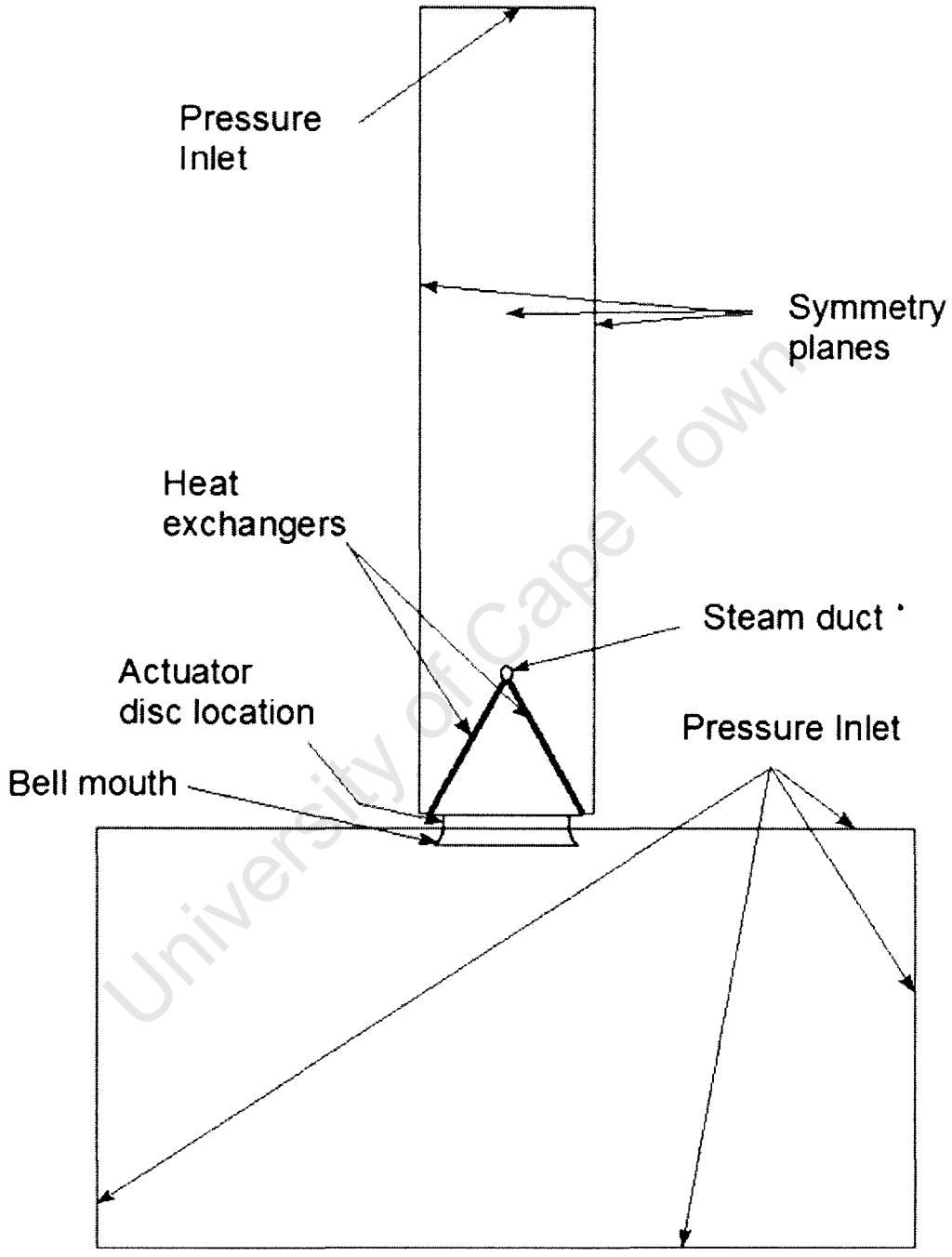

Figure 7.2: Geometry used to investigate ideal inlet conditions

Fan casing diameter	$d_{FC} = 1.542m$
Hub diameter	$d_{FH} = 0.616m$
Tip clearance	$4mm$
Rotational speed	$N = 750RPM$
Blade root stagger angle	$\gamma_{root} = 59°$

Table 7.1: Fan characteristics used for the ideal volume flow rate simulations

The simulations will be performed using the standard $k - \epsilon$ turbulence model, using the default coefficients. The SIMPLEC pressure velocity coupling algorithm will be used instead of the default SIMPLE algorithm. The under relaxation factors are set as follows:

	Default	Used
Pressure	0.3	0.2
Density	1	1
Body Forces	1	1
Momentum	0.7	0.5
Turbulence Kinetic Energy	0.8	0.8
Turbulence Dissipation Rate	0.8	0.8
Turbulent Viscosity	1	1

Table 7.2: Under-relaxation factors used for this investigation

These under-relaxation factors will be used for all further simulations. All the simulations are done in single precision, which is not as accurate as double precision. Therefore the first order upwind discretization scheme was used. The first order upwind discretization scheme is only first order accurate. The standard discretization scheme is used for the discretization of pressure.

7.2 Results and Discussion

In Chapter 6 the ideal volume flow rate through an ACHE was calculated. This was done by including only the resistances downstream of the fan. In this section the geometry was created that has only downstream resistances. The ideal volume flow rate through

the system can now be calculated. Volume flow rate is defined as

$$V = \bar{v} \cdot A \tag{7.1}$$

Where $\bar{v}$ is the average velocity, and A is the cross sectional area, perpendicular to the average velocity vector. Thus to calculate the volume flow rate the area weighted average velocity, perpendicular to the fan, was calculated. The surface over which the calculations are performed was the upstream surface of the downstream, or outlet disc. By using this surface, consistency in the measurements is ensured, as this face never moves with relation to the other discs or the fan.

The volume flow rate was found to be $V = 16.635m^3/s$. The calculated volume flow rate was $V = 16.5m^3/s$, making the difference 0.8%. It can therefore be concluded that the numerical model can be used to evaluate ACHE's, because the error is negligable.

A large scale ACHE was simulated in order to investigate whether meaningful results could be produced, and test whether the problems at low flow rates experienced during the fan validation would be problematic. To ensure that the inertial and viscous coefficients were appropriate, the coefficient calculated by Dunn [27] were used. It was found that for the large scale ACHE's the turbulent viscosity was limited in a large majority of cells.

Chapter 8

Effect of ground clearance on a single row of ACHE's

Now that the ACHE model has been shown to produce meaningful results, it can be used to investigate the effects of ground clearance on a row of ACHE's. All the fans draw in air from the same location, the area between the symmetry planes on the side view in Figure 8.1. As the fan platform height is reduced this area is reduced, which induces cross flow on the fans closest to the perimeter of the bank. It has been shown that these cross-flows reduce the volumetric effectiveness of the fans [6, 7, 8, 9, 11], and thus the cooling capacity of the ACHE.

8.1 Geometry and Boundary Conditions

The geometry used will be a row of the ACHE's identical to those in Chapter 7. Figure 8.1 shows how the ACHE bank is constructed and the location of the symmetry planes. The symmetry planes are positioned such that they are the planes that experience no through flow. To create the ACHE bank, the fan-heat exchanger units will be connected end to end, as shown in Figure (8.2). The volumes below the fan are removed individually until the required platform height is attained. The volumes above the ACHE are used to break up the domain, in order to better control the mesh. The symmetry boundaries on the sides and the rear of the ACHE row are used to account for the effect of the adjacent rows. This also means that the ACHE simulated only has to be half the length of the ACHE bank required. The heat exchangers and the actuator discs are set up as mentioned before. The fan model constants, and the solver constants specified in Chapter 7 are used.

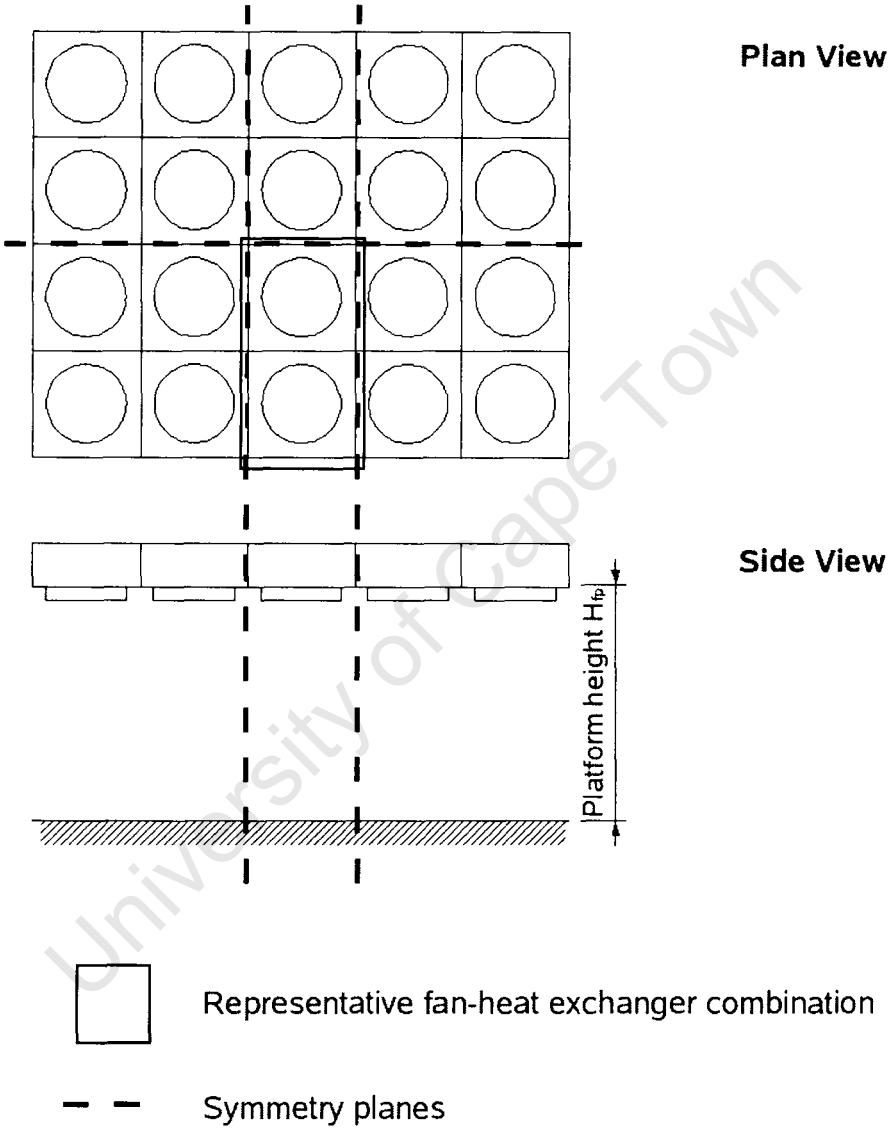

Figure 8.1: Schematic of the 2 fan ACHE bank, showing symmetry plane locations

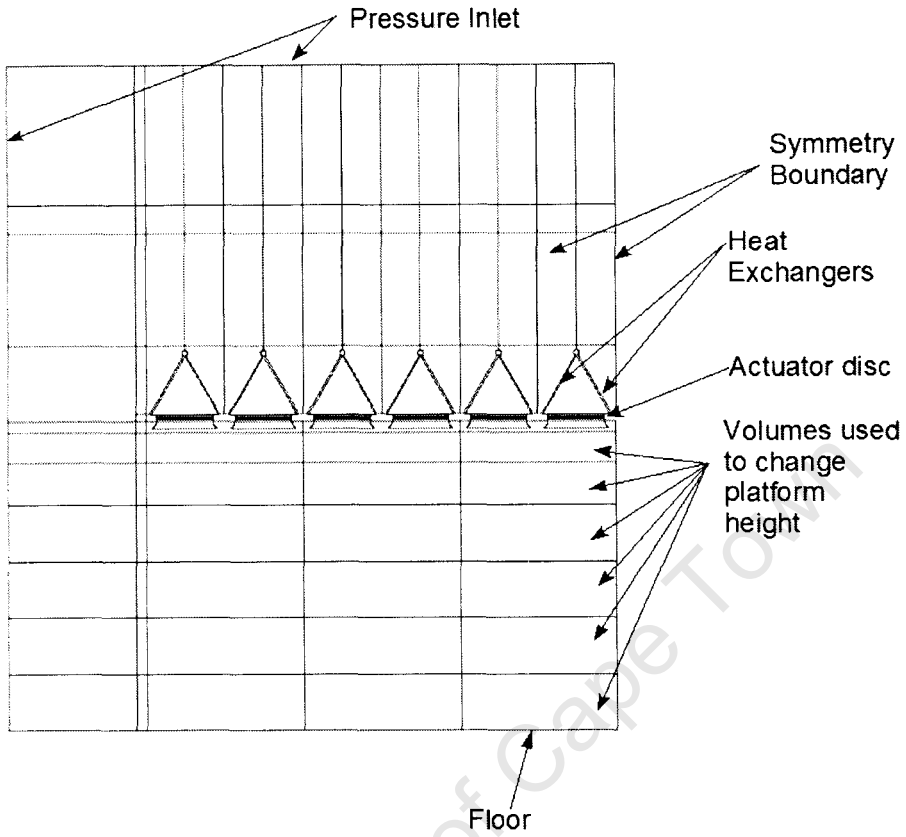

Figure 8.2: Schematic of the geometry to be modeled, showing boundary conditions

The following scenario's will be simulated: 1, 2, 4, 6, 8, and 12 ACHE's in a row, using the following platform heights $\frac{H_{FP}}{d_{FC}} = 5.5, 4.5, 3.5, 2.5, 1.5, 0.75$, where H_{FP} is the platform height above ground, and d_{FC} is the fan casing diameter. For a single ACHE, there will be only 2 symmetry planes and the ACHE will be open to the atmosphere on opposite sides, the left and the right of Figure (8.2). The numbering convention for all multiple fan systems to be tested from here on is as follows:

- Fan 1 is the fan that is situated at the origin, $(0, 0, 0)$ and is the peripheral fan, and thus closest to the ACHE bank periphery.
- Fan 2 - fan N is the next fan in the direction of the ACHE row, where N is the number of fans in the system.
- For an N x M array of fans that make up the ACHE bank, Fan 2 is the next fan in the negative Y direction. When the end of the current column is reached, i.e., fan N, the next consecutive fan number $N + 1$ starts in the next column in the

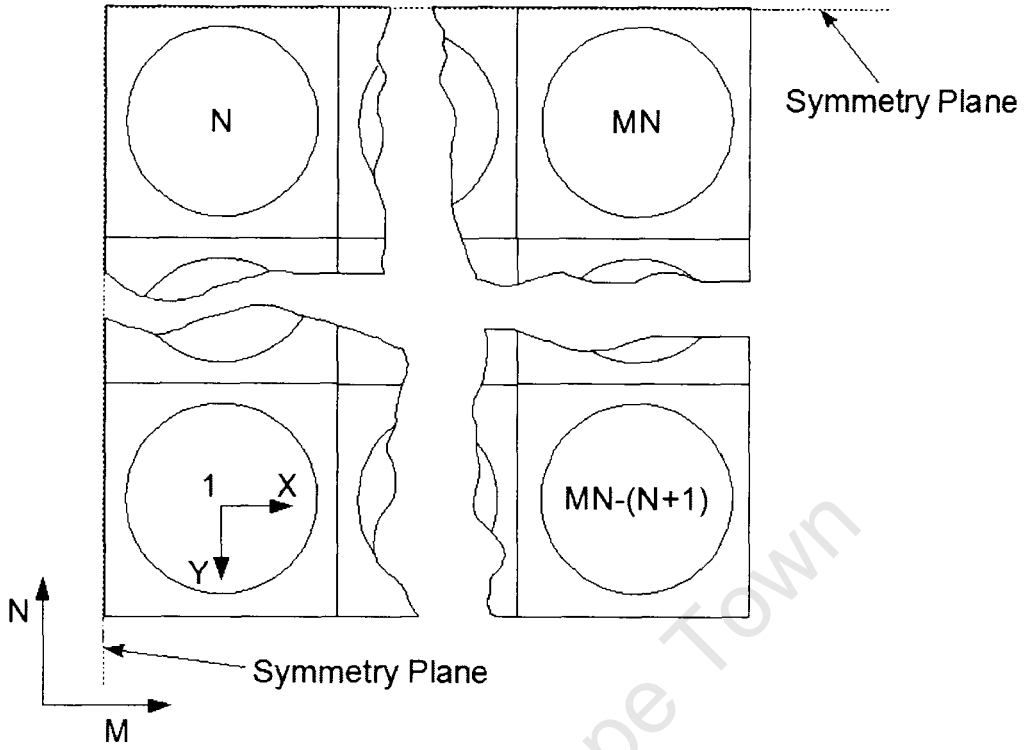

Figure 8.3: Fan numbering scheme used

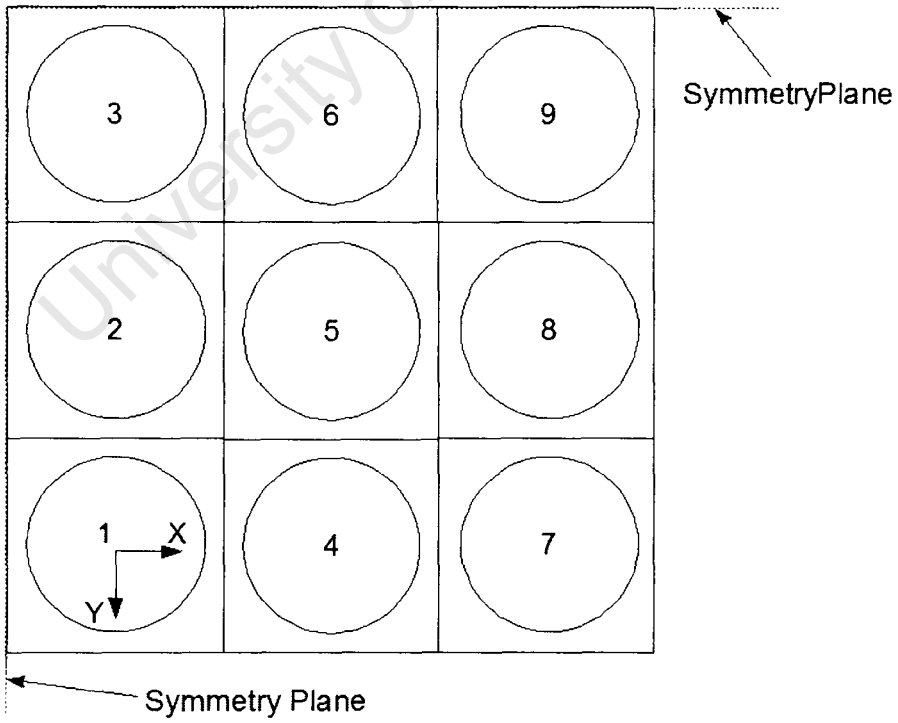

Figure 8.4: Example of the numbering used for a 3X3 fan system

positive X direction in line with fan 1, as shown in Figure 8.3. An example of a 3 x 3 fan system is given in Figure 8.4.

8.2 Results and Discussion

Salta and Kröger [7] experimentally investigated the effect of ground clearance on the volumetric effectiveness of a fan. The volumetric effectiveness of a fan is the ratio of the volume flow rate of air drawn through the fan, compared to the ideal volume flow rate for the same fan. Salta and Kröger [7] presented the volumetric effectiveness as a function of the dimensionless platform height X, such that :

$$\frac{V}{V_{id}} = 0.985 - e^{(-X)} \tag{8.1}$$

Where for fan system with 2 or more fans

$$X = \frac{(1 + \frac{45}{n_f})H_{FP}}{6.35 d_{fc}} \tag{8.2}$$

or

$$X = 4.882 \frac{H_{FP}}{d_{FC}} \tag{8.3}$$

For a single fan system.

In Equation 8.2 and 8.3, H_{FP} is the fan platform height, d_{FC} is the diameter of the fan, and n_f is the number of fans. Use of the symmetry plane means that n_f will be twice the number modeled, except in the single ACHE case. For the multiple fan ACHE configurations, the system average volume flow rate is used to calculate the volumetric effectiveness. Meyer [11] did numerical investigations of Salta and Kröger's [7] experiments and found a good correlation between the numerical and experimental results.

It should be noted that in Figure (8.5) to (8.10) "Empirical" refers to the values obtained using Equation 8.1 and 8.2 or 8.3, depending on the number of ACHE's. The numerical plot is the one obtained in the current investigation.

In general the correlation is good, with the trends repeatedly reproduced. This shows that the numerical model does produce reasonable results, and can be used to investigate proposed techniques to improve the effectiveness of the system. The discrepancy is thought to be system related, as Salta and Kröger [7] used a test facility comprised of

a set of fans and Meyer [11] used a porous region downstream of the fan. Neither of these investigations utilized a delta plenum chamber, with upstream effects taken into account.

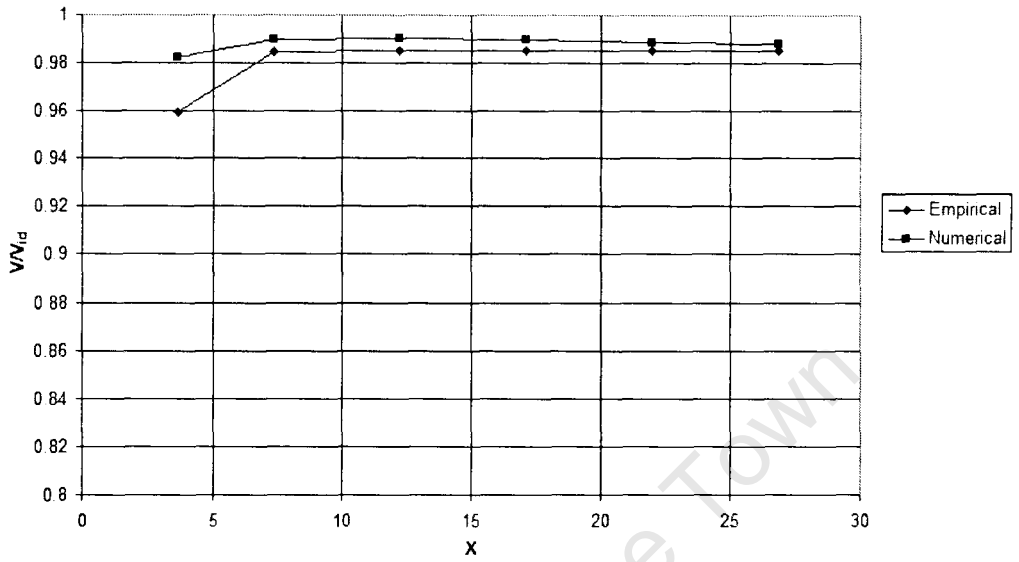

Figure 8.5: The volumetric effectiveness of a 1 ACHE system

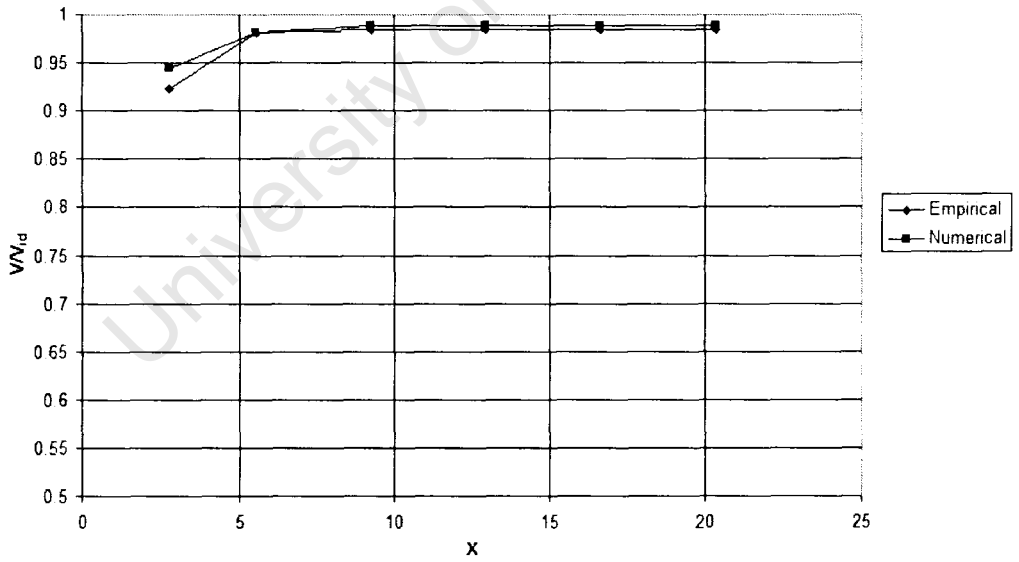

Figure 8.6: The volumetric effectiveness of a 2 ACHE system

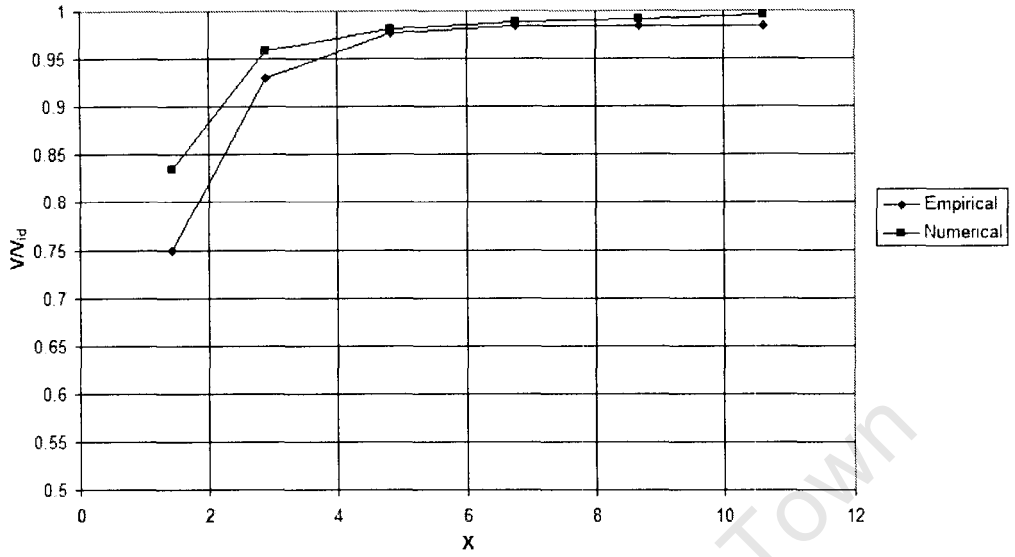

Figure 8.7: The volumetric effectiveness of a 4 ACHE system

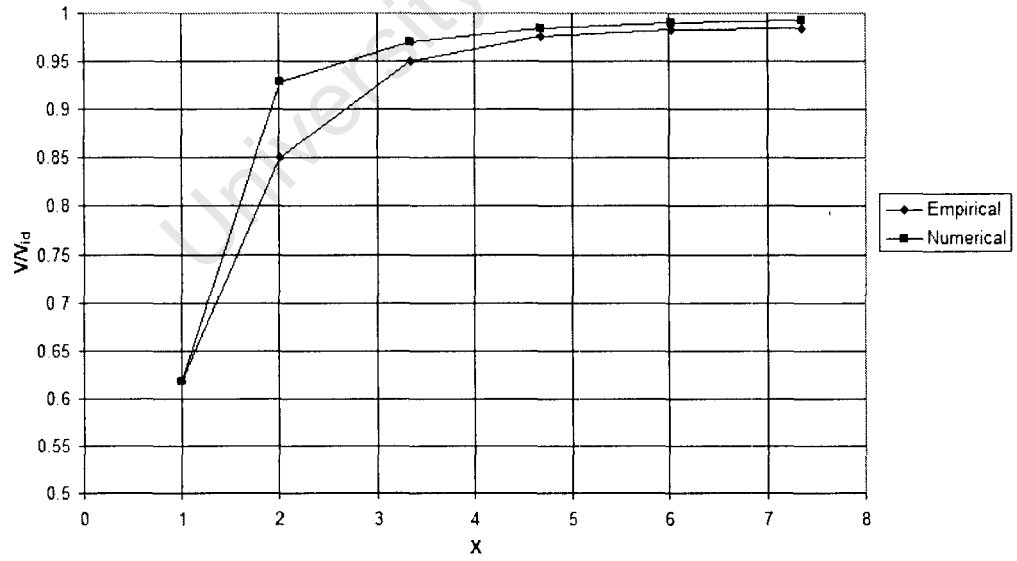

Figure 8.8: The volumetric effectiveness of a 6 ACHE system

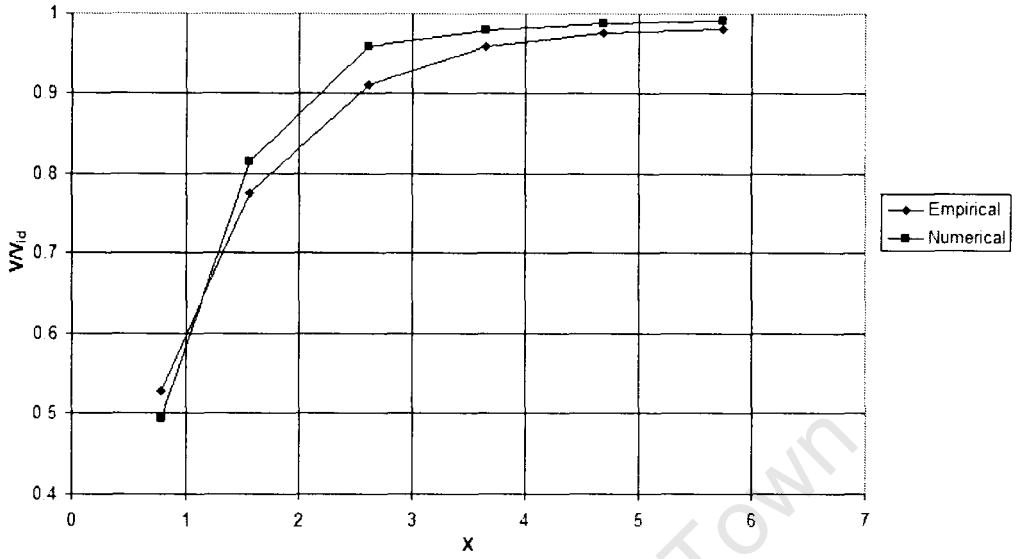

Figure 8.9: The volumetric effectiveness of a 8 ACHE system

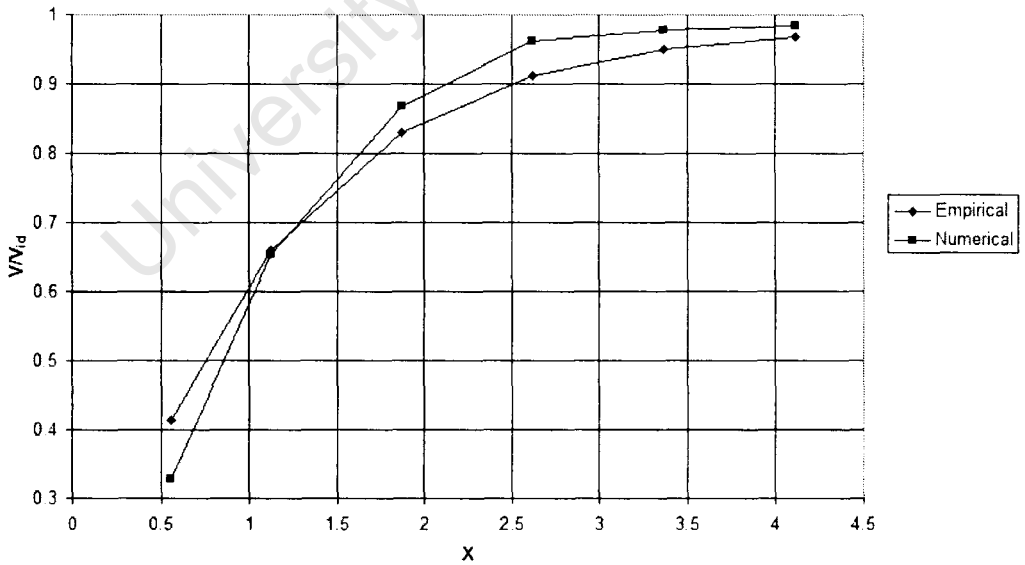

Figure 8.10: The volumetric effectiveness of a 12 ACHE system

Chapter 9

Effect of a walkway on the volumetric effectiveness

Previous experimental and numerical investigations suggest that the addition of a walkway on the perimeter of the fan platform increases the volumetric effectiveness of the periphery fans [7, 11]. The experiments carried out by Salta and Kröger [7], and the numerical simulations carried out by Meyer [11] investigated the effect of a walkway were done using only two fans, or a four fan system when symmetry is considered. In the numerical investigation Meyer [11] investigated the effect of one size walkway. The 12 fan system, and 8 fan system configurations investigated in Chapter 8 will be investigated as well, thus investigating if the current trends are applicable for larger ACHE's.

9.1 Geometry and Boundary Conditions

To simulate the effect of a walkway, an infinitely thin wall is attached to the fan platform, as shown in Figure 9.1. The width is measured from the side of the platform to the edge, the length is the same as the length of the ACHE, $1.85m$. For the simulations in this section the boundary conditions will be set up identically to those in Chapter 8. The only difference is the addition of a walkway of varying width. The widths to be investigated are the same as those used in the investigation by Salta and Kröger [7], and are listed in Table 9.1. The ratio $\frac{W_w}{d_{FC}}$ is the ratio of the walkway width to the fan diameter.

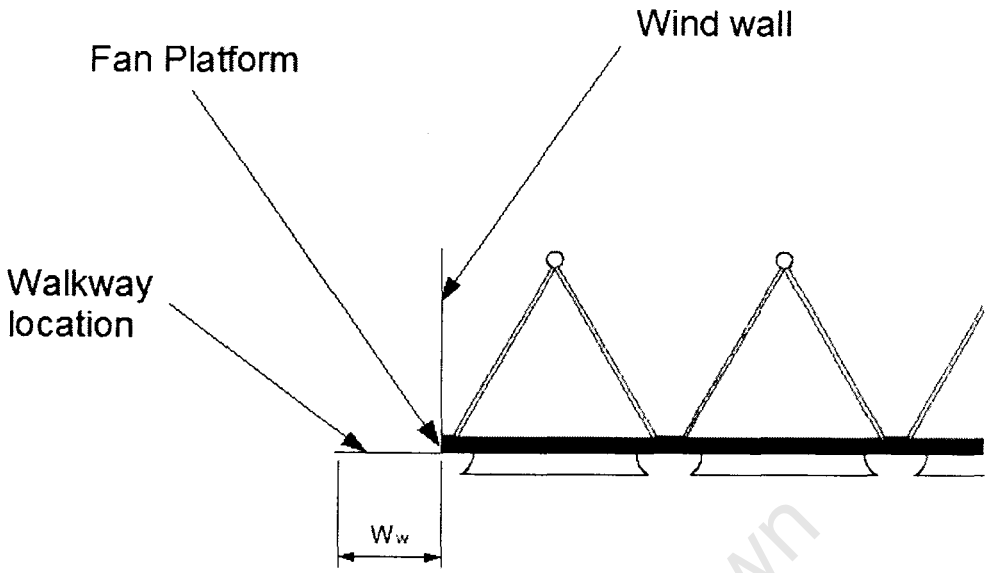

Figure 9.1: ACHE schematic showing the location of the walkway

$\frac{W_w}{d_{FC}}$	W_w
-	m
0	0
0.159	0.245178
0.317	0.488814
0.476	0.733992
0.635	0.97917

Table 9.1: Walkway widths to be investigated

9.2 Results and Discussion

Meyer [11] found that the inlet loss of the first fan was predominantly due to separation losses in the bell mouth. By adding a walkway the region of separation is moved to the region between the bell mouth and the walkway. Since the aim of the walkway is to improve the volumetric effectiveness of the system, the results in this section will be compared to the results of the ACHE's that do not have a walkway. The results from the Chapter 8 will be used as the basis for comparison. Unlike in Chapter 8, the volumetric effectiveness is not averaged over all the fans. Instead the volumetric effectiveness of the first and second fans are shown. If the system volumetric effectiveness is used, it is difficult to visualize the difference, as the largest improvement occur at the peripheral fans. The peripheral fans are also the ones of interest, in this investigation.

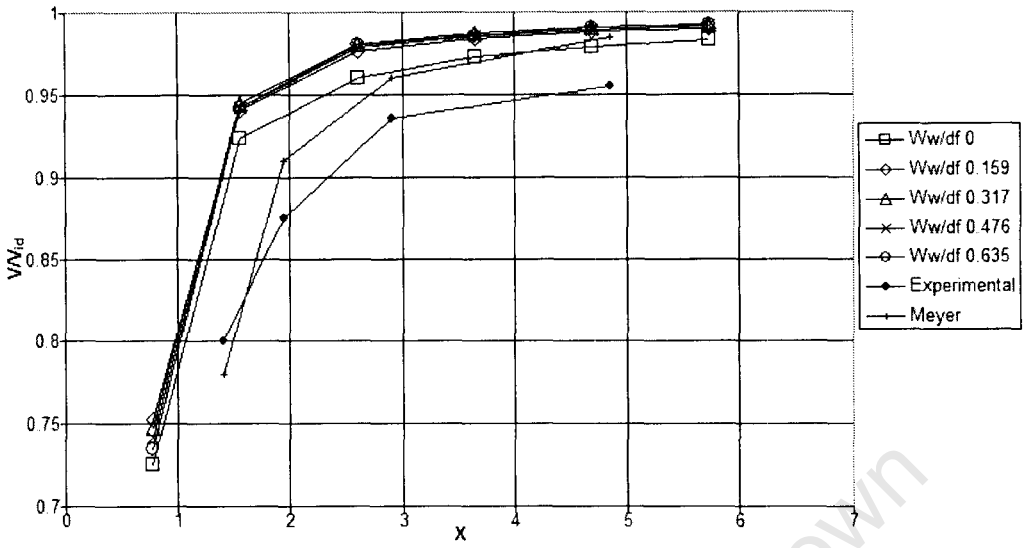

Figure 9.2: Effect of a walkway on the first fan of a 4 fan system

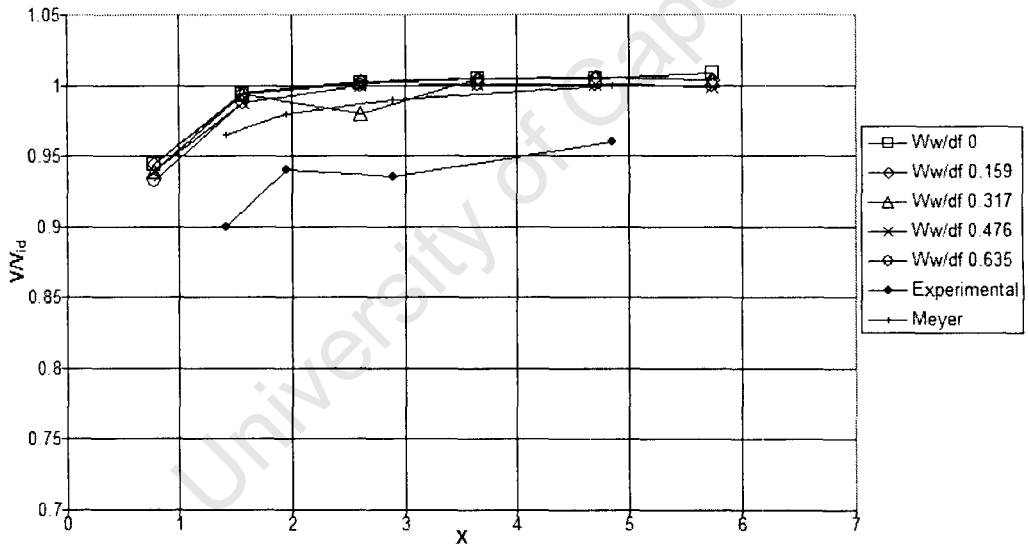

Figure 9.3: Effect of a walkway on the second fan of a 4 fan system

When referring to Figure 9.2 and Figure 9.3 it can be seen that the addition of the walkway does improve the volumetric effectiveness of the individual fans. The effect of adding a wider walkway adds only a marginal increase in performance, and at $\frac{W_w}{d_{FC}} = 0.317$ it reaches a maximum, as shown in Figure 9.4. This is consistent with the experimental data taken from Salta and Kröger [7]. For the 4 fan system the experimental results are taken from Salta and Kröger [7].

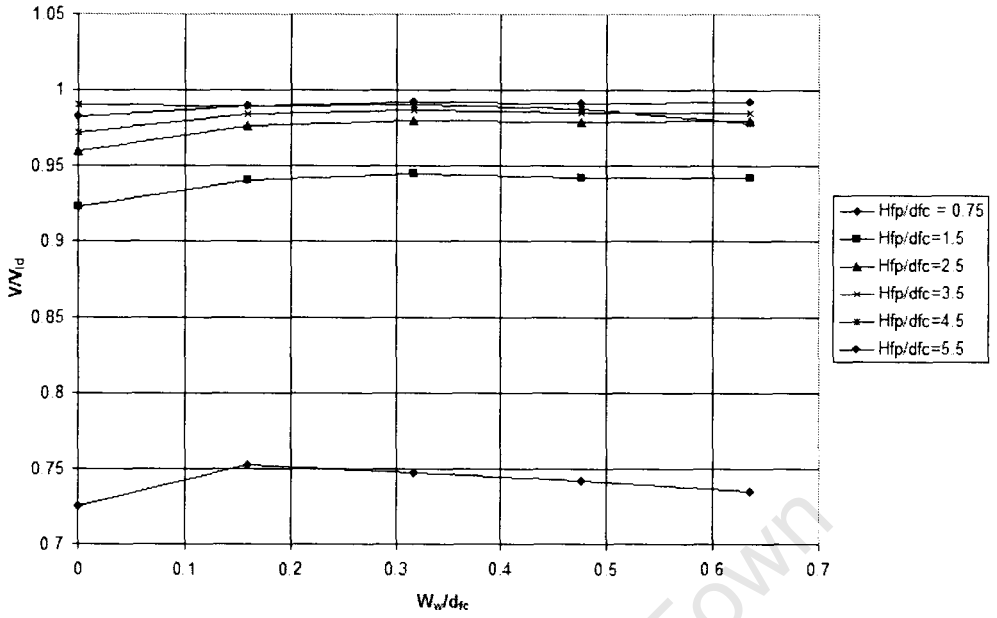

Figure 9.4: The volumetric effectiveness of a 4 fan system as a function of the walkway width

The difference between the numerical results in this investigation, those of Meyer [11] and the experimental work done by Salta and Kröger [7] might be caused by a coarse mesh. To investigate this a finer mesh was generated, such that the number of cells in the region of the bell mouth doubled. This is referred to as FINE in Figures (9.5) and (9.6). The mesh inside the bell mouth, and in the surrounding area was then again increased, such that the mesh density inside the bell mouth increased by a factor of three and in the surrounding region there were twice as many cells. This is referred to as FINER in Figures (9.5) and (9.6). It can be seen from Figures (9.5) and (9.6) that the difference is results is not tied to the grid density. It is thought that the discrepancy could be due to system effects, as in previous investigations the plenum, and the atmosphere above it were not modeled.

It can be seen that the effect of the walkway is recreated using the model. The values are slightly different, but the trend is reproduced. To this end the results for the 8 fan and the 12 fan system should be meaningful. Figures (9.7) and (9.8) show the effect of the walkway on an 8 fan system. It is clear that the effect of the walkway is more pronounced on the first fan then on the second fan. The largest change occurs for fan platform heights that are not recommended for commercial use, therefore the ad-

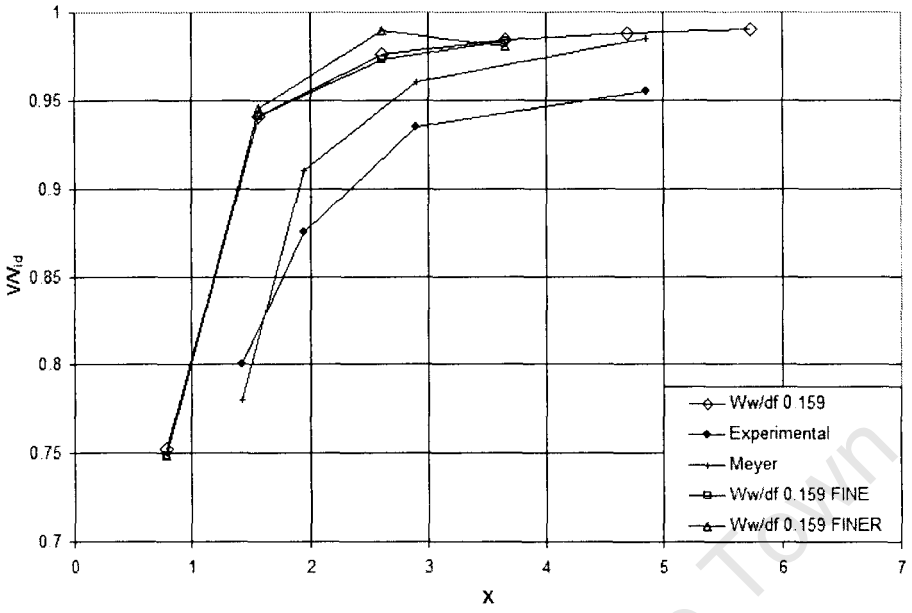

Figure 9.5: Effect of grid density on the first fan of a 4 fan system

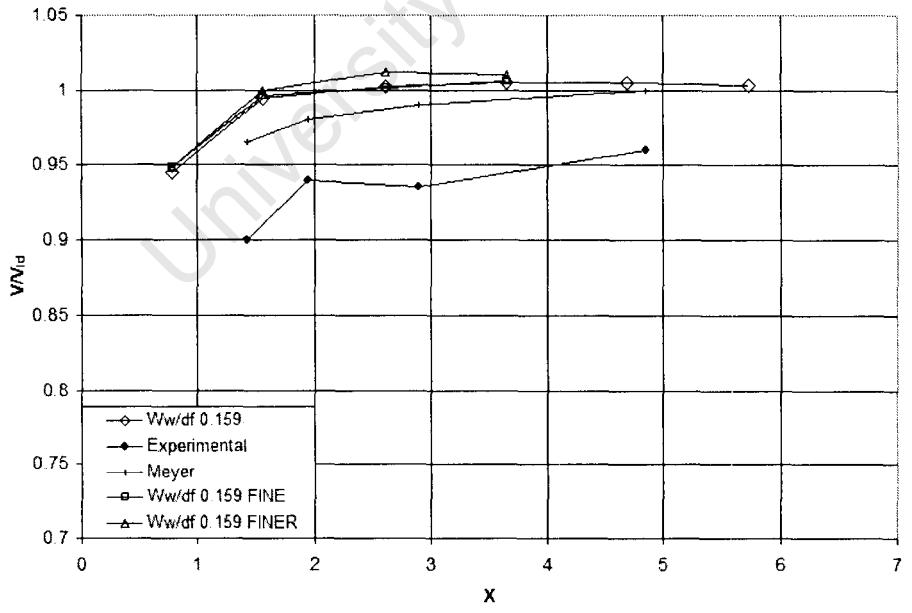

Figure 9.6: Effect of grid density on the second fan of a 4 fan system

dition of the walkway will only really improve the volumetric effectiveness of the first fan.

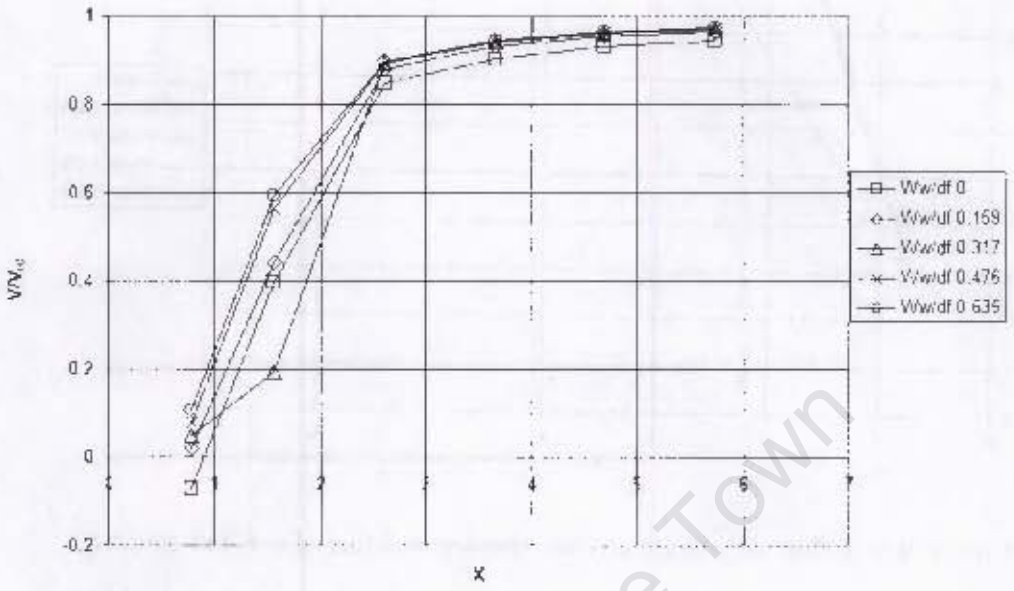

Figure 9.7: Effect of a walkway on the first fan of a 8 fan system

The low value for a 8 fan system with $\frac{W_w}{d_{FC}} = 0.317$, at $X = 1.565$ appears to be due to the region of recirculation shown in Figure 9.10. This recirculation can also be seen in Figure 9.9, which is at the lowest platform height to be tested, but not in Figure 9.11. The region of recirculation in Figure 9.10 has moved such that it no sits on the lip of the bell mouth, causing a region of lower pressure. The low pressure region draws air through the fan in the opposite direction, thus decreasing the volumetric effectiveness. Since this only occurred for an isolated case, it could be a phenomenon that is related to a specific correlation of the velocity of the air through the entrance of the ACHE bank, the walkway width and the bell mouth height. The investigation of this phenomenon is beyond the scope of this report.

For an ACHE bank consisting of 12 fans, the addition of a walkway has a greater effect on the volumetric effectiveness of the first fan, especially at lower platform heights. This can be seen in Figures (9.12) and (9.13). The improvement on the first fan of a 12 fan system due to a walkway is because of the increase volume flow rate through the entrance to the ACHE bank. The increase in flow rate through the entrance of the ACHE bank thus creates a large cross flow, and thus a larger separation region, but the walk way moves this separation region to outside of the first fans bell mouth.

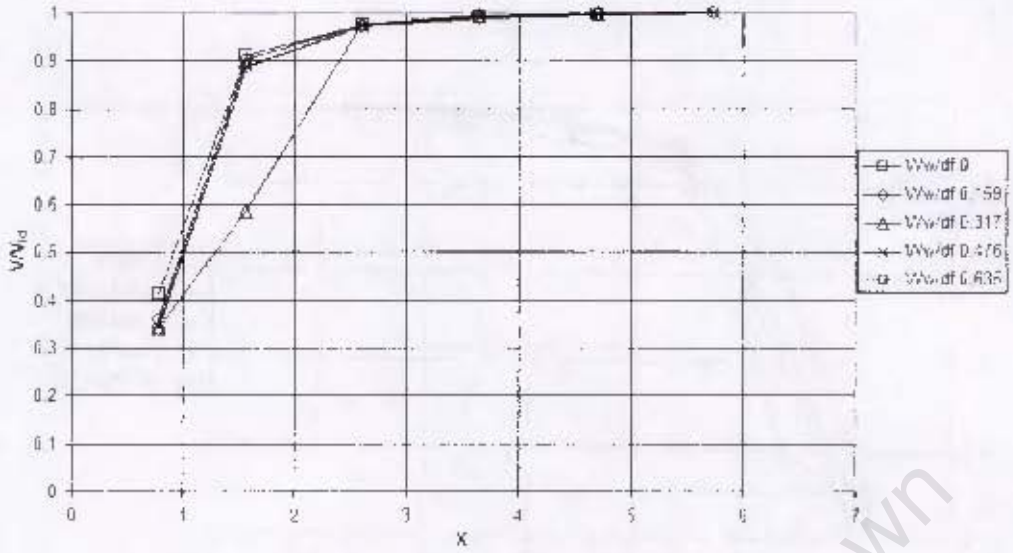

Figure 9.8: Effect of a walkway on the second fan of a 8 fan system

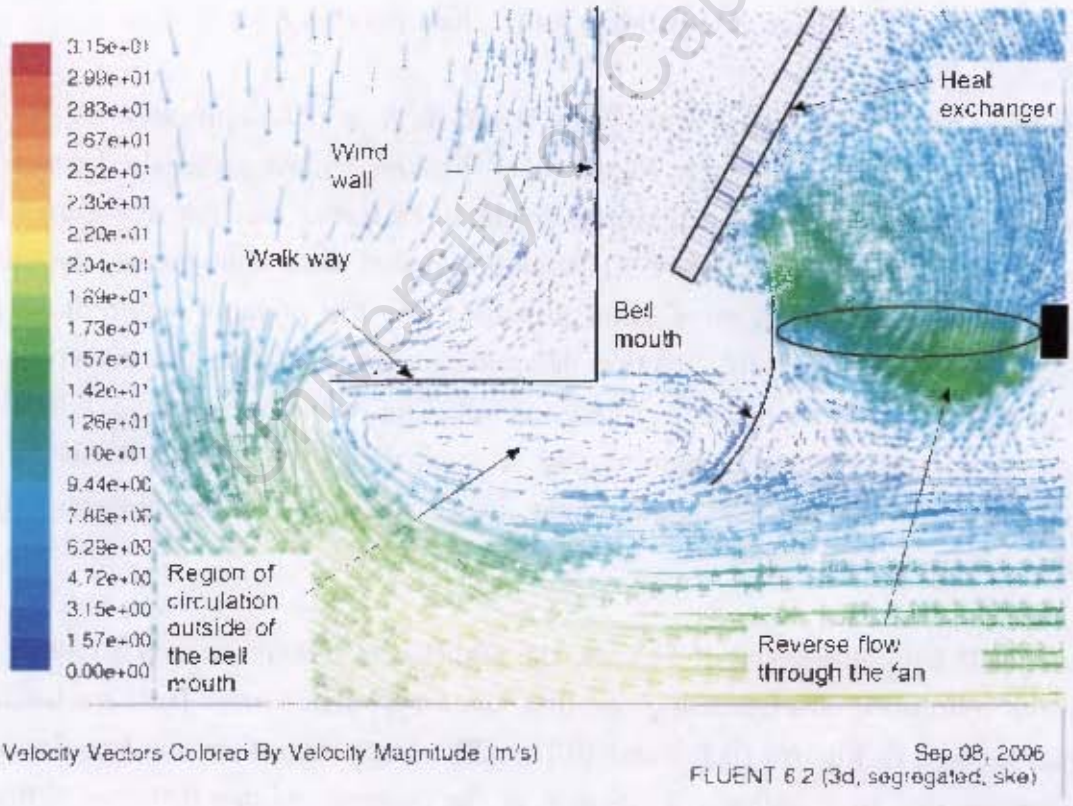

Figure 9.9: Velocity vector plot on vertical plane through fan 1, of a 8 fan system, with $\frac{W_w}{d_{fc}} = 0.317$ and $X = 0.782$

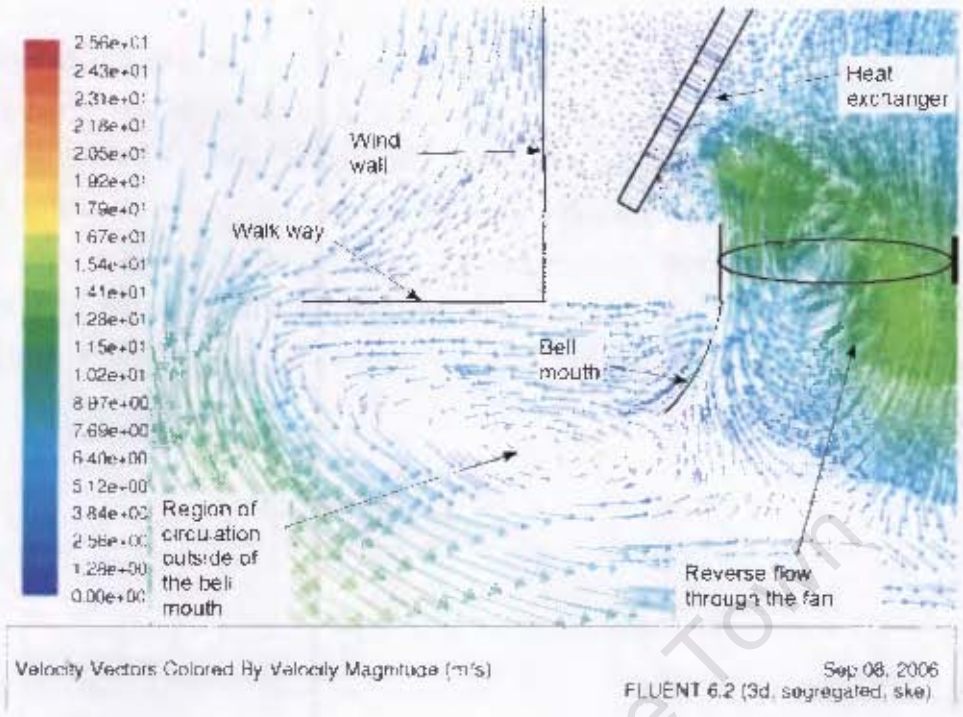

Figure 9.10: Velocity vector plot on vertical plane through fan 1, of a 8 fan system, with $\frac{W_w}{d_{FC}} = 0.317$ and $X = 1.565$

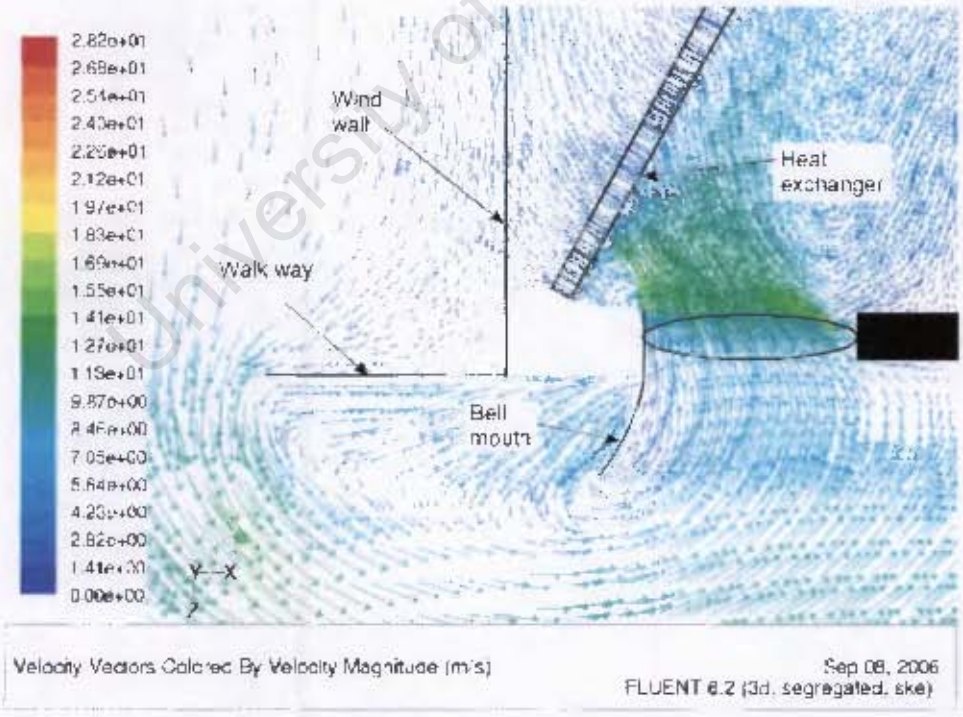

Figure 9.11: Velocity vector plot on vertical plane through fan 1, of a 8 fan system, with $\frac{W_w}{d_{FC}} = 0.317$ and $X = 2.608$

It is clear that having $X < 2.5$, or $\frac{H_{FP}}{d_{FC}} < 3.5$ is detrimental to the performance of the ACHE. Again the effect on the second fan by the addition of the walk way is marginal. The dip in the volumetric effectiveness of fan 1 at $X = 1.12$ or $\frac{W_{ac}}{d_{FC}} = 1.5$ indicates that even though the fan is operating, the velocity of the air moving passed the fan inlet is sufficient to create a pressure difference greater then the fan static pressure rise. Thus the air is drawn through the fan in the opposite direction to which the fan is designed for. This reversed flow could be exacerbated by a strong wind, in the same direction as this cross flow.

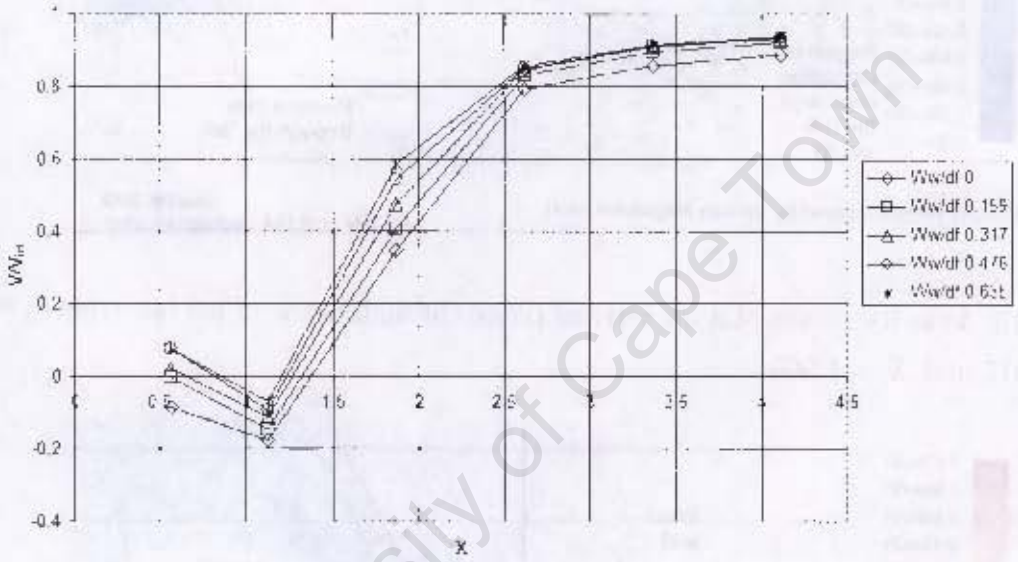

Figure 9.12: Effect of a walkway on the first fan of a 12 fan system

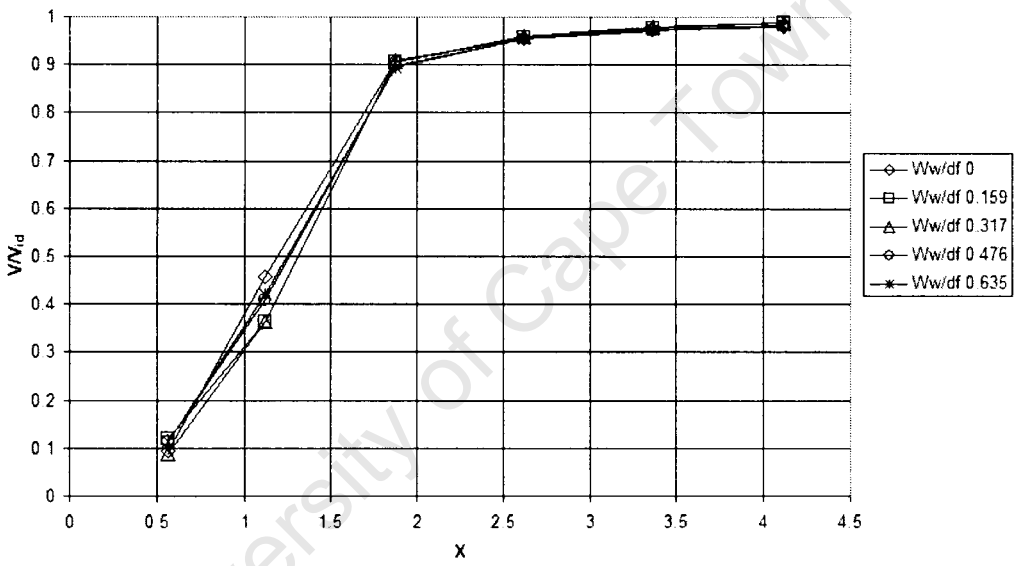

Figure 9.13: Effect of a walkway on the second fan of a 12 fan system

Chapter 10

Investigation of a NxM array of ACHE's

It has been shown that the periphery fan in an ACHE row that is part of an infinitely long ACHE bank operates at the lowest volumetric effectiveness. A finite length ACHE bank is, however, of more interest since it now contains a corner fan. The corner fan in such a bank will now be the first fan in two directions, but will have a larger area through which to draw in air. In this chapter it will be investigated whether the volumetric effectiveness of the corner fan now be better or worse off.

10.1 Geometry and Boundary Conditions

In this investigation, three different configurations of ACHE array's will be simulated. The geometry includes a bank that has 2x2, 4x4, and 6x6 fans. This was achieved by having 2 perpendicular symmetry plains, as shown in Figure (8.3), and using 1, 4, and 9 fans respectively. These configurations can be seen in Figures (10.1), (10.2), and (10.3). The atmospheric regions opposite the symmetry planes were made to be the same width as each other. Aside from this difference, the configuration is the same as that described in the previous chapters. The 6x6 ACHE array, which had approximately 8 million cells, was the largest to be simulated, as a 8x8 ACHE exceeded the computational resources available.

In the previous investigations the air was constrained to flow in the direction of fan 1 to fan N. In this investigation this was not the case as the ACHE was open to atmosphere on two sides now, instead of one. This made the solution much more sensitive to the

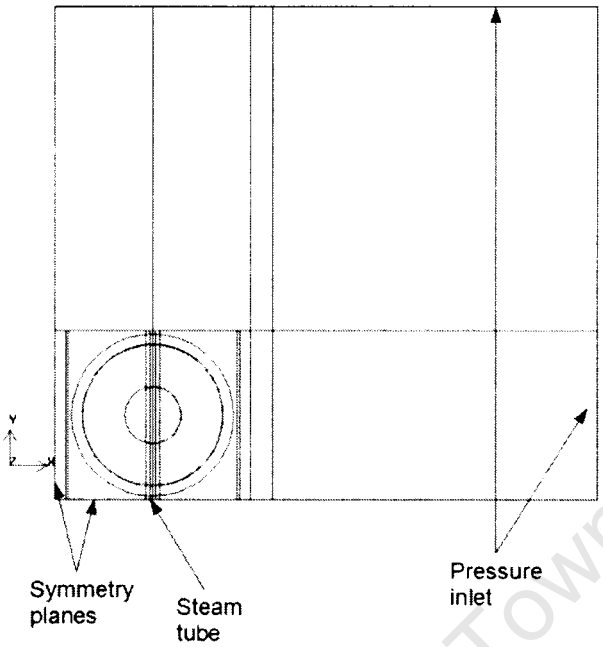

Figure 10.1: 2x2 ACHE schematic

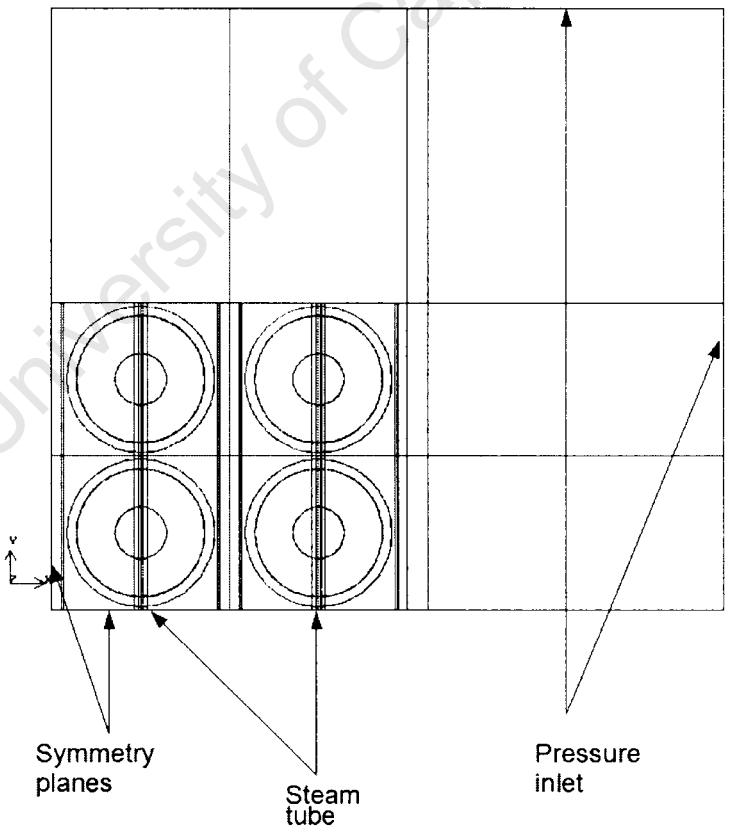

Figure 10.2: 4x4 ACHE schematic

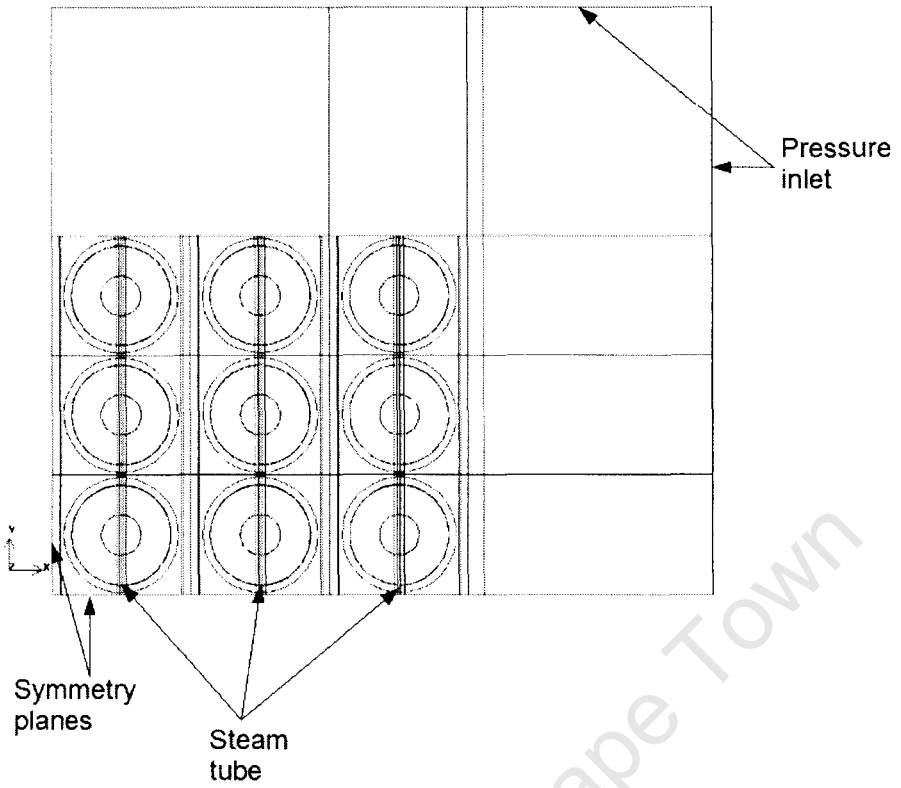

Figure 10.3: 6x6 ACHE schematic

mesh used. It was found that the mesh had to be predominantly hexahedral, otherwise the simulation did not converge properly; the residuals acted erratically. This is thought to be due the the less constrained nature of the flow field in the region of a corner in the ACHE bank. The mesh surrounding the ACHE array thus had to be refined. The ACHE row from an infinitely long ACHE bank, as investigated in previous chapters will be referred to as Nx1 ACHE banks for the rest of the report.

10.2 Results and Discussion

The empirical formula defined by Equation 8.1 that was used previously as a basis for comparison is not strictly valid in this section, as the ACHE's tested are not part of a infinitely long bank of ACHE rows. It is useful however to show how the peripheral fans at the edge of a bank of ACHE's perform in comparison to those in the middle of an infinitely long ACHE bank, where the empirical formula is valid.

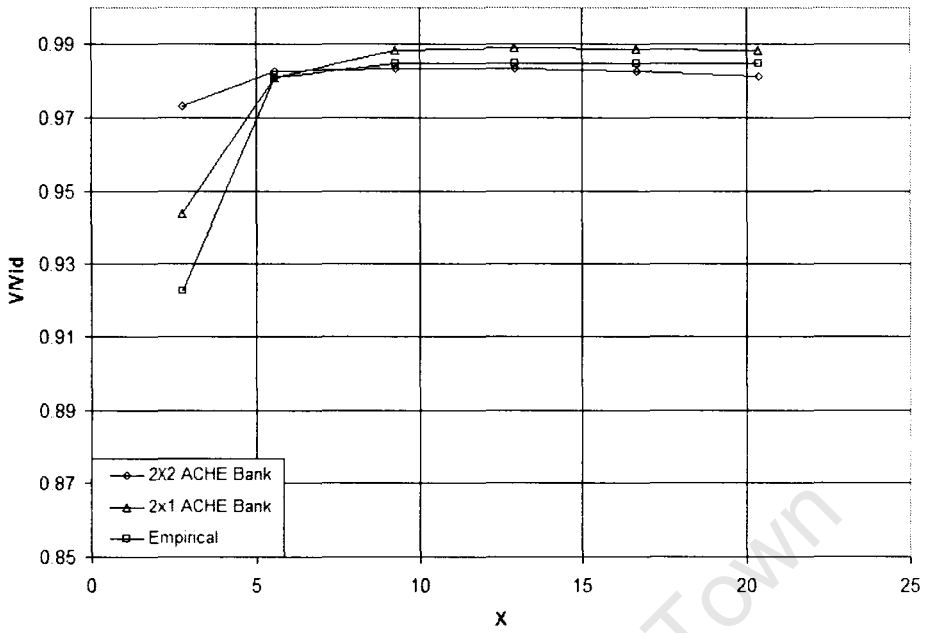

Figure 10.4: Comparison of volumetric effectiveness of a 2x2 bank of ACHE's

10.2.1 Results of the 2x2 ACHE bank

As a basis for comparison, the volumetric effectiveness of the Nx1 ACHE banks investigated previously will also be used to indicate the relative difference between results. This comparison is useful because it has been shown that the numerical and the empirical data have some discrepancies. An example of which can be seen in Figure (10.4).

From Figure (10.4) it can be seen that when not constrained on either side, the ACHE has a better volumetric effectiveness at lower platform heights. From this investigation it is still uncertain as to the cause of the improvement.

10.2.2 Results of the 4x4 ACHE bank

To investigate the possible cause of the improvement a 4x4 ACHE is modeled. A comparison of the system volumetric effectiveness of the 4x4 ACHE can be seen in figure (10.5). It is evident here that the system average volumetric effectiveness is higher then that of the Nx1 4 fan system. It was concluded that the edge fans must have some effect, and could be the cause of the improvement. The improvement could be due to the increased area that the fans can draw air from, which could have resulted in a lower

induced cross flow, but must be investigated further.

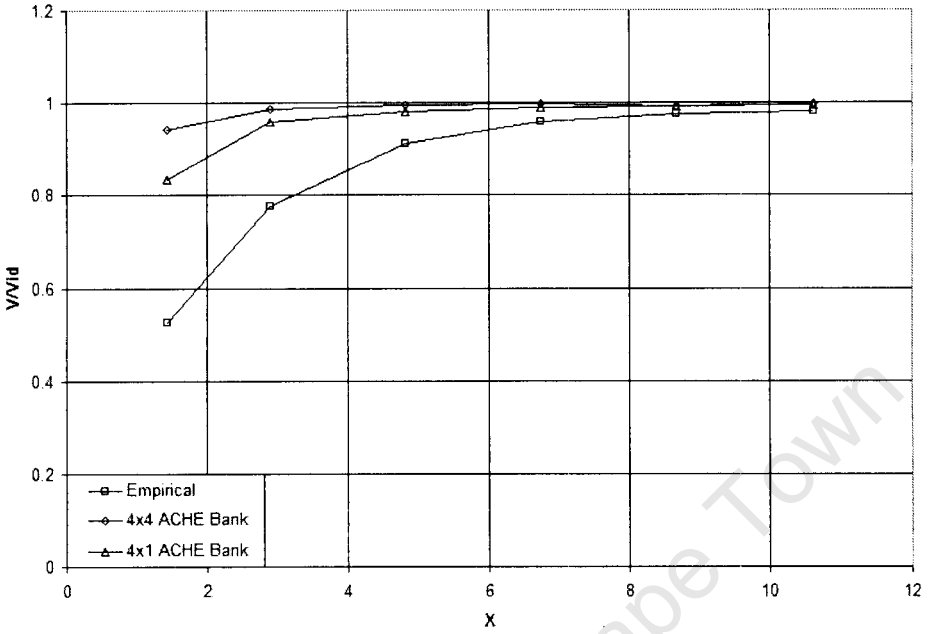

Figure 10.5: Comparison of the system volumetric effectiveness of a 4x4 ACHE

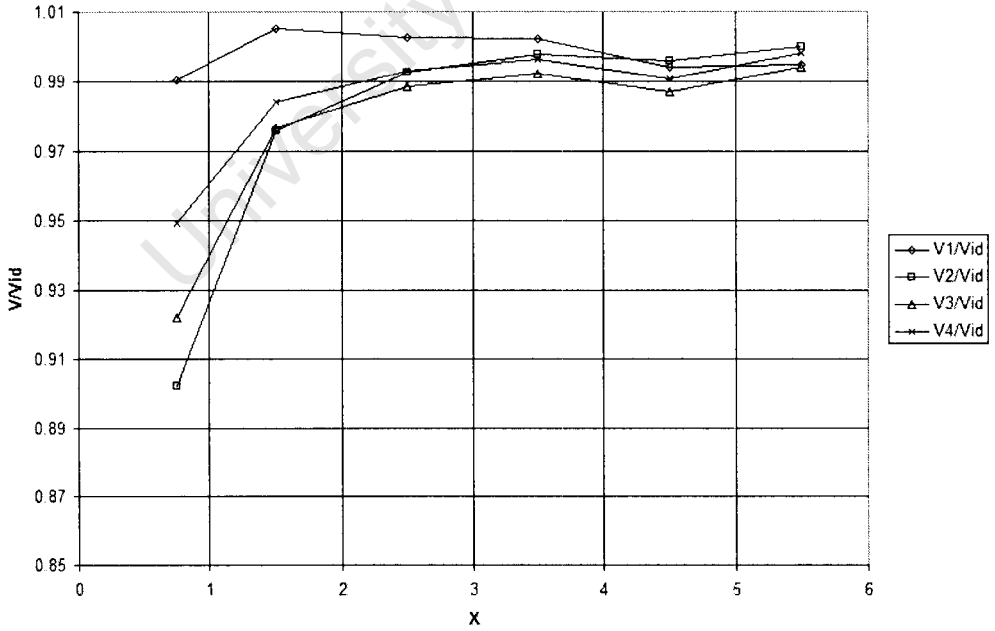

Figure 10.6: Comparison of volumetric effectiveness of each fan in a 4x4 ACHE

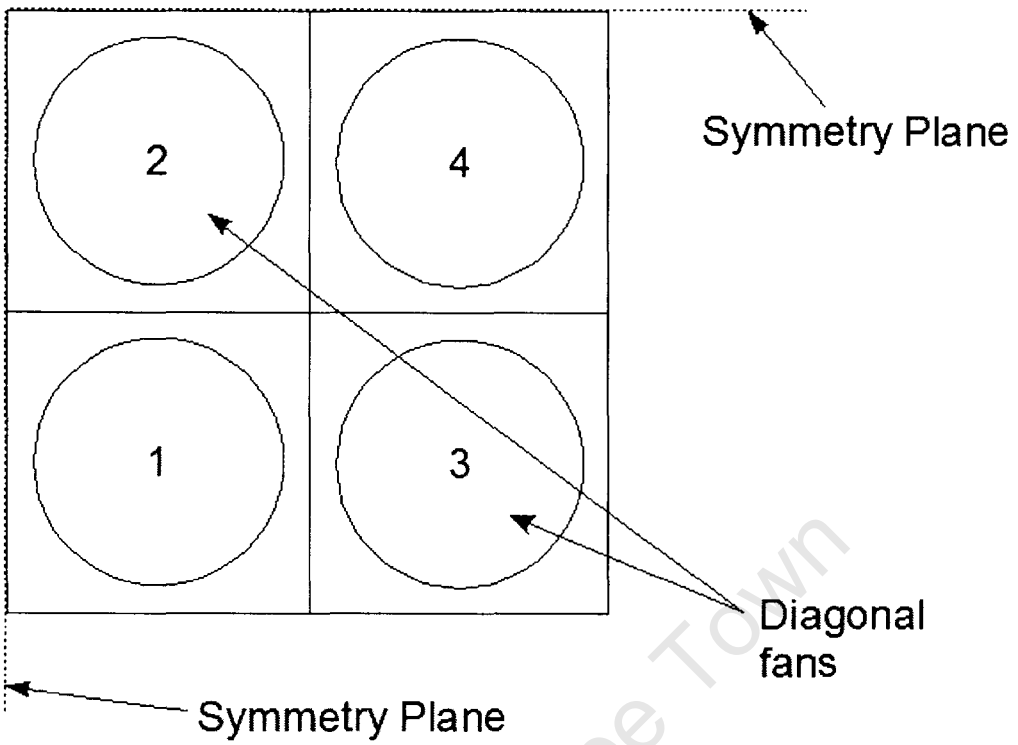

Figure 10.7: Diagrammatic representation of the diagonal fans in a 4x4 ACHE

The individual volumetric effectiveness of each fan in the 4x4 ACHE is plotted in Figure (10.6). This was done to investigate how the individual fans perform, thus finding which fans contributes to the improvement. Referring to Figure (10.7) fan 1 and fan 4 are almost symmetrical with respect to the diagonal (i.e. the line joining fan 2 and 3), except for the rotational direction of the fan. For this reason it is felt that they should perform approximately the same. The rotational effects should be negligible as they are constrained to be within the plenum. The flow acquires the rotational effects from the fan, and loses it at the heat exchanger. Since the flow can only leave the heat exchanger perpendicularly.

Figure (10.6) shows that the diagonal fans do not perform the same even though they do have the similar inlet conditions. The only geometric difference that could cause this is the orientation of the plenum. In the Nx1 ACHE bank's investigated previously all the plenum's were parallel to each other and were not connected. In the MxN array's the some of the plenums are connected.

10.2.3 Results of the 6x6 ACHE bank

If the manner in which the plenums are connected influences the volumetric effectiveness of the fans it should be more pronounced in a larger bank. This was the basis for simulating a 6x6 ACHE bank. Referring to Figure (10.8) it is evident that the 6x6 ACHE performs better than the 6x1 ACHE. This is consistent with the trend seen in a 2x2 and a 4x4 ACHE bank. The discrepancy between the fans that are situated symmetrically about the diagonal was again evident, as shown in Figure (10.9). The difference in volumetric effectiveness between these fans was approximately 0.1, which is larger than those of the 4x4 ACHE, which differ by only 0.05.

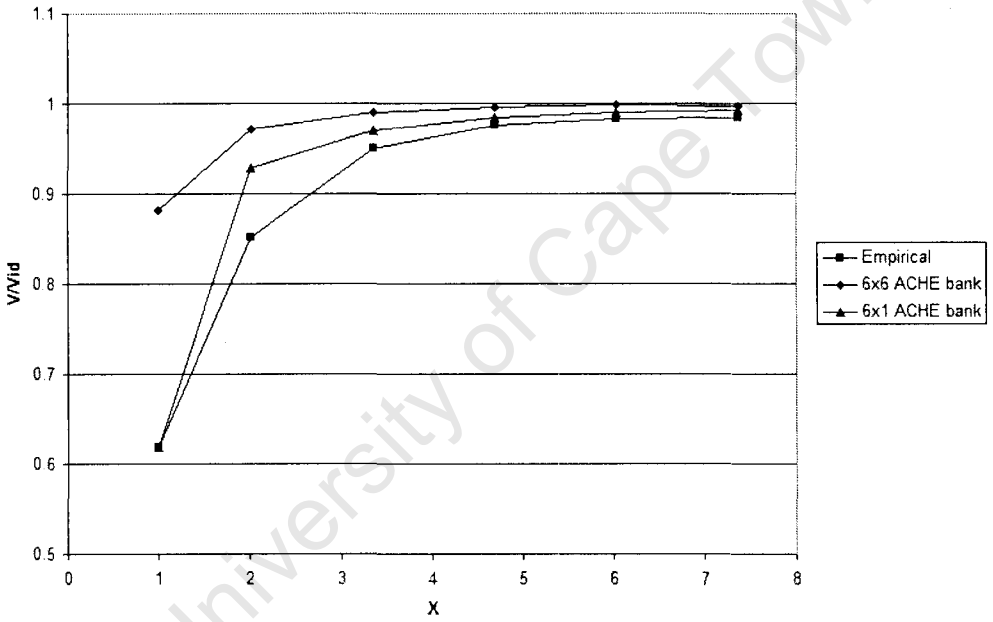

Figure 10.8: System average volumetric effectiveness of a 6x6 ACHE bank

In an attempt to determine the cause of this difference, the average volumetric effectiveness of the fans in the different rows was plotted. The fans were grouped together such that they had a constant X, such that the plenums were connected and a constant Y, such that the plenums were parallel. These plots can be seen in Figures (10.10) and (10.11).

It can be seen that the fans in any row do not perform the same as the fans in the position reflected about the diagonal, i.e., fan 1 and fan9. These fans are symmetrical

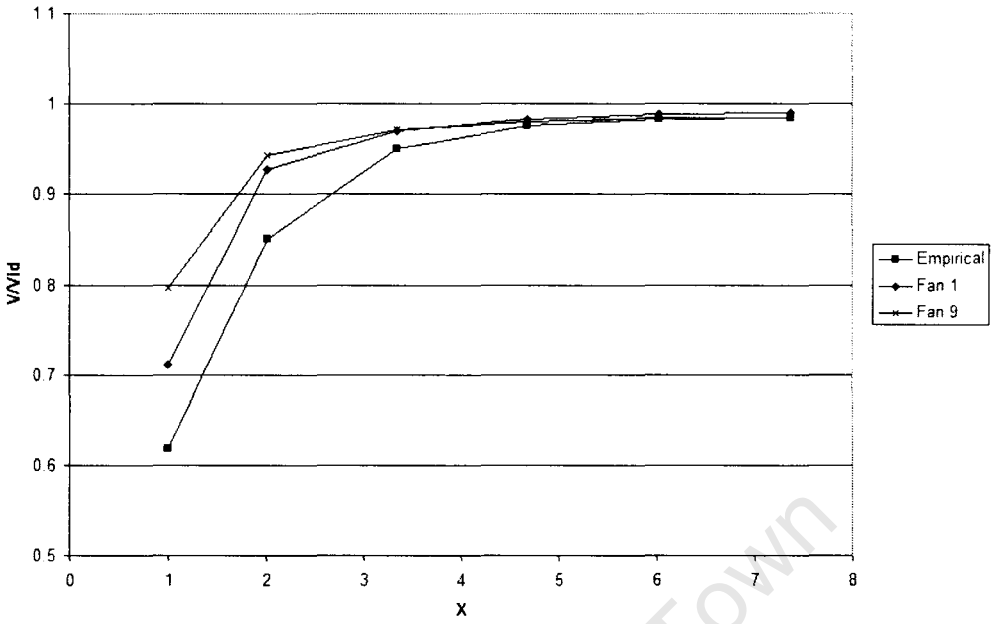

Figure 10.9: Individual fan volumetric effectiveness of fan 1 and fan 9 in a 6x6 ACHE bank

about the diagonal; in this case is the diagonal is the line joining fans 3, 5, and 7. With reference to Figure (10.11), it can be seen that fans 1, 4, and 7 perform worse then all the other fan combinations, performing worse than the empirical data. This suggests that the fans at the periphery of the ACHE bank, in the direction of the steam duct, experience some additional losses that were not anticipated.

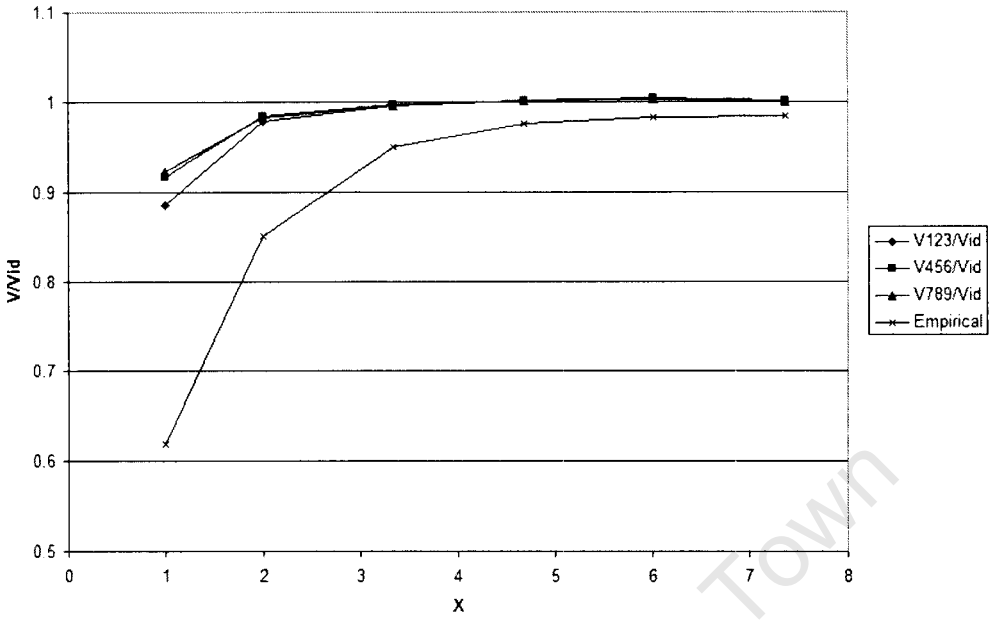

Figure 10.10: Fan volumetric effectiveness of fans that share a plenum in a 6x6 ACHE bank

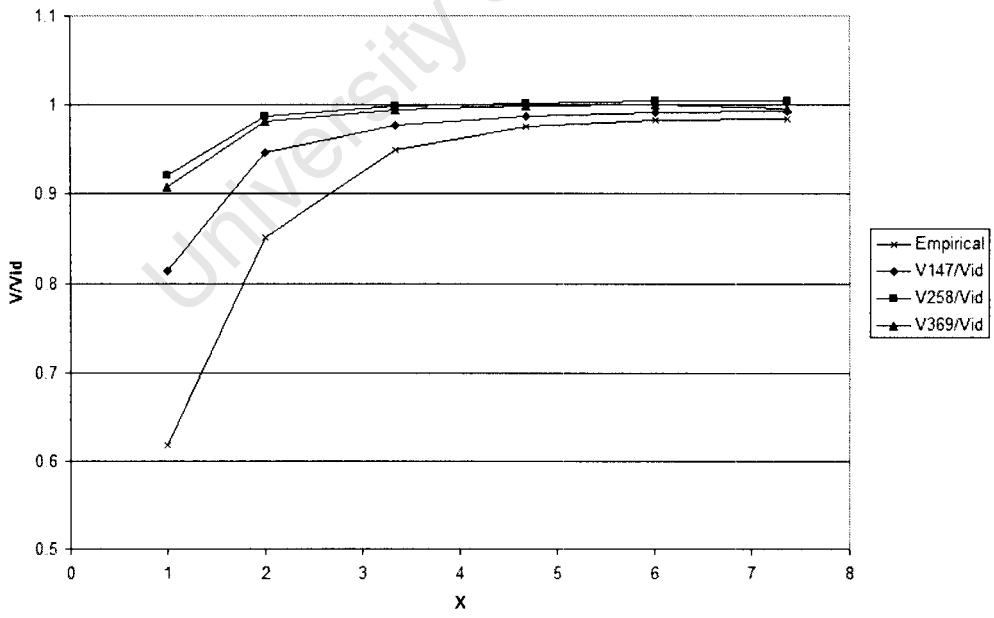

Figure 10.11: Fan volumetric effectiveness of fans that have the same Y co-ordinate in a 6x6 ACHE bank

10.2.4 Results of the 6x1 ACHE row with a joined plenum

It is clear that the orientation of the plenum does have an effect on the volumetric effectiveness, it was still unclear as to the cause of the difference found. For this reason further simulations were required. A 6x1 ACHE row with a joined plenum was therefore simulated in order to investigate the difference caused. It was thought that increasing the length of the ACHE row would increase the additional losses to the periphery fans that are in line with the joined plenum.

The geometry can be seen in Figure (10.12). All ACHE's connected in the same manner as Figure (10.12) will be referred to as joined plenum ACHE's, whereas all ACHE's connected as those in Figure (8.2) will be referred to as parallel plenum ACHE's.

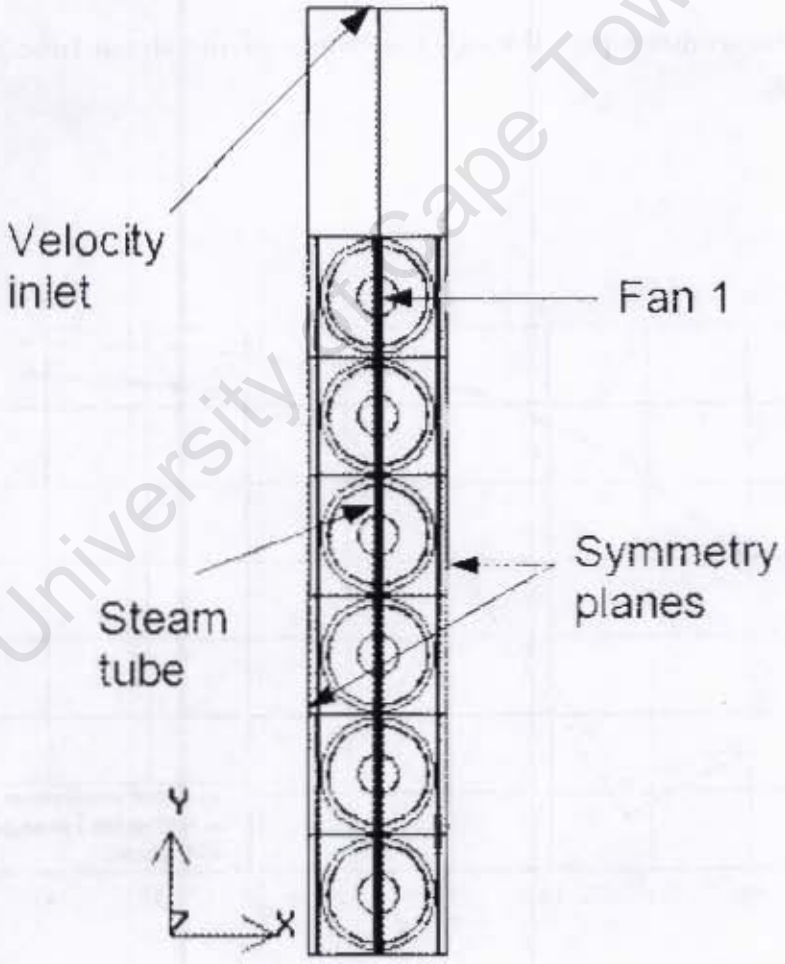

Figure 10.12: Schematic of the ACHE bank with a joined plenum used to investigate the effect of the orientation of the plenum

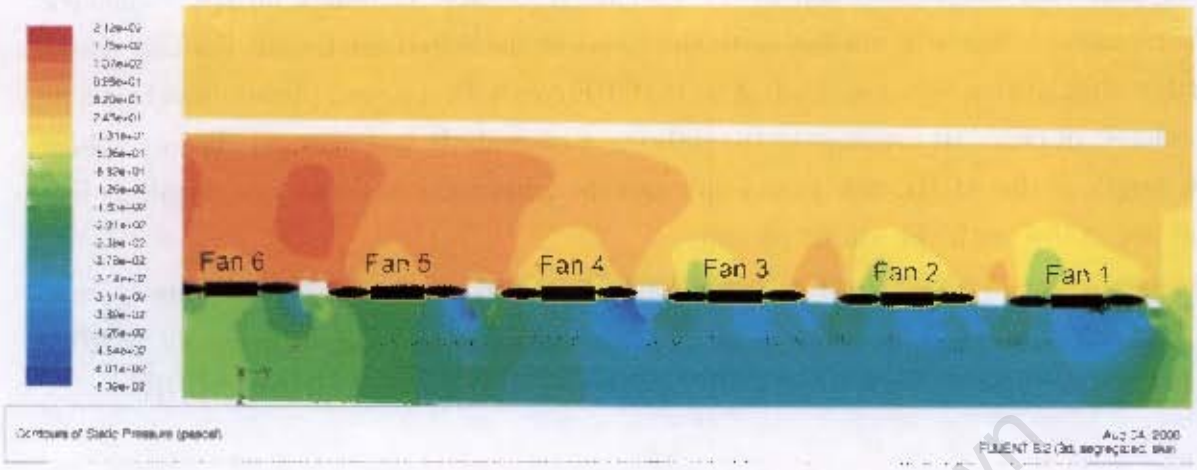

Figure 10.13: Static contour plot through the center of the steam tube of the joined plenum 6x1 ACHE

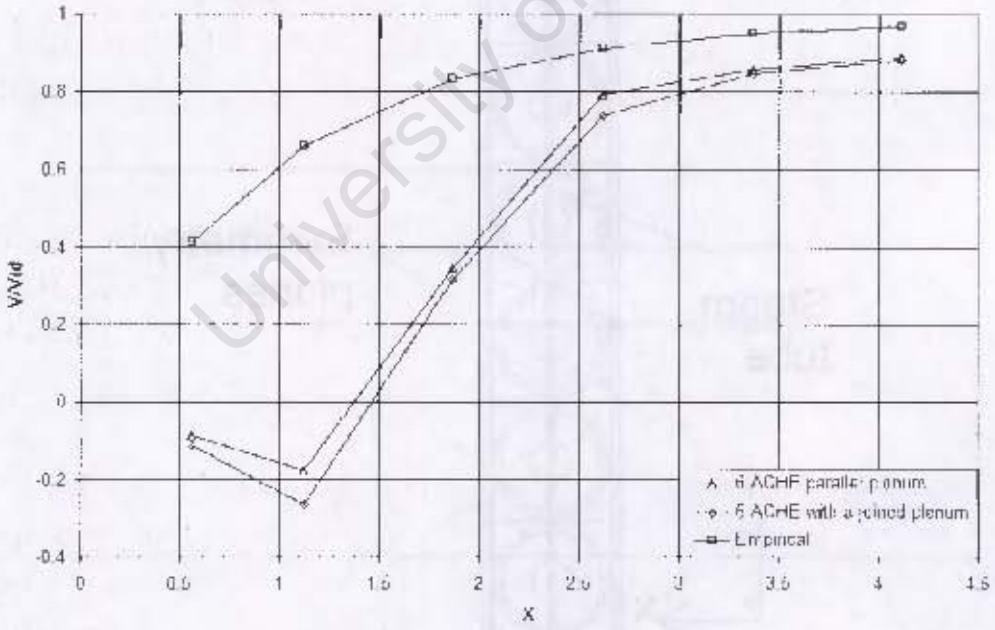

Figure 10.14: Comparison of the volumetric effectiveness of the first fan for different plenum orientations

Figure 10.15: Vector plot in the region of fan 4 and 3 showing the flow in the plenum moving toward the first fan

The static contour plot of the 6x1 ACHE row, shown in Figure (10.13), shows that the plenum above peripheral fans experience a lower pressure due to the decreased effectiveness. This pressure difference in the plenum along the ACHE row causes air to move from fan 6 to fan 1 to try to equalize the pressure. Since the air can move from fan 6 to fan 1, the static pressure at fan 1 became higher than for the parallel plenum case. This caused the fan to perform even worse then it did before, as shown by Figure (10.14). This was because the pressure difference across the fan was greater than before, which caused a larger reversed flow.

Figure (10.15) shows the vector plot in the region of the third and fourth fan. The tendency of the flow to move in the direction of fan 1 is clear. When consulting the path lines in Figure (10.16) it becomes apparent that the flow leaving the first fan now recirculates back into the plenum where it could possibly be caught up in the flow heading towards fan 1 again.

In an attempt to restrain the cross flow in the plenum, walls were set up such that they completely closed off the plenum between fan 1 and 2, and fan 2 and 3. The position of

Figure 10.16: Plot of the path lines released from the fans

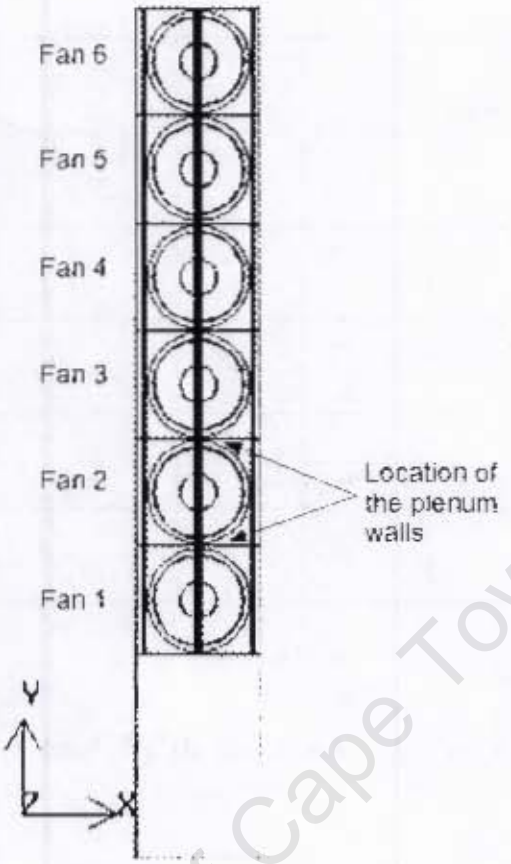

Figure 10.17: Schematic representation of the ACHE bank used to investigate the effect of plenum walls

the walls are shown in Figure (10.17).

The investigation was only carried out for $\frac{H_{EP}}{d_{FC}} = 0.75$. This is the height at which fan 1 and fan 2 perform the worst, making the cross flow in the plenum more pronounced. It was thought that separating these plenums would improve the volumetric effectiveness of fan 1 and fan 2. The reason for this is that the pressure effects should now be negated, making cross flow between the plenums of fan 1 and fan 2 impossible.

As seen in Figure (10.18) the result of this change was a slight decrease in performance of all but the second fan, which doubled it's flow rate. The doubling of the flow rate of fan 2 is thought to be because the cross flow no longer forces the flow leaving the one side of the fan back onto the other side of the same fan. This can be seen in Figure (10.19) and (10.20). Figure (10.20) shows how the flow leaving the positive y side of the fan can now move higher up in the plenum and exit the plenum, as opposed to being

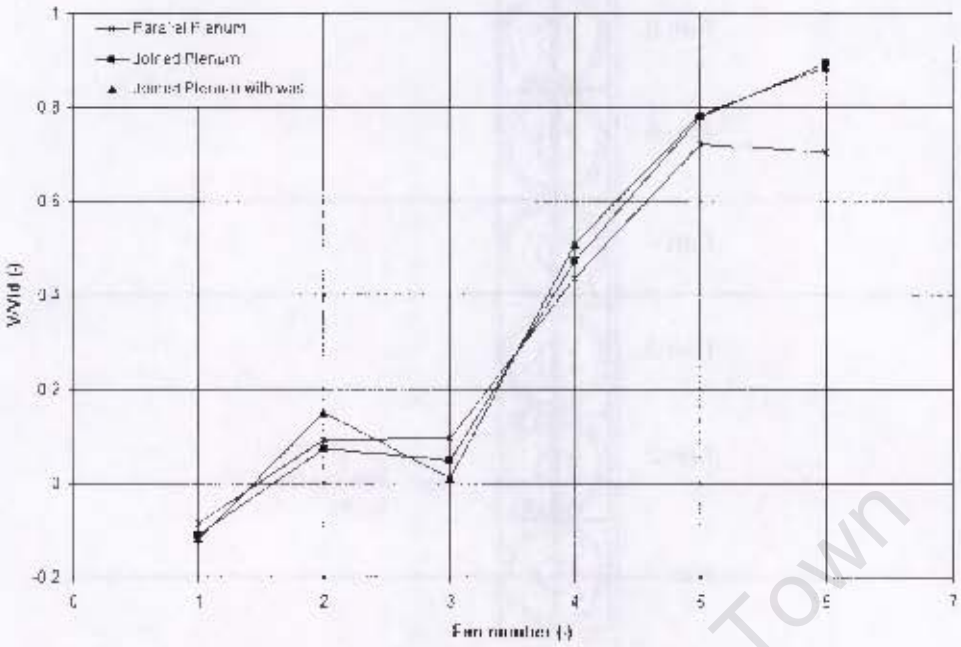

Figure 10.18: Volumetric effectiveness of a 6x1 ACHE bank with different plenum configurations

forced back onto the fan.

The volume flow rate of the cross flow between the plenums above fan 4 to 6 did not change much either. The results can be seen in Table 10.1. The maximum change was $V = 0.206m^3/s$ which occurred between the plenum of fan 4 and fan 5. However the volume flow rate across the plenum increased by this much. This implies that the atmospheric region above the heat exchanger must also have an effect on the negative effects experienced by fan 1 and fan 2. Further investigations into the possible cause of this is beyond the scope of this research.

	V_{34}	V_{45}	V_{56}
	m^3/s	m^3/s	m^3/s
No wall	4.868	3.684	1.723
Wall in plenum	4.821	3.890	1.745

Table 10.1: Comparison of the cross flow between the specified plenums with and with out plenum walls

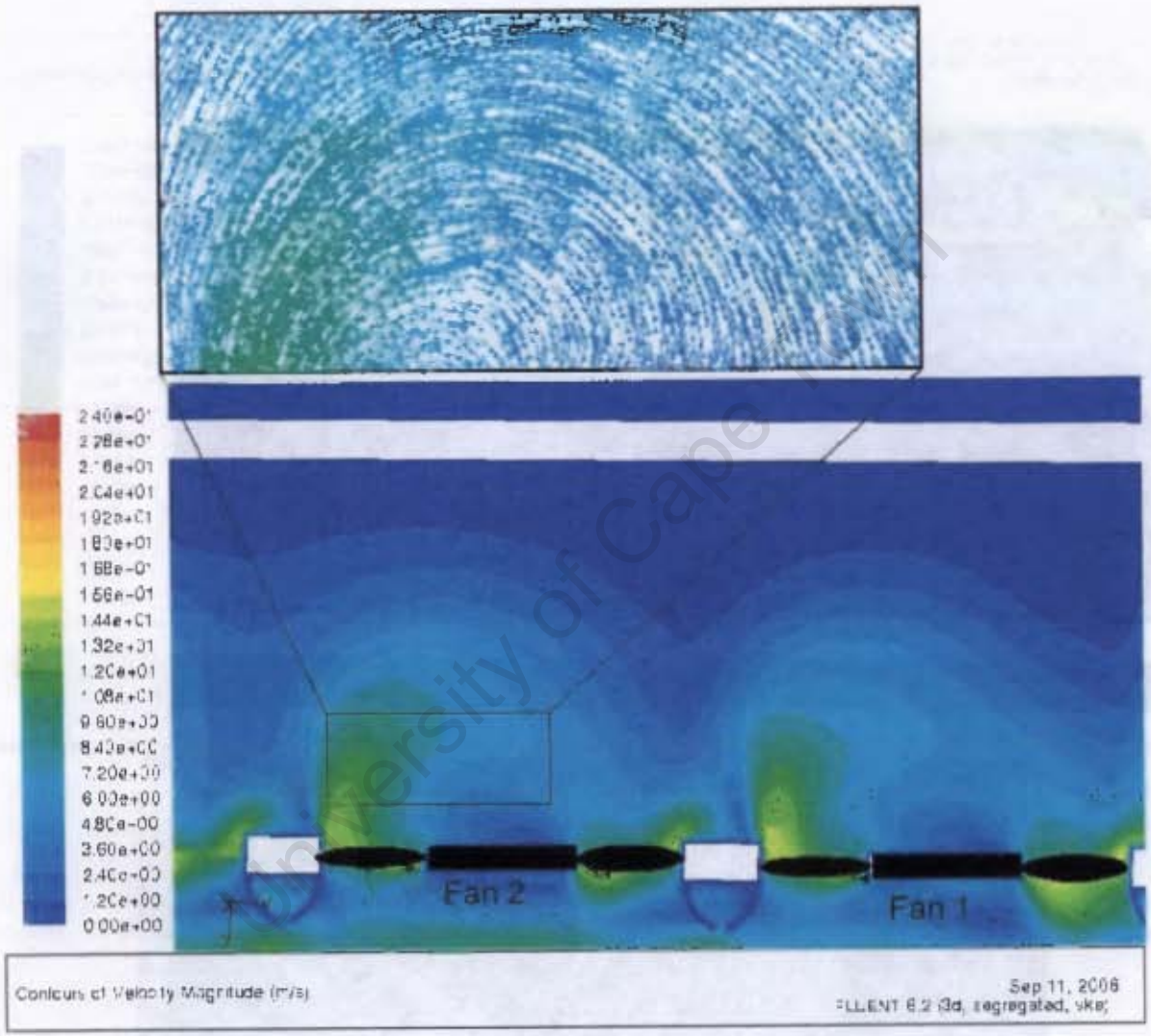

Figure 10.19: Contour and vector plot in the region of fan 2 that has no plenum walls

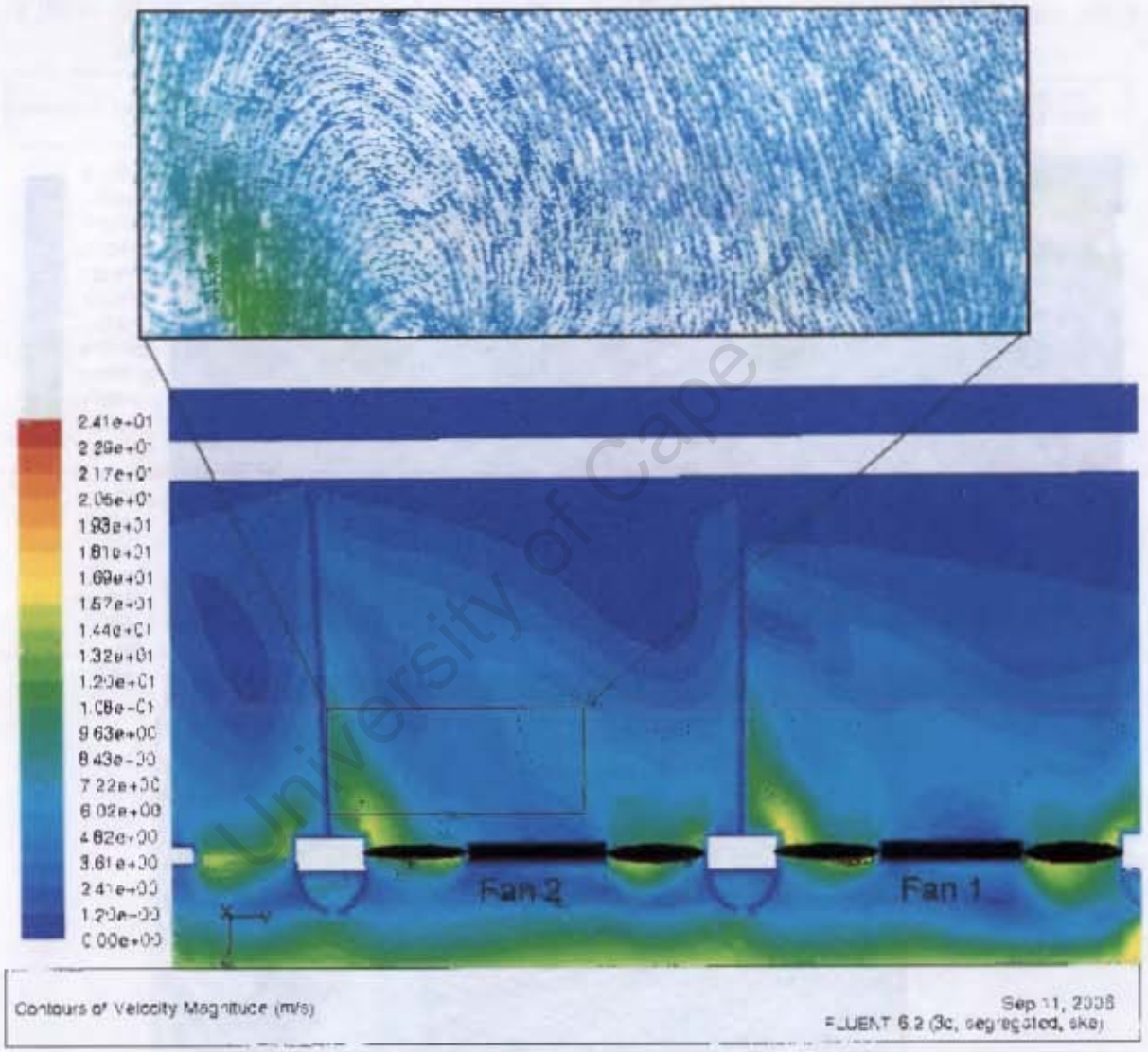

Figure 10.20: Contour and vector plot in the region of fan 2 that has plenum walls

Chapter 11

Investigation of the effect of wind

In the previous chapters and in literature [6, 7, 8, 9, 11] it has been shown that cross flows in the vicinity of the fans can have a detrimental effect on the fans' performance. In this chapter these detrimental effects will be exacerbated by the presence of wind. The worst case scenario is if the wind lies in the direction of the ACHE row, i.e. from fan 1 to fan N. A moderate wind speed of $10m/s$ will be tested. It was found by Coetzee and du Toit [12] that neglecting end effects could produce erroneous results. There is however no experimental data for a 2 dimensional array of ACHE's with which to compare to. There is however experimental data for a Nx1 system of fans that can be compared to [7], and will thus give an indication of the effect wind has on the fans. In Chapter 10 it was also shown that the edge effects are present without a wind profile at the periphery of a 2 dimensional ACHE bank. Therefore a single row of 12 ACHE's will be simulated, as the flow field is understood in more detail.

11.1 The Wind Profile

In order to simulate the effect of wind on a bank of ACHE's it is necessary to have and ACHE that is open on two opposite sides, so that the wind can enter the domain as well as leave it. Thus a ACHE bank that is comprised of 12 fans will be tested. Since the wind is expected to degrade the performance of the ACHE, an ACHE with a joined plenum will be investigated as it has been shown that an ACHE with a joined plenum performs marginally worse then one where the plenum's are parallel. As previously stated the wind profile will be approximated by the $\frac{1}{7}^{th}$ Power law.

For these simulation there is a mesh density change, between the inlet, the interior and

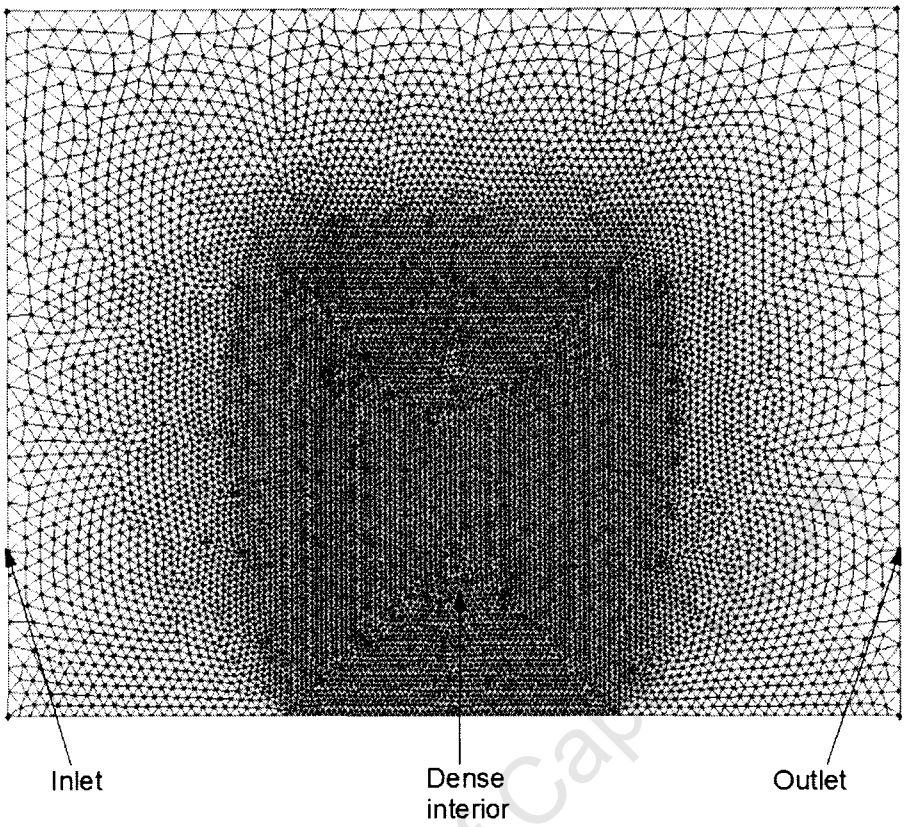

Figure 11.1: Mesh used to test the wind profile retension capability

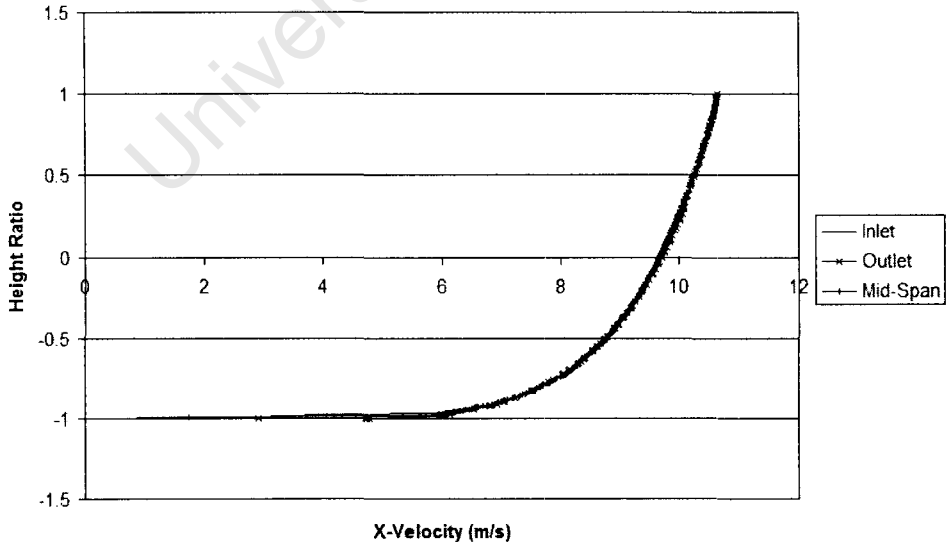

Figure 11.2: Plot of the velocity profile at different locations in the mesh

the outlet. The grid used is predominantly tetrahedral, and thus the number of cell faces perpendicular to the flow will be minimal, making numerical diffusion a possible problem. In order investigate this, and ensure that the velocity profile is retained through out the domain, a grid with a similar mesh density change was created. The grid used can be seen in Figure (11.1). The dense central region is surrounded by the same size atmosphere as the ACHE bank to be simulated. The velocity used was $10m/s$, and the reference height was set to be at a height ratio of 0. The height ratio is set up such that the top of the volume is at 1 and the bottom at -1, with 0 being the center.

The velocity profile is shown in Figure (11.2), it is evident that the velocity profile is indeed maintained, with negligible differences. Thus the change in grid density should not distort the wind profile.

11.2 Geometry and boundary conditions

The grid used to simulate an infinitely long bank of 12 ACHE's will be used for this investigation. Since 12 fans must be explicitly modeled, the ACHE bank will be copied and mirrored about the symmetry plane, as the symmetry plane can no longer be used. All the boundaries have the same boundary types and conditions as before, except for the boundary to which the wind profile will be attached. This boundary is set to a velocity inlet. The geometry can be seen in Figure (11.3). The wind profile is attached in such a manner that it will intersect fan 1 first and move toward fan 12.

Initially a wind speed of $10m/s$ was to be simulated, but after repeated attempts it was found that for some of the platform heights $10m/s$ was too fast for the current grid. At this wind velocity the solution did not converge for all the residuals were erratic. Since the grid size was at the upper most limit for the available resources, a finer mesh could not be generated. Therefore the wind speed was reduced to $3m/s$, as used by Coetzee and du Toit [12]. Using this wind speed, the simulations converged without any of the complications experienced by faster winds. $3m/s$ is however a very slow wind speed, being only $10.8km/h$, but it should be fast enough to reveal a trend. The reference height was held constant at the lowest fan platform height, $H_{ref} = 1.234m$, since the incoming wind profile is dependent on the conditions upstream of the ACHE, and will thus not change if the ACHE is raised or lowered.

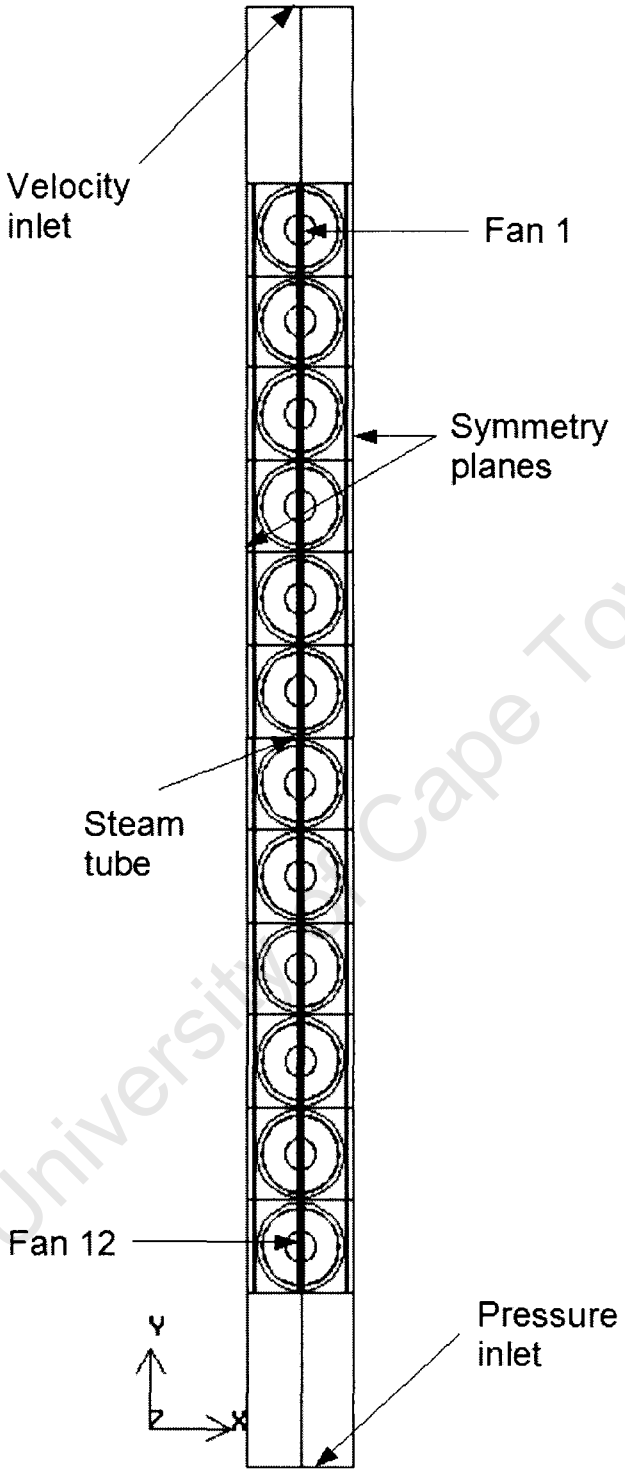

Figure 11.3: Schematic of the bank of 12 ACHE's used to investigate wind effects

11.3 Results and Discussion

A comparison of the system volumetric effectiveness can be seen in Figure (11.4). The empirical curve is included to give a better indication of the change. It is evident that the presence of wind lowers the volumetric effectiveness curve. The difference is not substantial, but it is expected to increase as the wind speed increases. As a further comparison the individual volumetric effectivenesses are plotted in Figures (11.5) to (11.10) against those for windless conditions. The fans that are potted are those that are the same distance from the periphery of the ACHE bank. For instance fan 1 from the windless conditions is compared to fan 1 and fan 12 with the effects of wind. In windless conditions fan 1 and fan 12 perform the same, due to symmetry, and thus only the first six fans are used for comparison. If the presence of wind has no effect on the volumetric effectiveness of the bank of ACHE's, the 2 plots should be identical.

The similarity of the volumetric effectiveness of fan 12 with wind, and fan 1 without wind suggests that at this velocity, the effects of wind do not reach all the way through to the last fan. Looking at the volumetric effectiveness of fan 8 and fan 9 with wind for the lowest platform height, it is obvious that the wind eventually gets entrained in the flow entering the fans, and in this case improves the performance.

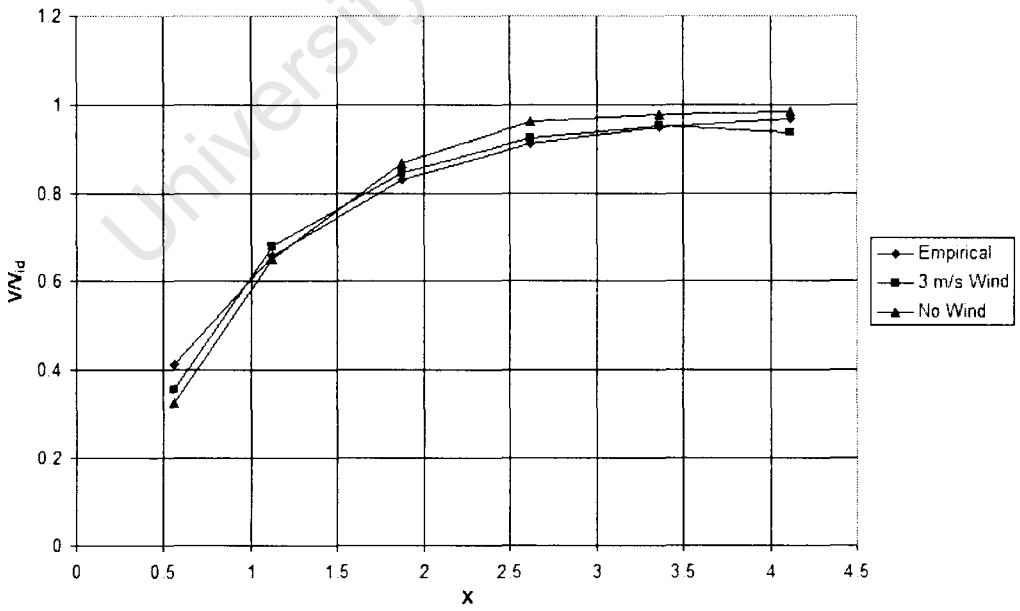

Figure 11.4: System volumteric effectiveness for a bank of 12 ACHE's in the presence of wind

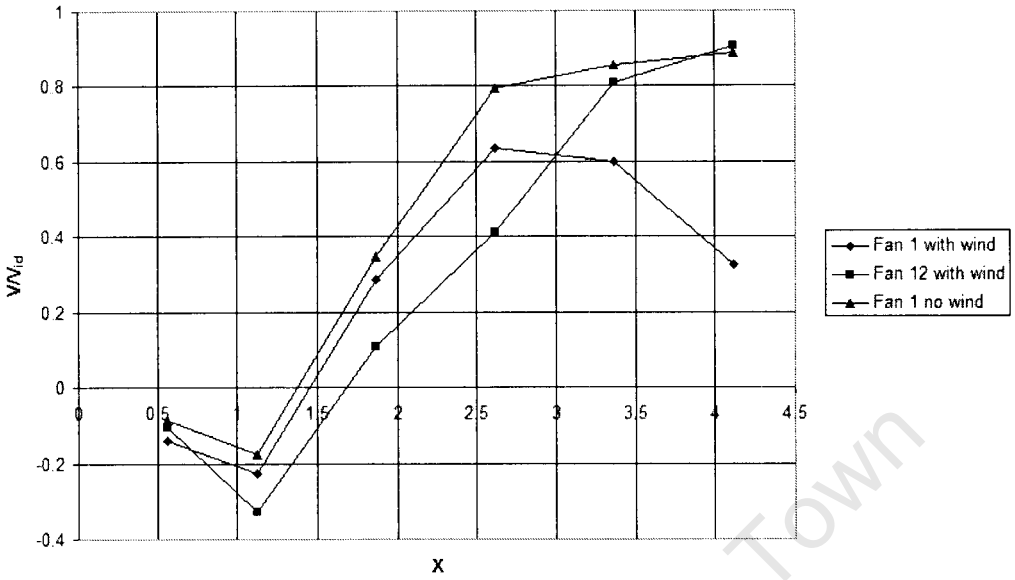

Figure 11.5: Comparison of the volumetric effectiveness of fan 1 and 12

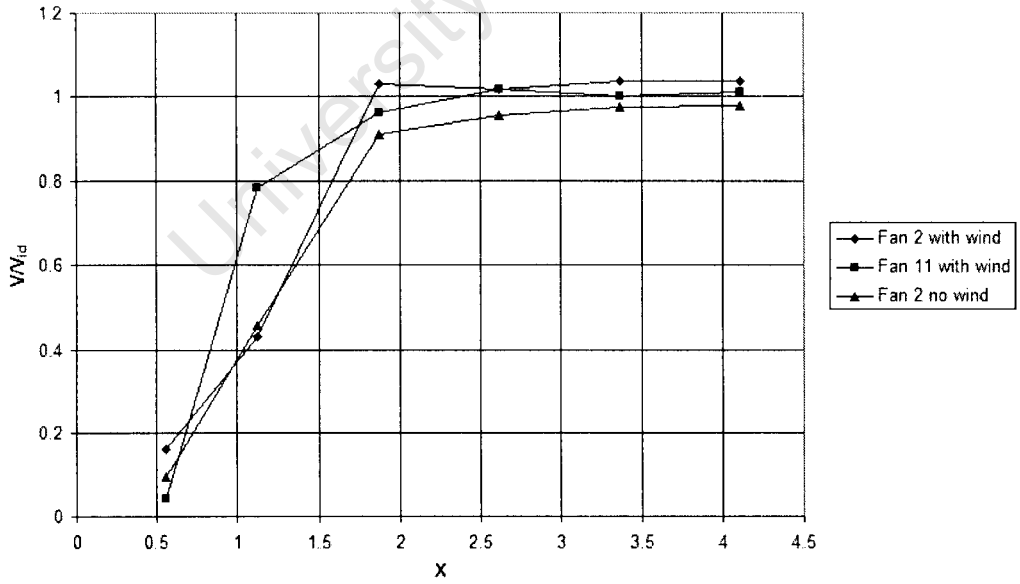

Figure 11.6: Comparison of the volumetric effectiveness of fan 2 and 11

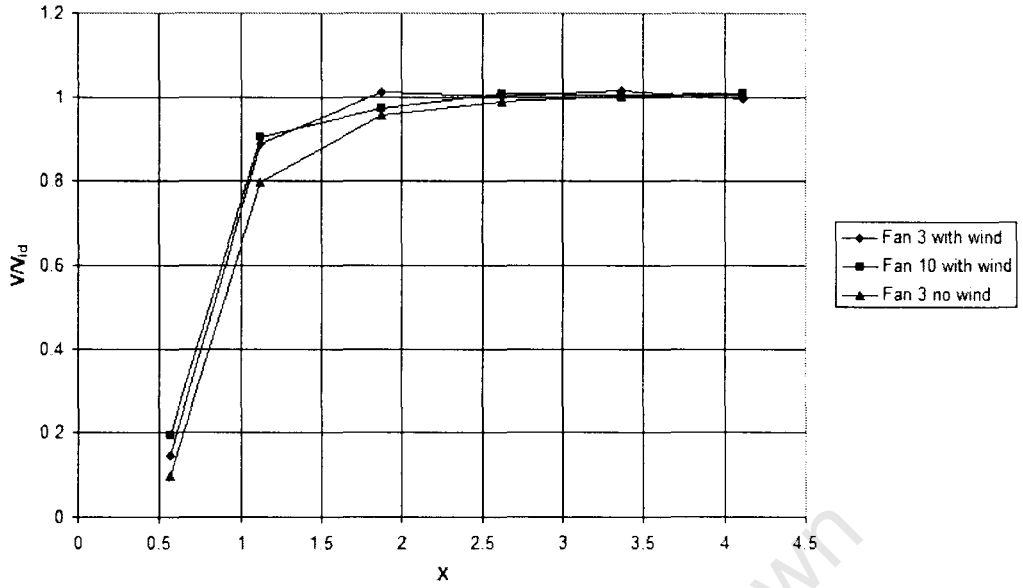

Figure 11.7: Comparison of the volumetric effectiveness of fan 3 and 10

The dip in the volumetric effectiveness of fan 1 at higher platform heights is thought to be due to the increased wind speeds at this height. As the fan platform is raised, it encounters a higher velocity cross flow, since the reference height is held constant. The increased cross flow, as shown previously, has a detrimental effect hence lowering the volumetric effectiveness.

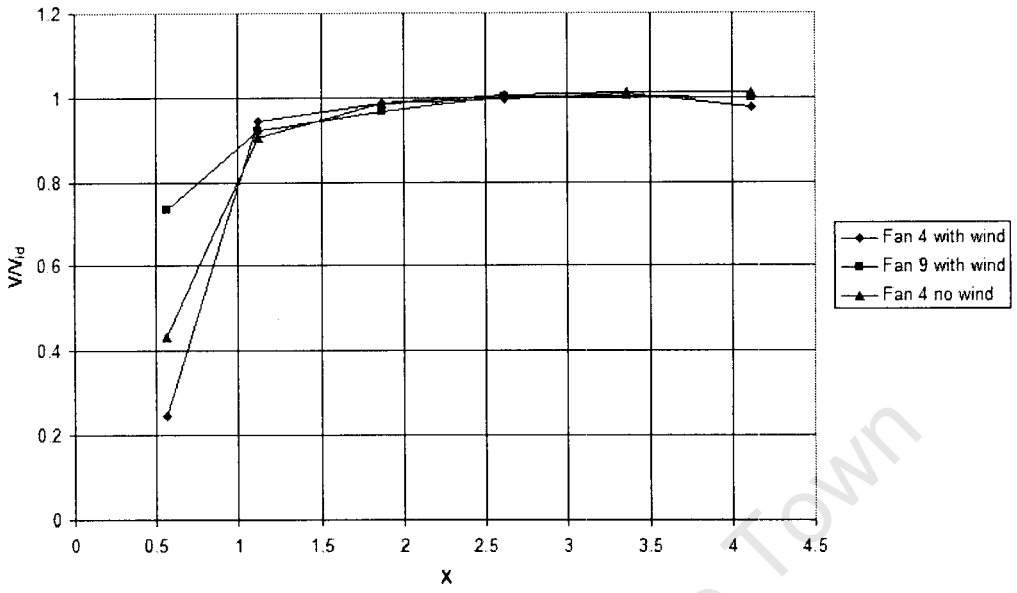

Figure 11.8: Comparison of the volumetric effectiveness of fan 4 and 9

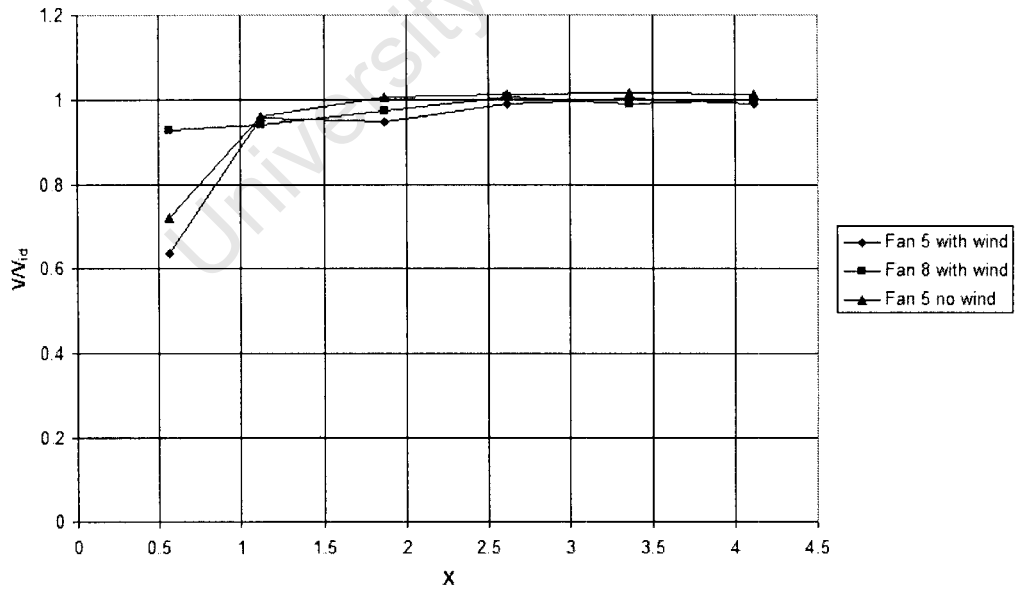

Figure 11.9: Comparison of the volumetric effectiveness of fan 5 and 8

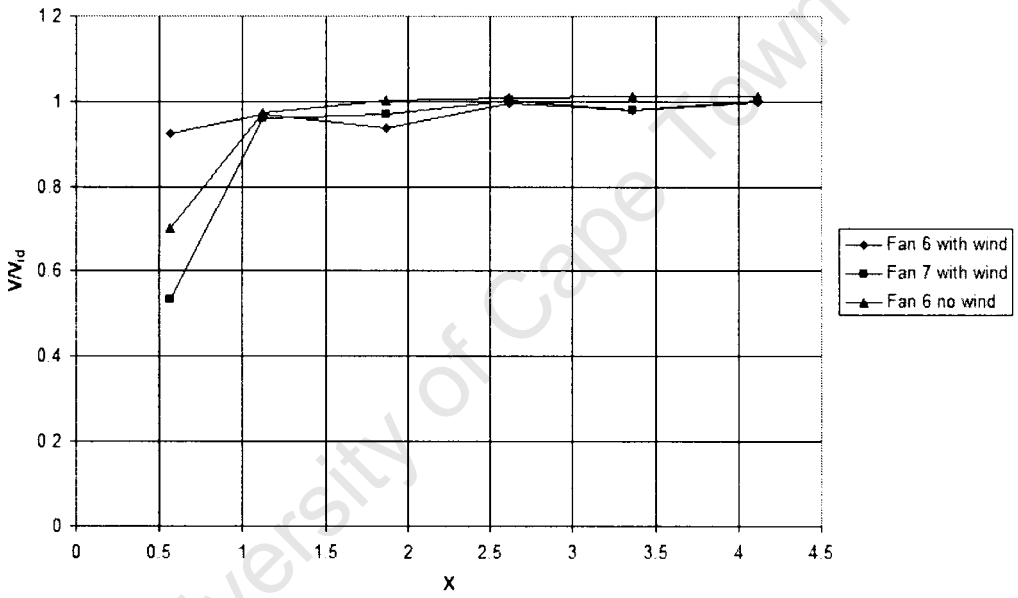

Figure 11.10: Comparison of the volumetric effectiveness of fan 6 and 7

Chapter 12

Conclusions and Recommendations

12.1 Conclusions

In these investigations numerous different models were used, and the results compared to experimental results reasonably well. Thus it can be concluded that the actuator disk fan model does indeed simulate the flow field in the region of an axial flow fan, having a good correlation to the experimental results. The turbulence models available in FLUENT® are sufficient for the purposes of investigating an axial flow fan, however a stable turbulence model that can deal with the axial flow fan and the wind profile, or bluff body flow, needs to be investigated.

The heat exchanger was modeled as a porous region, the governing equations have been stated. A heat exchanger performance characteristics can be accurately simulated using the governing equation, Equation (6.14) and a known pressure drop relationship across a heat exchanger.

Using the fan model as well as the porous region for the heat exchanger produce realistic flow rates through the fan. The flow rates are consistent with experimental results as well as empirical data. By changing the viscous and inertial resistance of the porous region, any realistic operating point can be achieved.

When simulating the ACHE, it was found that the ground clearance played a substantial role in the ACHE's volumetric effectiveness. It was found that with the addition of a walkway at the edge of the ACHE improved the periphery fans performance, but increasing the walkway length to much could have detrimental effects.

In the investigation of a 2 dimensional array it was found that edge effects play a part in the flow field of a bank of ACHE's, especially in the region of the corner fans. The plenum chamber's orientation also had an effect on the volumetric effectiveness of the ACHE. When the plenums of an ACHE row were parallel to each other the overall system volumetric effectiveness was higher then when the plenums were joined.

When wind was included to the ACHE row with a joined plenum, it was found that the volumetric effectiveness curve was lowered, i.e. wind has a similar effect as a slight lowering of the fan platform. With the low wind speed simulated it is difficult to determine the extent of this effect. It was also found that the effects of a given wind speed were dependent on the fan platform height.

12.2 Recommendations

First and foremost, it is recommended that experimental data be obtained for the 2 dimensional array. A small arrangement, i.e., 2x2 fans, should be sufficient to verify the numerical trends. The experimentation should use the same type of plenum as the numerical investigation, as it has been shown that the plenum has an effect on the flow field.

In order to better investigate the effect of wind, a smaller bank of ACHE's should be modeled, so as to increase the grid density above the plenum. A bank of 10 ACHE's could be used, as this should allow a sufficient decrease in cells to refine the region downstream of the plenum, as well as the plenum itself. It was stated that the $k-\epsilon$ turbulence model is incorrect for bluff body flow, which will be experienced when wind is included in the simulations. For this reason some of the turbulence models used for Wind Engineering should be incorporated in some manner, when higher wind speeds are investigated. However this means that either the turbulence model must be coded by the user as a user defined function.

This investigation was treated as being iso-thermal, but ACHE's are inherently thermal devices. The thermal effects of the heat exchanger should thus also be investigated. As the air passes over the heat exchanger it will heat up, and thus lower it's density. This density change will create a buoyancy effect [6], which will make the air leaving the heat exchanger tend to rise faster then the iso-thermal case. This could be done by using a

user defined function, since the temperature in a heat exchanger is not constant over its surface

In order to simulate larger configurations a computer with a large amount of memory is required, in these simulations the computers used had 4 GB of memory. The grid was reduced as much as possible, while maintaining the accuracy of solution.

For the purposes of design it is recommended that the orientation of the plenum be taken into account when selecting the fans. Since fans that are closer to the periphery in a joined plenum ACHE operate at a lower flow rate, the fans here should produce a higher fan static pressure then fans near the middle. In some cases a higher fan static pressure rise can simply be achieved by changing the fan blade root stagger angle. A steeper blade root stagger angle produces a higher fan static pressure rise, but increases the power consumption [33]. By varying the blade root stagger angle as a function of the distance from the periphery of the ACHE bank could thus produce a more constant pressure distribution in the plenum, thus helping reduce cross flow between the plenums.

References

[1] C.J. Meyer and D.G. Kröger. Numerical simulation of the flow field in the vicinity of an axial flow fan. *International Journal for Numerical Methods in Fluids*, 36:947–969, 2001.

[2] FLUENT Inc. *FLUENT® 6.2 UDF Manual*, January 2005.

[3] P.R.P. Bruneau. The design of a single rotor axial flow fan for a cooling tower application. Master's thesis, Department of Mechanical Engineering, University of Stellenbosch, South Africa, 1994.

[4] W.H. Stinnes. An experimental investigation for rotor-only axial flow fans for cooling tower application. Master's thesis, Department of Mechanical Engineering, University of Stellenbosch, South Africa, 1999.

[5] C.J. Meyer and D.G. Kröger. Numerical investigation of the effect of fan performance on forced draught air-cooled heat exchanger plenum chamber aerodynamic behavior. *Applied Thermal Engineering*, 24:359–371, 2004.

[6] D.G. Kröger. *Air-cooled Heat Exchangers and Cooling Towers.* Self Publication, 1998.

[7] C.A. Salta and D.G. Kröger. Effect of inlet flow distortions on fan performance in forced draught air-cooled heat exchangers. *Heat Recovery Systems & CHP*, 15(6):555–561, 1995.

[8] W.H. Stinnes and T.W. Von Backström. Effects of cross-flow on the performance of air-cooled heat exchanger fans. *Applied Thermal Engineering*, 22(12):1403–1415, 2002.

[9] K. Duvenhage, J.A. Vermeulen, C.J. Meyer, and D.G. Kröger. Flow distortions at the fan inlet of forced draught air-cooled heat exchangers. *Applied Thermal Engineering*, 16(8/9):741–752, 1996.

[10] G.D. Thiart and T.W. von Backström. Numerical simulation of the flow field near an axial flow fan operating under distorted inflow conditions. *Journal of Wind Engineering and Industrial Aerodynamics*, 45:189–214, 1993.

[11] C.J. Meyer. Numerical investigation of the effect of inlet flow distortions on forced draught air-cooled heat exchanger performance. *Applied Thermal Engineering*, 25(11-12):1634–1649, 2005.

[12] R.V. Coetzee and C.G. du Toit. Numerical modelling of an air-cooled heat exchanger: Influence of end-effects on results. *R&D Journal*, March, 2004.

[13] H.K. Versteeg and W. Malalasekera. *An Introduction to Computational Fluid Dynamics.* Prentice Hall, Harlow, 1995.

[14] FLUENT Inc. *FLUENT® 6.2 Documentation*, January 2005.

[15] Elizabeth Marden Marshall and André Bakker. *COMPUTATIONAL FLUID MIXING.* Fluent Inc. Lebanon, 2002.

[16] D.C. Wilcox. *Turbulence Modeling for CFD.* DCW Industries, Inc., La Canada, California, 1998.

[17] B.E. Launder and D.B. Spalding. The numerical computation of turbulent flows. *Computer methods in Applied Mechanics and Engineering*, (3):269–289, 1974.

[18] F.R. Menter. Two-equation eddy-viscosity turbulence models for engineering applications. *AIAA Journal*, 32(8):1598–1605, August 1994.

[19] D.O. Dommasch. *Elements of Propeller and helicopter Aerodynamics.* Pitman Publishing Corporation, 1953.

[20] R. Von Mises. *Theory of flight.* McGraw-Hill Book Company Inc., London, 1945.

[21] RJ. McGhee. Low-speed aerodynamic characteristics of a 17-percent-thick airfoil section designed for general aviation application. N74-11821, December 1973.

[22] S.F. Hoerner and H.V. Borst. *Fluid-dynamic Lift.* Published by Mrs L.A. Hoerner: Brick Town, South Africa, 1975.

[23] S.F. Hoerner. *Fluid-dynamic Drag.* Published by S.F. Hoerner: Brick Town, South Africa, 1965.

[24] Bao-Shi Shiau and Shih-Chang Hsu. Measurement of reynolds stress structure and turbulence characteristics of the wind above a two dimensional trapezoidal shape of a hill. *Journal of Wind Engineering and Industrial Aerodynamics*, 91:1237–1251, 2003.

[25] Aishe Zhang, Cuilan Gao, and Ling Zhang. Numerical simulation of the wind field around different building arrangements. *Journal of Wind Engineering and Industrial Aerodynamics*, 93:891–904, 2005.

[26] E.G. Tulapurkara, B.H.L. Gowda, and J.S. Chaukar. Mean velocity field around prismatic bodies in tandem arrangement. *Journal of Wind Engineering and Industrial Aerodynamics*, 93:777–796, 2005.

[27] D.I. Dunn. Numerical modelling of the flow through a forced draught air-cooled heat exchanger. BSc Thesis, University of Cape Town, October 2004.

[28] P. Hotchkiss. Development of a rotor model for the numerical simulation of helicopter exterior flow fields. Master's thesis, Department of Mechanical Engineering, University of Cape Town, South Africa, 2004.

[29] Robert N. Meroney. CFD prediction of cooling tower drift. *Journal of Wind Engineering and Industrial Aerodynamics*, 94:463–490, 2006.

[30] Paulo J. Oliveira and Bassam A. Younis. On the prediction of turbulent flows around full-scale buildings. *Journal of Wind Engineering and Industrial Aerodynamics*, 86:203–220, 2000.

[31] Shuzo Murakami. Overview of turbulence models applied in cwe-1997. *Journal of Wind Engineering and Industrial Aerodynamics*, 74-76:1–24, 1997.

[32] Shuzo Murakami. Current status and future trends in computational wind engineering. *Journal of Wind Engineering and Industrial Aerodynamics*, 67&68:3–34, 1997.

[33] C.J. Meyer and D.G. Kröger. A numerical investigation of the errors associated with the scaling of axial flow fan performance characteristics. *R&D Journal*, 20(2), 2004. Incorporated into The SA Mechanical Engineer.

[34] B.B. Daly. *Woods practical guideto fan engineering.* Woods of Colchester Ltd., Colchester, 1978.

[35] C.J. Meyer. Plenum losses in forced draught air-cooled heat exchangers. Master's thesis, Stellenbosch, 1996.

Appendix A

Parallelization of UDF

In order to decrease the time to solution and increase the computational resources, FLUENT® can partition the given domain, and distribute it amongst a number of computers, or processors in the case of multi-processor computers. The computers or processors that are not hosting the simulation are commonly referred to as compute nodes, or simply nodes [2]. Increasing the number of nodes allows for an increase in computational power as well as an increase of system resources. This allows for a more complex mesh to be used, as well as a larger domain. The down fall of this however is that the effectiveness of additional computers decreases as more computers are added, which is due to a variety of reasons, including larger amounts of data must be transfered, and to more locations.

A.1 FLUENT processes used for parallel

Parallel FLUENT® is made up of 3 separate processes, namely the Cortex, the host, and the nodes [2]. The cortex is mainly responsible for user interface and graphic related functions. The host is responsible for interpreting the commands given to it by the cortex, and distributing these commands and data to the nodes. The nodes in turn hold all the data. Each of the nodes will perform the calculations on their data, which will be a portion of the total mesh with regions that over-lap the mesh on another node, as seen in Figure (A.4), this is in order to ensure continuity and to enable communications between nodes.

The nodes are number 0 to $n-1$, where n is the number of nodes used. The host process communicates directly with node 0, which in turn communicates with all the

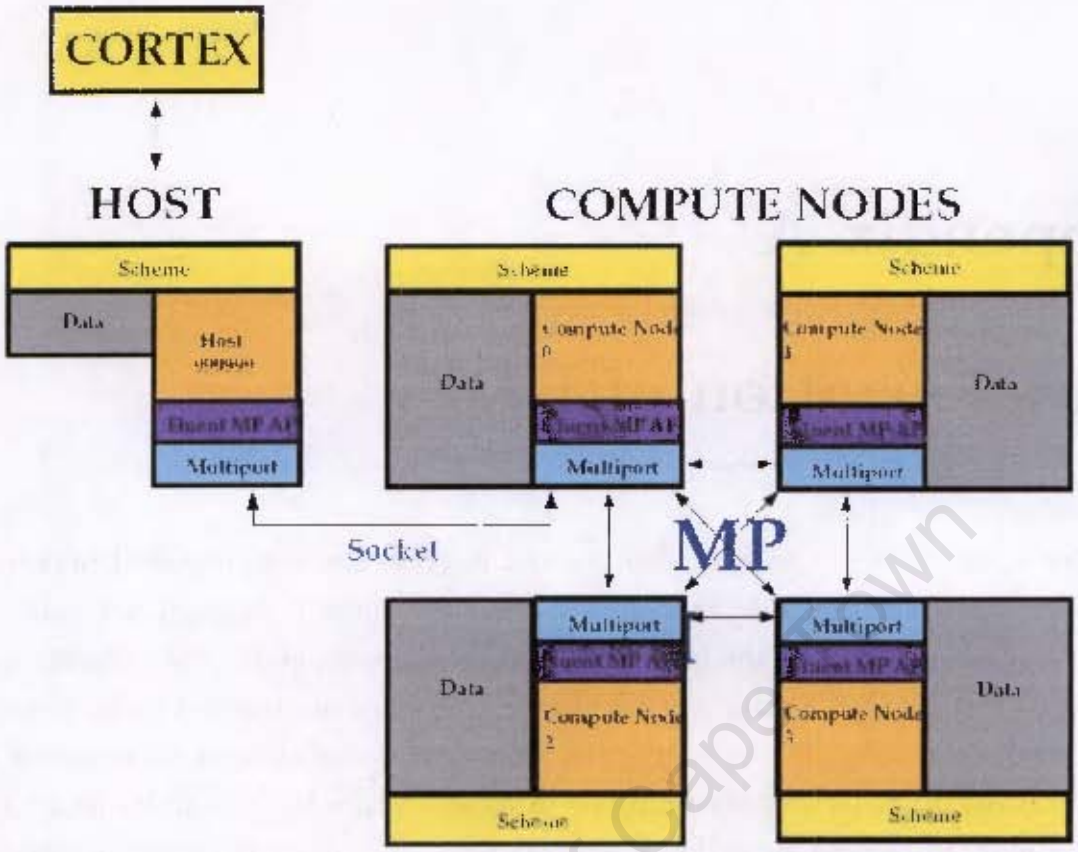

Figure A.1: The parallel architecture FLUENT employs [2]

other nodes. The nodes are all *virtually* linked via the communicator used. This is shown schematically in Figure (A.1). The communicator used is dependent on the computer architecture, as well as the the network in use. This means that if a message is to be printed, or a file written out, the data must all first be sent to node 0, and then on to the host, as shown in Figure (A.2). This will be important for all input/output (IO) operations.

A.2 Partitioning and partitions

As previously mentioned, the computational domain must be partitioned and distributed amongst the nodes. The quality of this partition will determine how much advantage you obtain by running in parallel. If the partition is done in such a manner that there are a large number of cells making up the partition interface , then a large amount of data must be transfered between nodes. This makes the network speed a crucial element. The region of over-lap will also be larger, which decreases the amount of useful

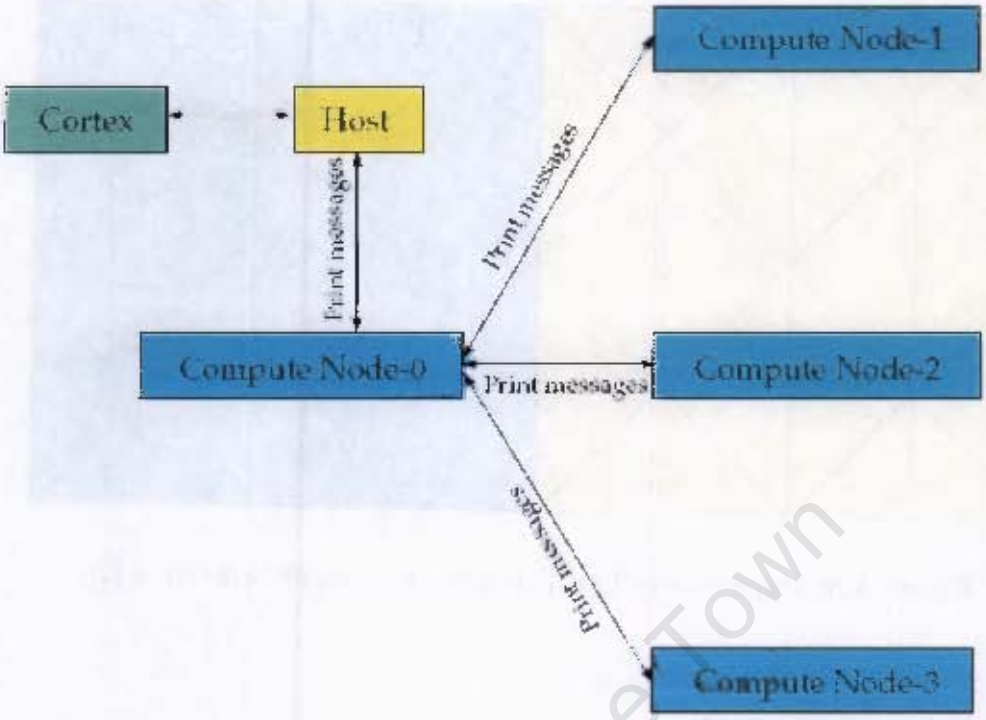

Figure A.2: The message passing technique FLUENT employs [2]

memory on the given node. This is because it must store the information for these over-lapped (exterior) cells as well as the information of the local (interior) cells. For this reason the number of cells making up the partition interface should be reduced as much as possible. Figure (A.3) and (A.4) shows a simple partitioned mesh, with a region of over-lap [2]. Figure (A.5) shows the difference between interior and exterior cells.

FLUENT® offers numerous partitioning methods, which can be performed on the domain itself or on a register. A register is a grouping of cells that have been marked for grid refinement. Using registers gives more control over where the partition will be situated. The partitioning methods include: cartesian co-ordinates, cylindrical co-ordinates, polar co-ordinates, principal axes and spherical co-ordinates [14]. All of these methods have a variety of specification methods. The method used is dependent on the geometry of the domain and the number of nodes. The mesh can be partitioned automatically by FLUENT® , or manually using the methods mentioned above.

The processing power of the various nodes must also be taken into account when partitioning, as all the nodes must finish the current iteration before the next one can start.

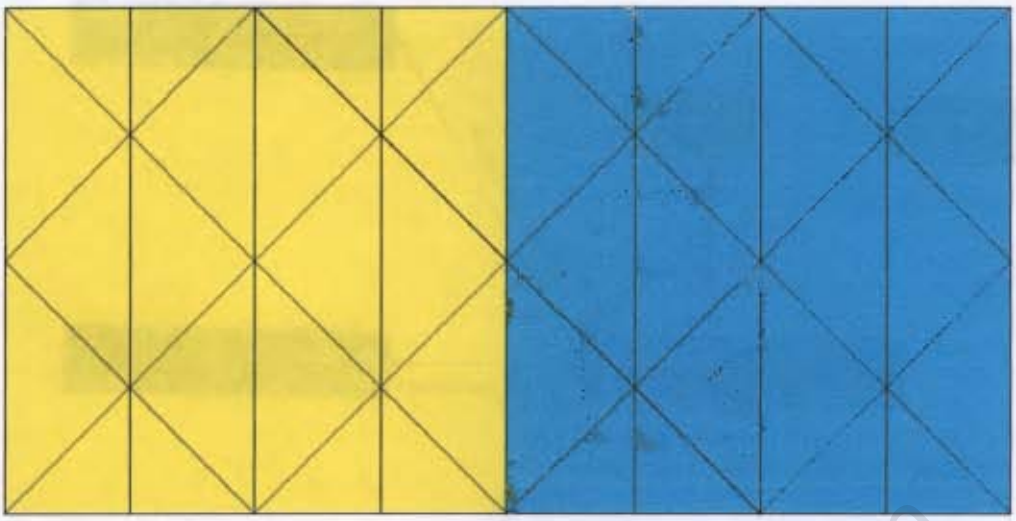

Figure A.3: Unpartitioned grid showing the required division [2]

Thus if the domain is partitioned such that each node has the same number of cells, the cluster will operate at the speed of the slowest machine. To over come this FLUENT® can perform a load balance. Load balancing moves the cells around, such that all nodes finish at approximately the same time. This will decrease the time to solution. This however removes control from the user, and the mesh could end up partitioned in a manner that is undesirable. Performing a load balance too often will increase the time to solution.

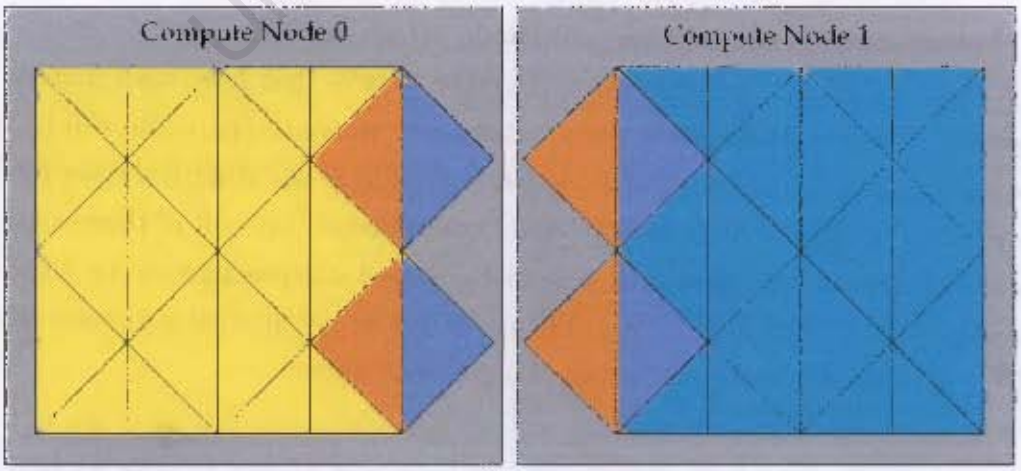

Figure A.4: Partitioned grid showing the over-lapped cells [2]

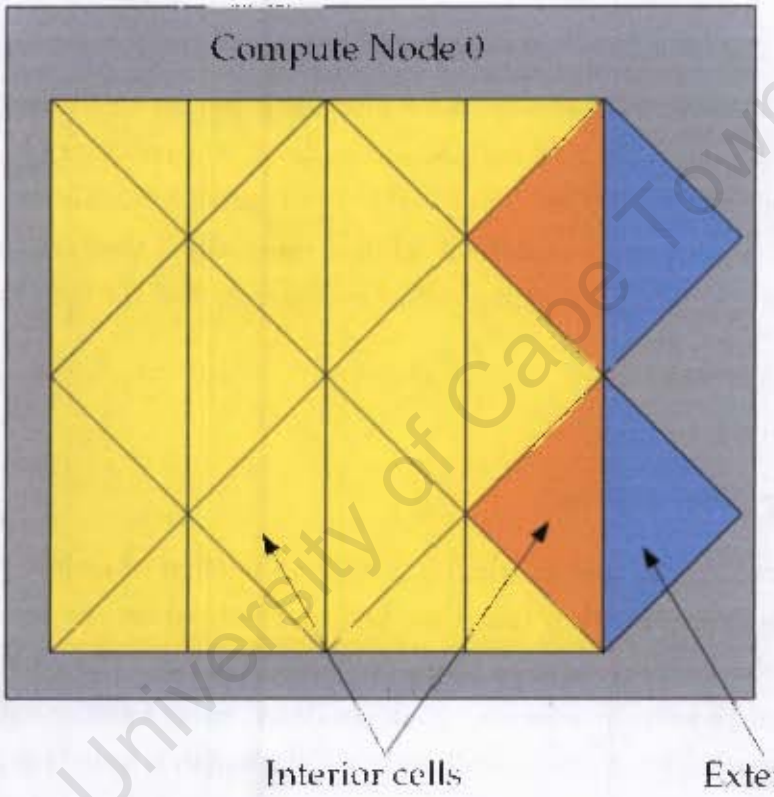

Figure A.5: Grid from one node showing the interior and exterior cells [2]

A.3 Parallelization of the UDF

In order for the UDF to be used by the parallel version of FLUENT®, it must be written such that all commands that pertain to data are only executed on the nodes, and all commands that involve IO are only executed on the host. It is also good practice and programming to write it such that the code will execute in the serial version of FLUENT® [2]. FLUENT® has provided a number of macros to assist in this. The macros used to parallelize the UDF of interest are classified into 4 main categories. They are: Compiler directives, communication macros global reduction macros, and looping macros.

All the data used for calculating the source terms must be available to all the nodes, as well as the host. The UDF links the inlet and the outlet disc to the actuator disc in order to calculate v_R. These links must thus be available to all processes. The momentum source terms must also be available on all the machines, especially if they are to be written to disc. This is done by using the global reduction macros, and the communication macros.

A.3.1 Compiler Directives

Compiler Directives are used to specify where the current portion of code needs to be compiled. They can be compiled such that they will be executed on the serial solver, host or node. Using the negated form of these can also be used. The negated form instructs the portion of code to be execute on all processes except the specified type. This is the more common usage of compiler directives. The negated form is accessed by pre-pending the process type by "!". The following compiler directives are available, as well as the negated form of these [2].

```
#if RP_HOST
   /* Code segment executed on the host only */
#endif /* RP_HOST */

#if RP_NODE
   /* Code segment executed on the host only */
#endif /* RP_NODE */
```

```
#if PARALLEL
   /* Code segment executed on both host and nodes,
    but not serial equivalent to #if RP_HOST || RP_NODE */
#endif /* RP_PARALLEL */
```

A.3.2 Communication Macros

These are used when information is required to be passed from the host to the node, or the node to the host. The data type and the number of variables to be sent are defined by the macro name. The macros are [2]:

```
host_to_node_type_num(val_1,val_2,...,val_num);

node_to_host_type_num(val_1,val_2,...,val_num);
```

Where `type` is the data type, and `num` is the number of variables being sent.

A.3.3 Global Reduction Macros

Global reduction macros are used to synchronize data on all the nodes. This ensures that all the nodes are using the same values in the computations. There are four main types of macros, namely: global summation, global maximum and minimum, and global logicals. The global reduction macros only synchronize the nodes, and all data must be sent to the host, if it's to be used for IO operations, writing to disk for instance. The macros are as follows:

```
PRF_GXSUM1(val)
PRF_GXSUM(val,N,iwork)
PRF_GXHIGH1(val)
PRF_GXHIGH(val,N,iwork)
PRF_GXLOW1(val)
PRF_GXLOW(val,N,iwork)
```

Where `val` is the value to be synchronized, `N` is the number of elements in the array, and `iwork` is a temporary array used by FLUENT®. The `X` must be replaced with either `I` for integers or `R` for real numbers. The version of FLUENT® started will determine if `R` is a single or a double precision real number.

A.3.4 Looping Macros

Looping macros are used to loop over each cell in the given domain, so that the current values can be accessed. As mentioned before there are internal cells, those on the current node, and external cells, the over-lap region. For this reason it is important to distinguish between the cells to be used in the calculation. If the serial looping macro is used, the cells on the current node are used as well as the cells in the over-lap. Thus there is a looping macro for internal cells, external cells and all cells in the continuum specified. The macros are defined as [2]:

```
begin_c_loop_int(c, tc){
   /* Loops over interior cells only */
}
end_c_loop_int(c, tc)

begin_c_loop_ext(c, tc){
   /* Loops over exterior cells only */
}
end_c_loop_ext(c, tc)

begin_c_loop(c, tc){
   /* loops over all cells of the continuum entity */
}
end_c_loop(c, tc)
```


The variables in the brackets (`c` and `tc`) are used to specify which cell, (`c`), is currently being used, and which cell thread, `tc`, the cell belongs to. FLUENT® will loop over all the cells in a given cell thread, changing the cell index as it does so. The cell thread defines the continuum entity of interest and is assigned either by the user, or by FLUENT®, depending on when and where it is used.

The global reduction macros initially are used to synchronize all the values. All the nodes now contain identical variables/arrays. The communication macros are then used to relay this information to the host. Once this step has been completed, all the computers used in the cluster have identical values in their respective variables/arrays.

Appendix B

Numerical results in tabular form

This appendix contains all the numerical data used to create the graphs in the various chapters. It is included to facilitate further research. The data has been ordered according to the chapter that it appeared in.

B.1 Data used for the fan model validation in Chapter 3

Fan 1				Fan 2			
P_i Pa	P_o Pa	T Nm	u m/s	P_i Pa	P_o Pa	T Nm	u m/s
-311.58661	0	71.930562	6.425732132	-311.57321	0	71.921996	6.425732132
-292.8429	0	74.080159	7.496687487	-292.84052	0	74.072144	7.496687487
-278.69986	0	74.261575	8.032	-278.69748	0	74.253651	8.032
-260.99344	0	73.656481	8.567642843	-260.99429	0	73.64859	8.567642843
-214.33424	0	69.316273	9.638598198	-214.342	0	69.309308	9.638598198
-189.98343	0	66.200899	10.17407588	-189.98413	0	66.194624	10.17407588

Table B.1: Fan performance characteristics using the $k - \epsilon$ turbulence model

Fan 1				Fan 2			
P_i	P_o	T	u	P_i	P_o	T	u
Pa	Pa	Nm	m/s	Pa	Pa	Nm	m/s
-272.27676	0	69.190592	6.425732132	-271.74411	0	-69.131011	6.425732132
-283.02835	0	72.993434	7.496687487	-283.22421	0	73.02886	7.496687487
-275.29916	0	73.896604	8.032	-275.28381	0	73.884982	8.032
-263.46463	0	73.832391	8.567642843	-263.49908	0	73.825134	8.567642843
-223.93095	0	70.617581	9.638598198	-223.92885	0	70.611713	9.638598198
-194.20801	0	66.816185	10.17407588	-194.21593	0	66.810818	10.17407588

Table B.2: Fan performance characteristics using the Realizable $k-\epsilon$ turbulence model

Fan 1				Fan 2			
P_i	P_o	T	u	P_i	P_o	T	u
Pa	Pa	Nm	m/s	Pa	Pa	Nm	m/s
-300.25055	0	67.853492	6.425732132	-300.26193	0	-67.846007	6.425732132
-280.31155	0	70.753217	7.496687487	-280.28174	0	70.744376	7.496687487
-262.72586	0	71.231252	8.032	-262.67432	0	71.218939	8.032
-240.16983	0	70.390871	8.567642843	-240.17365	0	70.383305	8.567642843
-191.74454	0	67.007934	9.638598198	-191.64893	0	66.994658	9.638598198
-177.22659	0	66.897503	10.17407588	-176.9171	0	66.867055	10.17407588

Table B.3: Fan performance characteristics using the $k-\omega$ turbulence model

Fan 1				Fan 2			
P_i	P_o	T	u	P_i	P_o	T	u
Pa	Pa	Nm	m/s	Pa	Pa	Nm	m/s
-298.90179	0	68.018246	6.425732132	-298.91797	0	68.01211	6.425732132
-279.36353	0	68.633941	7.496687487	-279.29538	0	68.593184	7.496687487
-262.54245	0	71.180082	8.032	-262.46927	0	-71.166734	8.032
-243.43185	0	70.923122	8.567642843	-243.47487	0	70.916445	8.567642843
-214.46498	0	71.909713	9.638598198	-213.93645	0	71.865693	9.638598198
-184.6971	0	68.633941	10.17407588	-184.4404	0	68.593184	10.17407588

Table B.4: Fan performance characteristics using the $k-\omega$ turbulence model with shear flow

Fan 1				Fan 2			
P_i	P_o	T	u	P_i	P_o	T	u
Pa	Pa	Nm	m/s	Pa	Pa	Nm	m/s
-300.2515	0	67.846931	6.425732132	-300.2677	0	67.839083	6.425732132
-280.32623	0	70.754096	7.496687487	-280.32352	0	70.746165	7.496687487
-262.73788	0	71.235598	8.032	-262.71982	0	71.231424	8.032
-243.05692	0	71.033481	8.567642843	-243.11382	0	71.036468	8.567642843
-214.25478	0	71.912161	9.638598198	-213.99438	0	71.890016	9.638598198
-183.68083	0	68.495277	10.17407588	-183.61298	0	68.479682	10.17407588

Table B.5: Fan performance characteristics using the $k-\omega$ turbulence model with transitional flow

Fan 1				Fan 2			
P_i	P_o	T	u	P_i	P_o	T	u
Pa	Pa	Nm	m/s	Pa	Pa	Nm	m/s
-298.86679	0	68.003808	6.425732132	-298.88757	0	67.993896	6.425732132
-279.36221	0	70.716812	7.496687487	-279.34485	0	70.706626	7.496687487
-262.48901	0	71.178743	8.032	-262.47058	0	71.170086	8.032
-243.34317	0	70.92545	8.567642843	-243.34648	0	70.916524	8.567642843
-214.19856	0	71.893761	9.638598198	-213.8761	0	71.863862	9.638598198
-184.567	0	68.618375	10.17407588	-184.30264	0	68.584255	10.17407588

Table B.6: Fan performance characteristics using the $k-\omega$ turbulence model with shear flow and transitional flow

Fan 1				Fan 2			
P_i	P_o	T	u	P_i	P_o	T	u
Pa	Pa	Nm	m/s	Pa	Pa	Nm	m/s
dnc	0	dnc	6.425732132	dnc	0	dnc	6.425732132
dnc	0	dnc	7.496687487	dnc	0	dnc	7.496687487
dnc	0	dnc	8.032	dnc	0	dnc	8.032
-254.73137	0	73.735019	8.567642843	-254.78508	0	73.727053	8.567642843
-210.48332	0	69.32963	9.638598198	-210.49605	0	69.319439	9.638598198
-185.15607	0	65.723769	10.17407588	-185.29419	0	65.733276	10.17407588

Table B.7: Fan performance characteristics using the SST $k-\omega$ turbulence model

Fan 1				Fan 2			
P_i Pa	P_o Pa	T Nm	u m/s	P_i Pa	P_o Pa	T Nm	u m/s
dnc	0	dnc	6.425732132	dnc	0	dnc	6.425732132
dnc	0	dnc	7.496687487	dnc	0	dnc	7.496687487
dnc	0	dnc	8.032	dnc	0	dnc	8.032
-254.91841	0	73.739763	8.567642843	-254.85057	0	73.729219	8.567642843
-210.63374	0	69.313067	9.638598198	-210.5499	0	69.301663	9.638598198
-183.75226	0	65.564569	10.17407588	-183.78937	0	65.564281	10.17407588

Table B.8: Fan performance characteristics using the SST $k-\omega$ turbulence model with transitional flow

Fan 1				Fan 2			
P_i Pa	P_o Pa	T Nm	u m/s	P_i Pa	P_o Pa	T Nm	u m/s
dnc	0	dnc	6.425732132	dnc	0	dnc	6.425732132
-290.5874	0	74.472052	7.496687487	-290.57516	0	74.464584	7.496687487
-279.08221	0	74.853216	8.032	-279.0936	0	74.846704	8.032
-264.37357	0	74.360576	8.567642843	-264.39545	0	74.352918	8.567642843
-219.59036	0	70.149198	9.638598198	-219.59221	0	70.141907	9.638598198
-192.89857	0	66.494075	10.17407588	-192.89024	0	66.487135	10.17407588

Table B.9: Fan performance characteristics using the standard RSM turbulence model

Fan 1				Fan 2			
P_i Pa	P_o Pa	T Nm	u m/s	P_i Pa	P_o Pa	T Nm	u m/s
dnc	0	dnc	6.425732132	dnc	0	dnc	6.425732132
dnc	0	dnc	7.496687487	dnc	0	dnc	7.496687487
dnc	0	dnc	8.032	dnc	0	dnc	8.032
-255.00233	0	73.669378	8.567642843	-255.01118	0	73.661753	8.567642843
-212.85217	0	69.33936	9.638598198	-212.85461	0	69.332053	9.638598198
-186.08469	0	65.686523	10.17407588	-186.08394	0	64.67957	10.17407588

Table B.10: Fan performance characteristics using the RSM turbulence model with no settings

Fan 1				Fan 2			
P_i Pa	P_o Pa	T Nm	u m/s	P_i Pa	P_o Pa	T Nm	u m/s
dnc	0	dnc	6.425732132	dnc	0	dnc	6.425732132
dnc	0	dnc	7.496687487	dnc	0	dnc	7.496687487
dnc	0	dnc	8.032	dnc	0	dnc	8.032
-252.24564	0	73.270539	8.567642843	-252.29073	0	73.265705	8.567642843
-210.50941	0	69.029482	9.638598198	-210.51361	0	69.021434	9.638598198
-184.95999	0	65.498825	10.17407588	-185.14877	0	65.521331	10.17407588

Table B.11: Fan performance characteristics using the vorticity based Spalart-Allmaras turbulence model

Fan 1				Fan 2			
P_i Pa	P_o Pa	T Nm	u m/s	P_i Pa	P_o Pa	T Nm	u m/s
dnc	0	dnc	6.425732132	dnc	0	dnc	6.425732132
dnc	0	dnc	7.496687487	dnc	0	dnc	7.496687487
dnc	0	dnc	8.032	dnc	0	dnc	8.032
-248.29324	0	73.13304	8.567642843	-248.30806	0	73.125921	8.567642843
-209.40451	0	68.973664	9.638598198	-209.40346	0	68.965152	9.638598198
-184.07143	0	65.382422	10.17407588	-184.06976	0	65.374487	10.17407588

Table B.12: Fan performance characteristics using the strain based Spalart-Allmaras turbulence model

Fan 1				Fan 2			
P_i Pa	P_o Pa	T Nm	u m/s	P_i Pa	P_o Pa	T Nm	u m/s
-258.35767	0	67.872492	6.425732132	-258.51822	0	67.889251	6.425732132
-284.94592	0	73.132145	7.496687487	-284.70087	0	73.116153	7.496687487
-276.14114	0	73.978906	8.032	-276.16135	0	73.971329	8.032
-263.81046	0	73.896599	8.567642843	-263.79785	0	73.891426	8.567642843
-222.72876	0	70.510911	9.638598198	-222.76917	0	70.508071	9.638598198
-193.78868	0	66.679934	10.17407588	-193.82777	0	66.676193	10.17407588

Table B.13: Fan performance characteristics using the Realizable $k-\epsilon$ turbulence model on a tetrahedral mesh

Fan 1			
P_i	P_o	T	u
Pa	Pa	Nm	m/s
-260.12152	0	68.596292	6.425732132
-287.59503	0	73.991268	7.496687487
-275.17526	0	74.319298	8.032
-260.4715	0	73.953609	8.567642843
-218.44571	0	70.312911	9.638598198
-190.11754	0	66.496985	10.17407588

Fan 2			
P_i	P_o	T	u
Pa	Pa	Nm	m/s
-259.73557	0	66.982071	6.425732132
-287.4342	0	73.989741	7.496687487
-275.08481	0	74.309957	8.032
-260.47742	0	73.95526	8.567642843
-218.4212	0	70.310925	9.638598198
-190.08696	0	66.493205	10.17407588

Table B.14: Fan performance characteristics using the standard $k-\epsilon$ turbulence model on a tetrahedral mesh

Fan 1			
P_i	P_o	T	u
Pa	Pa	Nm	m/s
-295.22922	0	19516.43947	6.389617
-287.61218	0	20241.09293	7.496687487
-274.4465	0	20220.17023	8.032
-251.57416	0	19811.28315	8.567642843
-208.25224	0	18556.52715	9.638598198
-183.96434	0	17652.8456	10.17407588

Fan 2			
P_i	P_o	T	u
Pa	Pa	Nm	m/s
-292.53607	0	19398.28417	6.389617
-287.53723	0	20237.29434	7.496687487
-274.44211	0	20217.39708	8.032
-251.53873	0	19809.53462	8.567642843
-208.25635	0	18555.20368	9.638598198
-183.95901	0	17651.51019	10.17407588

Table B.15: Fan performance characteristics using the standard $k-\epsilon$ turbulence model with $d_{FC} = 10m$

Fan 1			
P_i	P_o	T	u
Pa	Pa	Nm	m/s
-274.7305	0	19092.78717	6.425732132
-273.77493	0	19825.17478	7.496687487
-272.50656	0	20089.71882	8.032
-261.24741	0	20052.5187	8.567642843
-215.37608	0	18844.67284	9.638598198
-190.13814	0	17961.54452	10.17407588

Fan 2			
P_i	P_o	T	u
Pa	Pa	Nm	m/s
-274.68564	0	19090.21681	6.425732132
-273.7789	0	19821.9093	7.496687487
-272.51981	0	20089.20797	8.032
-261.24741	0	20054.05413	8.567642843
-215.37608	0	18839.90801	9.638598198
-190.12265	0	17959.64594	10.17407588

Table B.16: Fan performance characteristics using the Realizable $k-\epsilon$ turbulence model with $d_{FC} = 9m$, and $\gamma_{root} = 61$

Fan 1				Fan 2			
P_i Pa	P_o Pa	T Nm	u m/s	P_i Pa	P_o Pa	T Nm	u m/s
-252.50241	0	11299.5431	5.344462287	-252.34145	0	11295.47707	5.344462287
-247.47743	0	11422.50736	5.894627522	-247.36549	0	11420.16389	5.894627522
-245.11128	0	11607.62824	6.444792757	-245.12172	0	11606.66277	6.444792757
-290.84656	0	12721.07014	6.916362959	-290.86838	0	12720.56043	6.916362959
-250.95096	0	12238.72855	7.545123228	-250.88795	0	12237.41857	7.545123228
-239.06245	0	12127.22718	8.01669343	-239.08258	0	12126.72384	8.01669343
-217.73425	0	11776.61784	8.566858665	-217.74396	0	11776.33447	8.566858665
-191.05132	0	11161.92066	9.117023901	-191.08676	0	11161.47625	9.117023901
-159.76578	0	10318.37703	9.667189136	-159.75104	0	10316.86241	9.667189136

Table B.17: Fan performance characteristics using the standard $k-\epsilon$ turbulence model with $d_{FC} = 9m$, and $\gamma_{root} = 61$, on an axi-symmetric model

B.2 Data used to investigate the effect of ground clearance in Chapter 8

u_1 m/s	u_2 m/s	u_3 m/s	u_4 m/s	u_5 m/s	u_6 m/s
-0.90643191	0.99995148	1.0207608	4.6129766	7.6393585	7.4602847
-1.8678855	4.8490629	8.4628038	9.6040058	10.194004	10.308368
3.6720386	9.6398182	10.147365	10.452929	10.656077	10.646706
8.4211826	10.128481	10.506426	10.672878	10.723672	10.712842
9.087739	10.330987	10.636519	10.736227	10.753835	10.742961
9.4124804	10.393025	10.646658	10.723128	10.746935	10.750531

Table B.18: Velocity through each fan for a bank of 12 ACHE's in windless conditions

u_1 m/s	u_2 m/s	u_3 m/s	u_4 m/s
-0.75458115	4.3733315	7.8996186	9.4512215
4.2208824	9.6710234	10.249154	10.482006
8.9939833	10.321545	10.634315	10.70667
9.5859509	10.508701	10.704921	10.715249
9.8719559	10.586969	10.704655	10.719891
10.017978	10.634232	10.722126	10.709183

Table B.19: Velocity through each fan for a bank of 8 ACHE's in windless conditions

u_1 m/s	u_2 m/s	u_3 m/s
1.5021477	8.3341494	9.8414459
8.7699356	10.239537	10.538308
9.7079144	10.535342	10.637909
10.010472	10.632551	10.660488
10.151279	10.656529	10.676996
10.230285	10.680631	10.695225

Table B.20: Velocity through each fan for a bank of 6 ACHE's in windless conditions

u_1 m/s	u_2 m/s
7.6923437	10.008668
9.7928982	10.534454
10.182462	10.626315
10.312895	10.650053
10.376686	10.653722
10.423014	10.694677

Table B.21: Velocity through each fan for a bank of 4 ACHE's in windless conditions

u_1 m/s
10.0117
10.404507
10.482743
10.488377
10.48357
10.482914

Table B.22: Velocity through each fan for a bank of 2 ACHE's in windless conditions

u_1 m/s
10.417139
10.498499
10.50089
10.495726
10.482247
10.480075

Table B.23: Velocity through each fan for a bank of 1 ACHE's in windless conditions

B.3 Data used to investigate the effect of a walkway in Chapter 9

u_1 m/s	u_2 m/s
7.9780264	10.018343
9.9751749	10.543029
10.351393	10.633419
10.438	10.65473
10.478534	10.659603
10.498487	10.640389

Table B.24: Velocity through each fan for a bank of 4 ACHE's with $\frac{W_w}{d_{FC}} = 0.159$

u_1 m/s	u_2 m/s
7.9289088	9.9640036
10.019707	10.533428
10.394366	10.394366
10.470377	10.65688
10.50656	10.66161
10.525573	10.641893

Table B.25: Velocity through each fan for a bank of 4 ACHE's with $\frac{W_w}{d_{FC}} = 0.317$

u_1 m/s	u_2 m/s
7.8689003	9.965663
9.9948769	10.479309
10.382792	10.598692
10.451571	10.615538
10.490593	10.612556
10.511755	10.591344

Table B.26: Velocity through each fan for a bank of 4 ACHE's with $\frac{W_w}{d_{FC}} = 0.476$

u_1 m/s	u_2 m/s
7.7943373	9.8872519
9.9900389	10.476301
10.393208	10.601036
10.451571	10.615538
10.5029	10.614068
10.525103	10.595356

Table B.27: Velocity through each fan for a bank of 4 ACHE's with $\frac{W_w}{d_{FC}} = 0.635$

u_1 m/s	u_2 m/s	u_3 m/s	u_4 m/s
0.19772227	3.804399	7.612782	9.3132305
4.6810055	9.5825272	10.227076	10.479479
9.3265152	10.329078	11.136477	10.699362
9.8896914	10.535305	10.700349	10.71381
10.134056	10.609485	10.709733	10.727787
10.234396	10.642547	10.721607	10.707643

Table B.28: Velocity through each fan for a bank of 8 ACHE's with $\frac{W_w}{d_{FC}} = 0.159$

u_1 m/s	u_2 m/s	u_3 m/s	u_4 m/s
0.50153017	3.6265664	7.491313	9.2250557
2.040503	6.2093549	9.992713	10.453324
9.476922	10.353525	10.625232	10.699762
9.9751043	10.54046	10.69416	10.716526
10.198654	10.609901	10.703679	10.719918
10.305326	10.643287	10.720431	10.707955

Table B.29: Velocity through each fan for a bank of 8 ACHE's with $\frac{W_w}{d_{FC}} = 0.317$

u_1 m/s	u_2 m/s	u_3 m/s	u_4 m/s
0.82666367	3.6788704	7.4320793	9.2695179
5.9777236	9.4389381	10.148592	10.446862
9.4735832	10.301484	10.61155	10.715374
9.9830742	10.505679	10.699776	10.734526
10.193652	10.553174	10.696342	10.728271
10.305666	10.597436	10.71664	10.712785

Table B.30: Velocity through each fan for a bank of 8 ACHE's with $\frac{W_w}{d_{FC}} = 0.476$

u_1 m/s	u_2 m/s	u_3 m/s	u_4 m/s
1.1404672	3.5940564	7.3293982	9.1563406
6.3114915	9.4050617	10.13716	10.453803
9.5002222	10.293681	10.60772	10.708849
10.007567	10.490176	10.690712	10.7214
10.228197	10.556943	10.696227	10.731841
10.32861	10.601163	10.716394	10.713444

Table B.31: Velocity through each fan for a bank of 8 ACHE's with $\frac{W_w}{d_{FC}} = 0.635$

u_1 m/s	u_2 m/s	u_3 m/s	u_4 m/s	u_5 m/s	u_6 m/s
-0.032055106	1.2671862	1.977419	2.2468677	7.0505939	8.3421602
-1.5670556	3.8440354	7.9152069	9.3925209	10.141347	10.315018
4.3241119	9.6028757	10.149582	10.454695	10.655155	10.642817
8.7921896	10.161977	10.516762	10.671605	10.738015	10.723114
9.5016804	10.372758	10.641182	10.731316	10.741816	10.75536
9.7764921	10.475803	10.689703	10.726478	10.729488	10.751082

Table B.32: Velocity through each fan for a bank of 12 ACHE's with $\frac{W_w}{d_{FC}} = 0.159$

u_1 m/s	u_2 m/s	u_3 m/s	u_4 m/s	u_5 m/s	u_6 m/s
0.20671442	0.91892701	0.83922869	4.0408244	7.2144647	7.6914229
-1.1883199	3.8526168	7.7486148	9.278554	10.104351	10.321589
5.0318036	9.6005869	10.157574	10.452003	10.648413	10.634998
8.9827633	10.180343	10.517443	10.66931	10.739249	10.700478
9.6250467	10.389417	10.640702	10.729565	10.740471	10.75522
9.882432	10.487912	10.686646	10.724224	10.728268	10.744769

Table B.33: Velocity through each fan for a bank of 12 ACHE's with $\frac{W_w}{d_{FC}} = 0.317$

u_1 m/s	u_2 m/s	u_3 m/s	u_4 m/s	u_5 m/s	u_6 m/s
0.80410081	1.1935273	0.82552969	3.7356915	7.104033	7.5754457
-0.99038732	4.3307796	7.7503939	9.1533241	10.00448	10.278551
5.7518444	9.5064344	10.111266	10.449211	10.654591	10.635624
9.0172224	10.132253	10.503756	10.666897	10.744211	10.702937
9.6399384	10.299098	10.609833	10.68749	10.69306	10.777303
9.8969049	10.430584	10.67695	10.721454	10.725316	10.763237

Table B.34: Velocity through each fan for a bank of 12 ACHE's with $\frac{W_w}{d_{FC}} = 0.476$

u_1 m/s	u_2 m/s	u_3 m/s	u_4 m/s	u_5 m/s	u_6 m/s
0.80631989	1.1915425	0.80757266	3.7670047	7.1056809	7.562253
-0.75779426	4.4611144	7.7197223	9.1059961	9.9655752	10.280242
6.2048974	9.4998426	10.11007	10.447973	10.655817	10.63594
9.0815468	10.1275	10.501308	10.667457	10.750241	10.701832
9.6833544	10.335772	10.622487	10.708827	10.709199	10.772335
9.9369249	10.43641	10.674523	10.719063	10.724296	10.759293

Table B.35: Velocity through each fan for a bank of 12 ACHE's with $\frac{W_w}{d_{FC}} = 0.635$

B.4 Data used to investigate a 2 dimensional array of ACHE's in Chapter 10

u_1 m/s
10.31976
10.420135
10.429447
10.428615
10.421398
10.404992

Table B.36: Velocity through each fan for a 2x2 bank of ACHE's

u_1 m/s	u_2 m/s
7.0062647	10.410672
9.6348782	10.595693
10.126445	10.633069
10.292549	10.660699
10.318733	10.646662
10.346364	10.648864

Table B.37: Velocity through each fan for a 2x1 bank of ACHE's with a joined plenum

u_1 m/s	u_2 m/s	u_3 m/s	u_4 m/s
10.504077	9.5691662	9.7771091	10.066773
10.657954	10.348475	10.35605	10.436627
10.633843	10.527745	10.483038	10.529599
10.628391	10.579434	10.523169	10.566138
10.540033	10.560176	10.46544	10.505832
10.550079	10.603004	10.541007	10.584682

Table B.38: Velocity through each fan for a 4x4 bank of ACHE's

B.5 Data used investigate the influence if wind in Chapter 11

u_1 m/s	u_2 m/s	u_3 m/s	u_4 m/s	u_5 m/s	u_6 m/s	u_7 m/s	u_8 m/s	u_9 m/s
7.5354199	10.060883	10.569201	8.5471687	10.244256	9.8790388	9.8114576	8.9787083	8.4526644
9.8297205	10.615519	10.664414	10.00424	10.591692	10.542967	10.286776	10.185686	10.000115
10.288216	10.716286	10.673319	10.33706	10.677505	10.67055	10.448384	10.398685	10.304834
10.428986	10.712582	10.688976	10.457677	10.701238	10.684868	10.506885	10.466915	10.392347
10.490424	10.751015	10.67332	10.513024	10.727622	10.690447	10.536981	10.497864	10.437482
10.5067	10.734422	10.588605	10.524426	10.703837	10.642786	10.546165	10.508116	10.448583

Table B.39: Velocity through each fan for a 9x9 bank of ACHE's

u_1 m/s	u_2 m/s	u_3 m/s	u_4 m/s	u_5 m/s	u_6 m/s
-1.1796658	0.78739965	0.5085839	5.0069222	8.260416	9.478487
-2.8002324	8.0488882	9.7709484	10.126179	10.420153	10.483405
3.3475759	10.721332	10.668522	10.648046	10.682588	10.637366
7.8333192	10.647717	10.702564	10.718746	10.7319	10.655775
8.959774	10.676391	10.740289	10.744778	10.722243	10.701548
9.3636332	10.720118	10.76809	10.773377	10.756883	10.68403

Table B.40: Velocity through each fan for a bank of 12 ACHE's with a joined plenum

u_1 m/s	u_2 m/s	u_3 m/s	u_4 m/s	u_5 m/s	u_6 m/s
-1.4907111	1.7105153	1.5573599	2.5914855	6.7659717	9.8169231
-2.4148128	4.5706768	9.4203711	10.026488	10.162228	10.288217
3.0383742	10.936025	10.736989	10.464685	10.047843	9.9500198
6.7353787	10.811238	10.618958	10.553617	10.480335	10.566387
6.355329	10.991518	10.769093	10.705271	10.621441	10.379354
3.4587471	11.017237	10.562574	10.365785	10.499905	10.597585

Table B.41: Velocity through fan 1 to 6 for a bank of 12 ACHE's with a $3m/s$ wind

u_7 m/s	u_8 m/s	u_9 m/s	u_{10} m/s	u_{11} m/s	u_{12} m/s
5.6499562	9.8327579	7.7851658	2.0732584	0.4367893	-1.1080364
10.187848	9.9969463	9.7707529	9.6094637	8.3140955	-3.4915817
10.277966	10.314532	10.260963	10.331758	10.201488	1.1648569
10.648052	10.651276	10.637349	10.681026	10.80383	4.3809757
10.404489	10.506648	10.646085	10.652936	10.610388	8.5693789
10.632629	10.584405	10.591489	10.687878	10.721931	9.6016397

Table B.42: Velocity through fan 7 to 12 for a bank of 12 ACHE's with a $3m/s$ wind